Human Imaging and Identification Algorithms with UWB Doppler Radar Interferometry

by

Kenshi Saho

Acknowledgments

This work in Toru Sato Laboratory, Graduate School of Informatics, Kyoto University would not have been possible if not for the support and guidance of many people, whom I would like to acknowledge here.

First of all, I would like to express my gratitude to my supervisor Professor Toru Sato for his consistent guidance, continuous support, and kind advice. It would have been impossible to complete this thesis without his constructive suggestions and criticism. I have learned a lot by seeing his professionalism, leadership, and passion to various works, and his tolerance always encouraged me during the current work. He is the greatest educator, researcher, and outstanding role model to me. I am very honored to be his student.

I would like to express my sincere appreciation to Assistant Professor Takuya Sakamoto for his appropriate advice and invaluable suggestions. He taught me attractiveness of the Ultra Wide-Band (UWB) radar imaging, and showed me the best example of how to solve various types of research problems logically and mathematically. Moreover, his excellent research papers were the best models and references for this thesis.

I am very thankful to my thesis committee members, Professors Tetsuya Matsuda and Mamoru Yamamoto for their insightful comments and careful reading of this thesis. They spent their time on the discussion with me despite their busy schedule and I got a lot of inspiration for my thesis and research.

My work was greatly supported by all staffs of Toru Sato Laboratory. I deeply appreciate Associate Professor Seiji Norimatsu for his insightful advice and criticism. Many interesting and constructive comments based on his deep knowledge were important support for the present work. I wish to thank Assistant Professor Hirofumi Taki for his fruitful comments and discussions. His wide knowledge of medicine and various equipments was very important support for the current work. Moreover, his daily works for our laboratory highly helped me and other members. I am grateful to Assistant Professor Shouhei Kidera, now of the University of Electro-Communications for his constructive opinions and comments. When I was in undergraduate course, he taught me basics of UWB radar remote sensing. My knowledge and skills obtained from his detailed guidance were indispensable for the current work. Special thanks go to laboratory secretary Ms. Mari Watanabe for her careful support.

Last but not least, I would like to make the cordial appreciation to my most important people. I would like to express my heartiest gratitude to my parents Michinori and Rikimi for their immense support, patience and understanding. I am very honored to be their son. I sincerely thank my grandparents Masachika and Tomiyo, and Takanori and Kinko, younger brothers Atsuya and Kouki, and younger sister Miori for their continuous moral support. Moreover, I am heartily grateful to my fiancée Mai for her warm encouragement and affectionate support. Without their selfless love, I could never reach the goal of this long journey. I thank them from the bottom of my heart.

<div align="right">

Kenshi Saho
(　　　　)

</div>

in Kyoto
March 2013

Preface

Advanced monitoring systems for robot and security applications in locations such as towns, houses, shops and hospitals, have become increasingly prevalent in our society. A key goal for this type of monitoring is accurate and real-time imaging and the identification of people using a simple sensing system. Although many studies has developed human detection systems using optical sensors, the acquisition of adequate range resolution with this approach is difficult. Moreover, they do not work well in difficult environments such as low light and smoky conditions. Recently, a number of studies on human sensing, using ultrasonics, have been reported. However, the ultrasonic devices for robust and wide-area measurements in air are still under development and research.

To resolve these problems, human imaging systems using radar have been widely studied because of their advantages in range resolution and robust measurements. In particular, micro-Doppler radar and ultra wide-band (UWB) radar are attractive technologies for human motion/shape acquisition. Micro-Doppler radar can recognize the motions of multiple targets, and can realize human tracking using interferometry. The technique was first applied to continuous wave radar, but its resolution is inadequate for identifying human subjects. UWB radar can reconstruct high-resolution shapes of a single and simple-shaped target; however it is difficult to apply it to multiple complex targets such as humans. Taking these properties into account, the combined techniques of UWB radar, micro-Doppler radar and interferometry have great potential for high-resolution human imaging.

In the present study, human imaging and identification algorithms are proposed with this combined technique, termed UWB Doppler radar interferometry. First, a high-resolution imaging algorithm for multiple moving targets is introduced, and its performance is investigated using numerical simulations and experiments assuming a few revolving targets and numerical human model. These investigations verify that UWB Doppler radar interferometry composed of three receiving antennas can realize separation of multiple targets, and accurate imaging of each separated target. However, many false images are generated because of interference from multiple targets such as various parts of the body, and this leads to incorrect extraction of humans. To resolve this problem, the mechanism for this type of false image is clarified, and false image detection and rejection algorithms using velocity information are proposed. Experiments which assume a variety of pedestrian targets in a realistic situation show that the proposed imaging

algorithm achieves high-resolution and reliable human imaging in real-time. Moreover, applications to humans walking in various directions are carried out and the effectiveness of the algorithm is established.

Next, two human identification algorithms are proposed based on human shape/motion information obtained using the proposed imaging algorithm with UWB Doppler radar interferometry. One of the proposed algorithms is a classification algorithm for various pedestrian types. The proposed classification algorithm uses feature parameters extracted from the silhouette and radial velocity distributions of the UWB Doppler radar images. This classification algorithm realizes accurate classification of a variety of motion types such as pedestrians with both arms swinging, pedestrians carrying a bag and swinging one arm, and those on crutches or in wheelchairs. Another algorithm separates images of two closely spaced pedestrian targets. The proposed separation algorithm applies the support vector machine to the estimated human images. The performance evaluations with experiments in a realistic environment verify that these proposed identification algorithms accomplish accurate classification/separation in real-time processing.

Contents

List of Tables

List of Figures

xi

xii

Acronyms

Each acronym is defined the first time it appears. As a further help, all acronyms are listed here in alphabetical order.

ANN	artificial neural network
BST	boundary scattering transform
CCD	charge-coupled device
CW	continuous wave
DOA	direction-of-arrival
EIRP	equivalent isotropically radiated power
FCC	federal communication commission
HOG	histograms of oriented gradients
IBST	inverse boundary scattering transform
IPP	inter-pulse period
IR	infrared
ISAR	inverse synthetic aperture radar
k-NN	k-nearest neighbor
MIMO	multiple-input multiple-output
NBC	naive Bayesian classifier
RMS	root mean square
SAR	synthetic aperture radar
SDFT	sliding-window discrete Fourier transform
SEABED	shape estimation algorithm based on BST and extraction of directly scattered waves
SPWD	smoothed pseudo Wigner distribution
STFT	short-time Fourier transform
SVM	support vector machine
TR	time-reversal
UWB	ultra wide-band

Chapter 1

General Introduction

1.1 Introduction

The use of intelligent robots such as household, nursing, and rescue robots will become widespread in the near future thanks to technological advances in recent years [1–3]. On the other hand, the security situation of the society has deteriorated since the start of the 21st century [4], and the importance of security technology to protect people from crime and terrorism is increasing.

For these reasons, surveillance and monitoring systems in locations such as towns, houses, shops and hospitals are ubiquitous in today's society. Such systems need to be able to sense people and other objects. For instance, the automatic and real-time identification of intruders is a promising application in surveillance systems. Here, the word "identification" means the clarification of what the detected target actually is. For example, is the detected target a human or a dog? If the target is human, is the person an intruder? Can the motion, location, figure, and other individual features of the person be detected? The ability to extract such information from the sensing data is required. Furthermore, moving robots must be able to locate and specify various objects to avoid collisions or to identify targets. For these purposes, a simple monitoring system, which can realize accurate imaging and target identification, is essential in robots.

Although various sensing targets can be considered, this thesis focuses on sensing humans which is the most important problem for intelligent monitoring systems. The properties required to human monitoring systems are summarized as follows:

- **Non-contact sensing**: Monitoring of a wide area should be realized by fixed sensors or sensors embedded in robots.

- **Real-time capability**: If there are intruders or obstacles, the system must identify them immediately.

- **Simple system**: Physical packaging should be as small as possible.

- **Robustness**: Sensors should be able to work in difficult environments (e.g., in the existence of many obstacles, low-light conditions, and smoky environments).

- **Complex target determination**: Sensors should be able to discern multiple complex-shaped targets such as the human shape.

- **High-resolution imaging of shape/motion**: Detailed shape/motion information should be effective for human identification.

A large number of studies on the development of non-contact human sensing systems were based on wave propagation. Although many researchers have developed human detection and identification systems using optical sensors such as cameras and lasers, the acquisition of adequate range resolution is difficult. Moreover, they do not work well in environments such as low light and smoky conditions. Ultrasound imaging has been applied in medical and biological fields, but there is little research on identifying human images in free space.

Radar human sensing systems have been studied widely because of their robustness to the environment compared with alternative wave-based systems. In particular, continuous wave (CW) micro-Doppler radar is a popular technique because motion recognition is easily realized using low-cost and small systems, and the detection of any presence, and human activity classification, are realized using time-frequency micro-Doppler signatures. For example, tracking of multiple humans has been achieved using CW micro-Doppler radar and interferometry with only three antennas, although its spatial resolution was inadequate to acquire details of shape and information about motion. As a solution to this problem, ultra wide-band (UWB) radar is a powerful tool because of its high-resolution capability. Shape estimation using UWB radar for a moving target has been conducted with a small number of antennas. However, because the algorithm used considers only a single and simple convex target, it is difficult to apply this technique to complex targets such as humans is difficult.

To satisfy all the requirements of human monitoring systems, a combination of UWB radar, micro-Doppler radar, and interferometry techniques is an option. Here, we call this combined technique "UWB Doppler radar interferometry". The two objectives of this thesis are to realize high-resolution human imaging using the UWB Doppler radar interferometry, and to propose target separation and classification algorithms based on acquired images for human identification.

In the following subsections, a detailed overview of the above conventional techniques is given, and the background and targets of the work are clarified. Section 1.2 introduces human remote sensing techniques with various wave-propagation-based systems, and clarifies the drawbacks of conventional systems. Section 1.3 introduces the CW micro-Doppler radar technique. Human motion identification and tracking algorithms based on time-frequency micro-Doppler signatures are reviewed. Section 1.4 describes UWB radar techniques including accurate localization and shape estimation techniques, and gives a simple introduction to UWB Doppler radar. The targets and the contents of this thesis are presented in Section 1.5.

1.2 Conventional Human Sensing Techniques with Various Wave-based Systems

This section reviews conventional techniques to detect, track and/or identify people with a variety of sensors using various propagated waves. The features and drawbacks of conventional techniques are clarified by comparing the requirements of the human monitoring systems outlined in the previous section. First, the classification of sensor types and their basic properties are identified. Sensing types can be classified into two categories from the view point of signaling:

- Passive sensing: sensors acquire signals that are available from the environment.

- Active sensing: sensors transmit their own signals and measure the properties of the responses.

Passive sensing systems are easily realized and are relatively low-cost and small in size. However, the quality of sensing is very dependent on the environment of the observation area. In contrast, active sensing systems can realize robust and accurate sensing because they can emit signals which are formatted to take into account the environment and target features. However, in general, their complexity and cost become high.

Sensors can also be classified by wave type. The main difference between wave types is the difference in wavelengths. The wave types which are often used for human sensing and their wavelengths in air are:

- Visible light: 400–800 nm

- Infrared radiation: 0.7 μm–1 mm

- Radio wave: 1 mm–100 m

- Ultrasonic: more than 1.7 cm

The sensing characteristics are almost determined by the wavelength which dictates the resolution and reflection properties of the target. Therefore, consideration of both the properties of each sensor/wave type and the sensing objectives is important in choosing a suitable sensor or combination of sensors.

1.2.1 Camera and Image Processing Approach

The optical camera is a representative passive sensor, which has already been used for surveillance systems and monitoring systems for robots because of its simple implementation. In camera systems, person detection and tracking are realized using image processing. One of the popular detection techniques currently deployed involves background

subtraction [5–8]. This technique allows quick detection of humans. However, applications of this technique are limited to an environment where the background scene is either static or slowly changing. This can lead to difficulties, for example, in office or conference rooms where background objects such as chairs are moved quite frequently, leading to much false detection. Other popular approaches involve object segmentation and pattern matching. Object segmentation is the extraction of the human shape from the image directly without subtracting the background [9–12]. Pattern matching convolves the input image with sample images of the object [13–17]. The matching is often conducted in other feature spaces such as histograms of oriented gradients (HOG) [17], and the matching result is then classified to identify a detected target with various basic mathematical tools such as a support vector machine [15, 16]. However, the accuracy and robustness of these methods are insufficient in difficult environments (e.g. the number of persons and the presence of many other moving targets such as pets and robots). For accurate identification of detected person, human face recognition approach based on the pattern matching techniques is widely studied [18–21]. Déniz et al. [20] proposed a robust face recognition method using HOG to compensate for errors due to occlusions and illumination changes, and achieved accurate recognition of a variety of human face. However, these techniques need clear image of person's face to realize identification with sufficient accuracy, and a robust extraction of such image is difficult. The primary problem here is that these approaches use only two-dimensional images.

For accurate detection and identification of humans, three-dimensional information is apparently effective, and this thesis focuses on three-dimensional sensing of shape and motion in the followings. In camera sensing systems, common techniques for this purpose are to use distance information obtained with a stereo camera [22–25], and motion information obtained by object tracking using video images [9, 10, 14, 15, 24, 26–28]. The stereo camera technique realizes an estimation of the distance to the target using two cameras, and low-complexity systems composed of CCD (Charge-Coupled Device) cameras have been developed and implemented as the eyes of robots [25]. Fig. 1.1 shows an outline of a stereo camera system. This system first establishes a common matching point between two cameras, and then estimates the position of the matching point using triangulation principles. However, this method is limited by triangulation geometry. It is difficult to select a suitable long baseline because of the trade-off between resolution and reduced ambiguity in the matching process. On the other hand, use of motion information obtained by video images is effective in improving the accuracy of human detection and increasing the number of effective parameters for human identification. The basic approaches are frame-differencing [10, 26, 27] and optical flow [14, 15, 28] methods. The advantages of motion-based imaging using these methods, compared with the background subtraction and pattern matching approaches, is that the number of misdetections can be reduced using low-complexity processing, and the disadvantage is that images of people disappear when they stop moving, requiring further processing. To improve the resolution and accuracy, the use of multiple cameras (more than two) has been proposed [29–31]. Nobuhara et
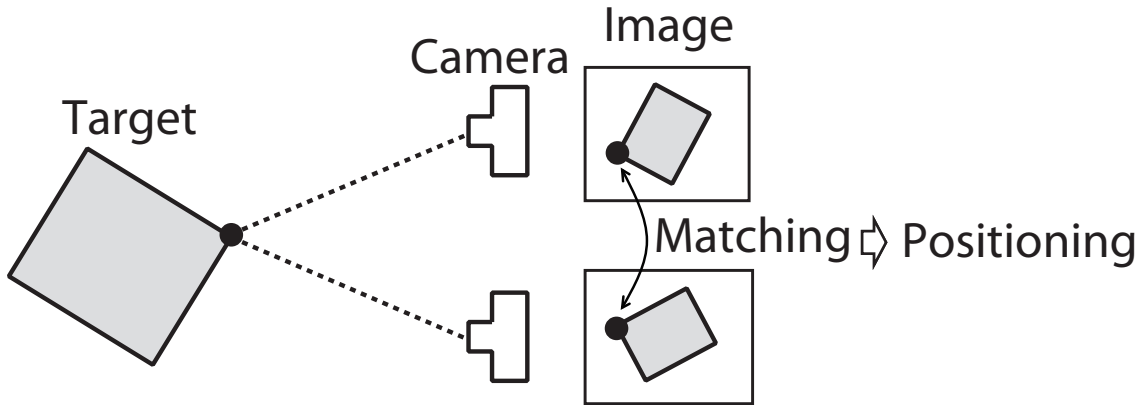
Figure 1.1: Outline of the stereo camera system.

al. [29] achieved an accurate human shape estimation using 13 cameras placed at various locations. Obviously, the system size and cost become high.

Based on these reviews, although a large number of camera sensing techniques have been studied and have realized person detection and identification for various conditions, they cannot realize an appropriate resolution to obtain detailed information of shape and motion with a picture or movie obtained from a single camera. In addition, real-time processing to acquire appropriate resolution is difficult for conventional camera systems because the processing becomes complex with an increasing number of cameras. Moreover, sensing accuracy is very dependent on the luminance of the surface of a target, and the light conditions.

1.2.2 Laser Rangefinder with Visible Light

One of the active sensor types is a visible ray laser which emits some form of radiation and estimates the target range by detecting reflections from the target. This type of system is known as a laser rangefinder [32]. Laser systems are more robust than camera systems, because the laser itself emits the signals, and its rangefinder can determine the target locations without the pattern matching that is required for a stereo camera. In addition, compared with radio, ultrasound and infrared sensors, the visible ray laser is immune to multipath and clutter because of its short wavelength. Two dimensional laser rangefinders have been used to detect and localize humans [33–37], and shape estimation using a three dimensional laser rangefinder has been achieved [38–40]. These methods acquire the range information using triangulation or time-of-flight methods.

An example of an image of a human face estimated by means of a three dimensional laser rangefinder and the triangulation technique is shown in Fig. 1.2, which shows the picture of a three-dimensional laser scanner (Konica Minolta Optics, Inc., VIVID910) and its

sensing system configuration [40]. This system employs laser beam light-sectioning technology which scans work pieces using a slit beam, and light reflected from the work piece is acquired by a CCD camera. Three dimensional data are then created by triangulation to determine distance information. The laser beam is then scanned using a high-precision galvanometric mirror. Fig. 1.3 shows the target face and imaging result estimated by this laser scanner. As shown in this result, the accurate acquisition of range information and sensing of a human face are realized. However, the regions where an image is not obtained are apparent, especially near the hair, because the reflection power of a laser beam is quite dependent on surface luminance. Moreover, the laser beam is required to scan in all directions to obtain a comprehensive target image, and this leads to long data acquisition times and relatively large system sizes. To obtain the image shown in Fig. 1.3, the total time for data acquisition and imaging was approximately 30 s, which was too long for the considered applications. In addition, the laser output power must be limited to protect the eye.

1.2.3 Infrared Techniques

Infrared (IR) sensors are good candidates for advanced human monitoring systems because several characteristics are different from visible light. For example, the thermography technique using passive IR sensors can acquire the temperature of objects [41–43]. Thermography detects radiation in the infrared range of the electromagnetic spectrum and produces images of that radiation. Because infrared radiation is emitted by all objects based on temperature, according to the black body radiation law, thermography makes it possible to find targets without visible illumination. The amount of radiation increases with temperature, thus thermography allows one to see variations in temperature. Fernández-Caballero et al. [41] detected human bodies using time sequenced thermographic images and real-time processing. This example means that the temperature information of humans obtained by thermography can be applied in human monitoring systems, especially in terms of detection.

Furthermore, active IR sensors have been used for night vision and human observation systems. Laser rangefinder techniques are also used in IR systems, and human positioning using an IR rangefinder has been studied [44–46]. Because the wavelength of IR is smaller than visible light, IR has the property of minimal scattering compared with visible light. Thus, sensing in darkness and/or smoky environments can be realized with IR. However, there are some problems in terms of the trade-off between range resolution and system complexity for the same reasons as in the optical approaches.

1.2.4 Ultrasound Sensor

Ultrasonic wave involves sound waves which have frequencies larger than 20 kHz. An ultrasound sensor is an active sensor which uses ultrasonic sound to estimate the range
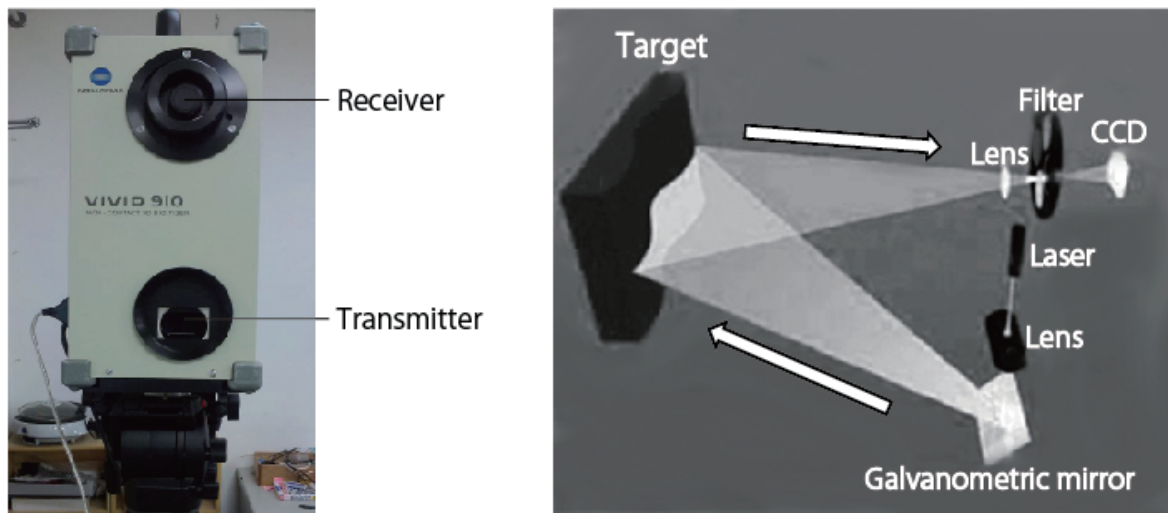
Figure 1.2: Picture of 3D laser rangefinder (VIVID910) (Left) and its system configuration [40] (Right).
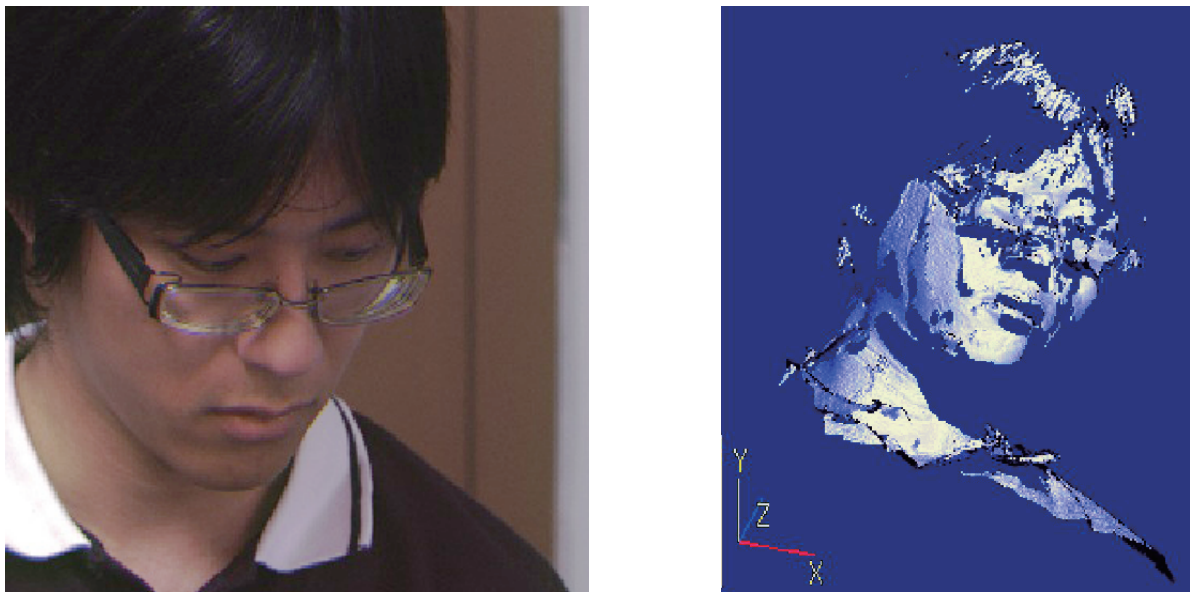
Figure 1.3: Human imaging example using the laser rangefinder. Picture of human face target (Left) and imaging result using a VIVID910 (Right).

and motion of a target. Various imaging techniques with ultrasound waves have been developed for medical applications [49–51]. This is because these waves can propagate
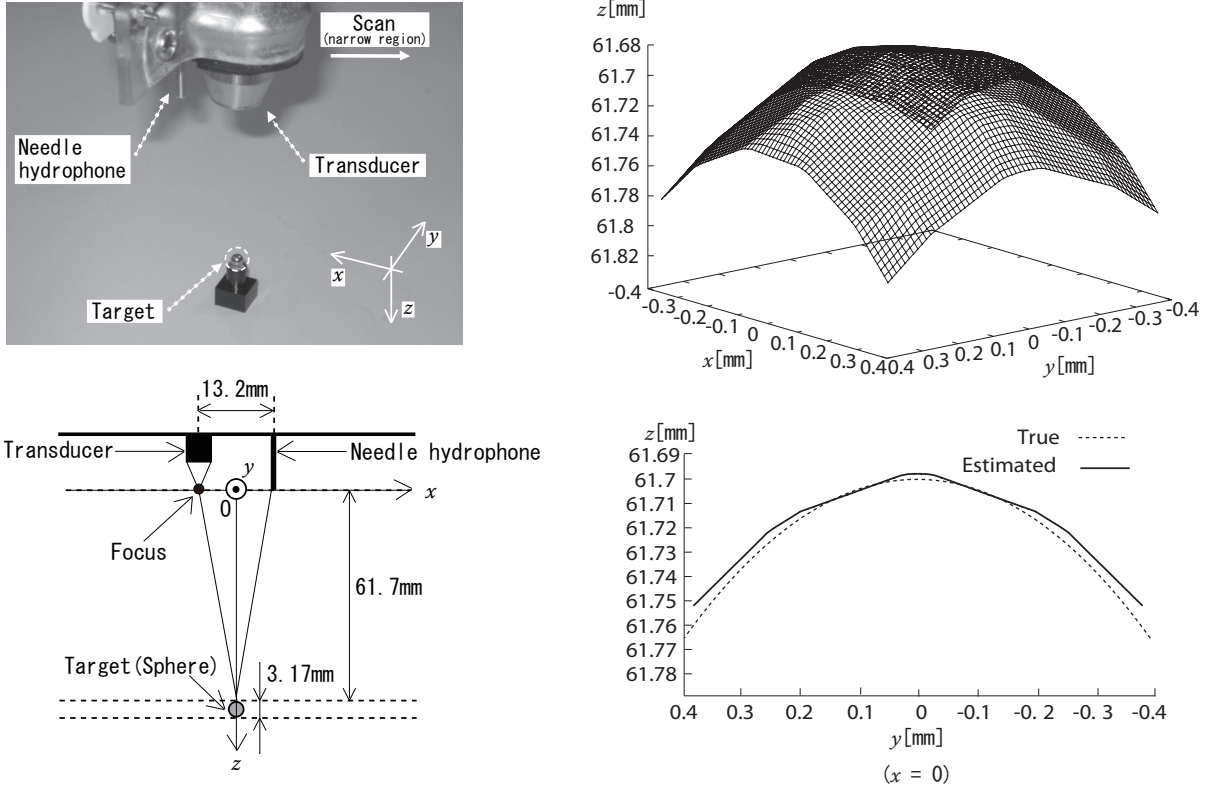
Figure 1.4: High-resolution shape estimation example using an ultrasound sensor [52]. Experimental site (Top left), outline of the vertical section of the ultrasound imaging system (Bottom left), 3-D image (Top right) and its vertical section of $x = 0$ (Bottom right).

through human organs and tissue while optical methods cannot. Furthermore, a device for ultrasonic signals is less expensive and simpler compared to that for radio waves because the sampling rate of an ultrasound wave is lower than for a radio wave. Consequently, ultrasonic techniques have also been used successfully for many low-cost nondestructive inspection applications [52–55]. Fig. 1.4 shows an example of high-resolution ultrasound imaging system and the estimated shape of a small spherical target [52]. The maximum error of the image estimated by the algorithm described in Section 1.4.3 was 8 μm with a transmitting wavelength of 700 μm using the simple system shown in Fig. 1.4. This result indicates that ultrasound sensing has great potential for super-resolution three-dimensional imaging.

For human monitoring applications, target positioning and motion recognition techniques have been studied using ultrasound propagated in air. These are based on signal processing techniques that were originally proposed for radar systems including a
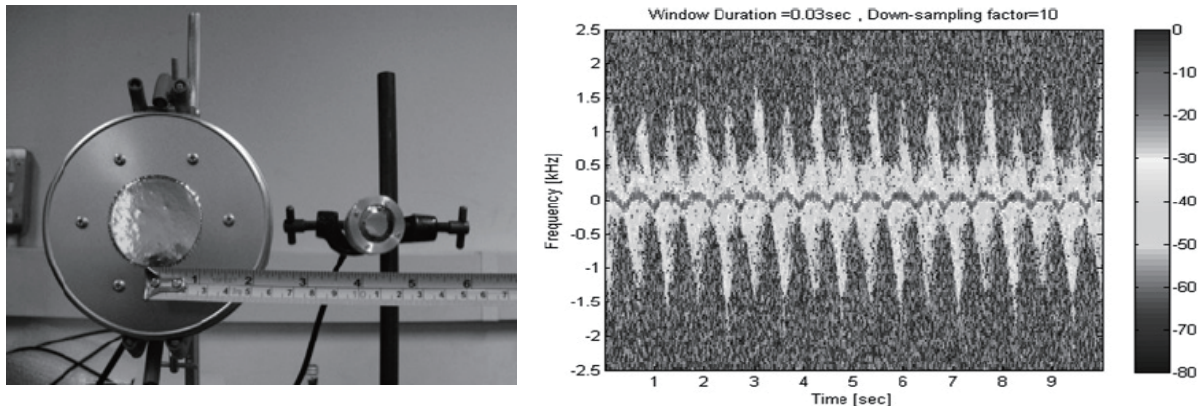
Figure 1.5: Picture of simple ultrasound Doppler sensor (Left) and measured time-frequency distribution corresponding to a pedestrian target on a treadmill (Right) [63].

moving target indicator [56–58], interferometry [59], tracking filter [60, 61] and Doppler sensors [62–64]. Balleri et al. [63] showed a time variation of Doppler frequencies corresponding to walking motion. Fig. 1.5 shows a picture of the ultrasound Doppler sonar and a time-frequency distribution of a pedestrian target on a treadmill, where frequency corresponds to radial velocity of the target's motion (detailed description is in Section 1.3.1). Relatively large frequencies of arms' and legs' movements are confirmed. This investigation showed that the motion feature of human can be detected by the simple sonar.

The propagation range for this type of wave is narrower than for radio waves, and the transmitting and receiving devices are more sensitive to the surrounding environment. In general, the velocity of ultrasound depends significantly on the temperature and pressure of the air. Therefore, ultrasound sensors cannot be used in the event of fire, which means that implementation in rescue robots is difficult. The ultrasonic devices for robust and wide-range measurements of human sensing in air are still under development and research [65, 66]. In addition, sensor fusion techniques with radio waves have great potential for human sensing [67].

1.2.5 Radar Techniques

Radio waves have advantages in high range resolution, and can be applied in difficult environments where visible rays and ultrasonic waves cannot be used, such as in smoke and fire. Radio detection and ranging (Radar) has been developed for measurement of the atmosphere, space debris, underground and so on. Since the end of 20th century, the application of radar to human sensing has been widely investigated with increasing interest for security systems. With the dissemination of wireless systems in various fields, passive radar systems are notable for use in indoor intruder detection and positioning.

Many positioning algorithms for passive radars have been proposed using a Wireless Local Area Network (WLAN) based on the IEEE 802 standards such as WiFi (802.11) and WiMAX (802.16) [68–71], digital video terrestrial broadcasts [72] and the global system for mobile communications [73]. These systems detect a cross-ambiguity function $\chi(\tau, f)$ which generates a range-Doppler map, expressed by [68]:

$$|\chi(\tau,f)|^2 = \left| \int_{-\infty}^{\infty} u(t)s^*(t-\tau)\exp(j2\pi ft)\mathrm{d}t \right|^2, \tag{1.1}$$

where $s(t)$ and $u(t)$ are the reference and the echo signals, $*$ is the complex conjugate and $j = \sqrt{-1}$. τ and f define the time-delay corresponding to range and the Doppler frequency. Chetty et al. [69, 70] presented a human positioning algorithm and its application examples based on Eq. (1.1) with a single receiver or a small number of receivers. These examples indicated that the Doppler shift of a pedestrian is accurately determined by a few receivers in a room with a single WiFi access point and some fixed obstacles. However, these systems are only able to estimate range to the order of 1 m and are unable to provide shape information, so their application to three-dimensional imaging of shape and motion is difficult.

On the other hand, classical active radar systems can acquire more accurate shape and motion information compared with passive radars. For moving target imaging, a number of effective algorithms are known, including inverse synthetic aperture radar (ISAR) [74–77], range-Doppler interferometry [78,79] and time-reversal (TR) [80,81] techniques. These techniques were developed for purposes other than robot or indoor monitoring systems. Consequently, the system model characteristics (frequency and bandwidth of transmitting signals, size, shape and motion of targets, and measurement environments) are unsuitable for human sensing. However, about ten years ago, these radar techniques and their advances became applicable to radar human imaging, because of technical improvement in radar hardware and computers and the regulations on the permissible output power for radio waves with broad bandwidth (UWB signals). To realize human sensing using high-frequency transmitted signals, micro-Doppler radar and UWB radar techniques for human sensing applications have been an active research area. Thus, the focus is on these techniques in the following sections.

1.3   CW Micro-Doppler Radar Techniques

Conventional optical human sensing systems require complicated and high-cost processing systems and/or time-consuming procedures to obtain information on movements and accurate positions. To realize motion recognition and identification with a simple system, CW micro-Doppler radar techniques have been widely studied, and many researchers have applied this to human tracking and identification. This section introduces the basics of CW micro-Doppler radar sensing [82,83] and various recent studies on motion identification and imaging of people [84–109].

1.3.1 Principle and Procedure of CW Micro-Doppler Radar

In this subsection, the definition and the description of the micro-Doppler effect and a basic procedure of the conventional CW micro-Doppler radar sensing are explained. First, to clarify effectiveness of the micro-Doppler radar, its features and a difference between conventional mean-Doppler and micro-Doppler effects are discussed. In radars which use microwaves, the modulation due to slight vibration and rotation, called micro-motion, induce frequency modulation on the returned signal and generates sidebands about the Doppler frequency shift of the target's body. This phenomenon is called the micro-Doppler effect [82, 83], and motion information of various human body parts can be detected by extracting their micro-Doppler frequencies. In contrast, conventional Doppler radars acquire mean velocity of targets. For instance, ISAR extracts Doppler frequencies of targets for a motion estimation process. In this process, ISAR assumes that target is rigid body and slight motion changes of target's surface and various parts of a target are ignored [74, 75]. Many other conventional radar imaging techniques are based on this assumption and detection of micro-motion is not considered. Consequently, for human sensing, conventional Doppler radars acquire only mean-Doppler frequency corresponding to motion of whole human body, and acquisition of information on micro-motion of each body part, such as arm-swing and body-oscillation, is thus difficult. On the other hand, the micro-Doppler radars acquire radial velocity of each body part because of using relatively high-frequency microwaves for transmitting signals. Thus, micro-Doppler radar is effective for extraction of human motion details and has become active research area for various human monitoring applications.

The micro-Doppler radar can be mathematically formulated same as the conventional mean-Doppler radar. In coherent radar, the variations in range direction cause a phase change in the returned signal from a target. Thus, the Doppler frequency shift that represents the change of phase function with time can be used to detect micro-motions of a target. Here, a mono-static radar and CW signal is assumed as the transmitting signal, which is expressed as:

$$s_{\text{Tc}}(t) = Ae^{j(2\pi f_0 t + \phi_0)}, \tag{1.2}$$

where A is the amplitude, f_0 is the frequency and ϕ_0 is the initial phase. In the micro-Doppler radar systems, f_0 is approximately 1-100 GHz. The reflected echo from a point scatterer has a time varying phase $\phi(t)$, and can be given by:

$$s'_{\text{R}}(t) = \eta Ae^{j[2\pi f_0 t + \phi_0 + \phi(t)]}, \tag{1.3}$$

where $\eta < 1$ is the ratio of the received amplitude to A. Consequently, the reflected signal after demodulation from N multiple scatters is expressed as:

$$s_{\text{R}}(t) = \sum_{i=1}^{N} \eta_i Ae^{j\phi_i(t)}. \tag{1.4}$$

11
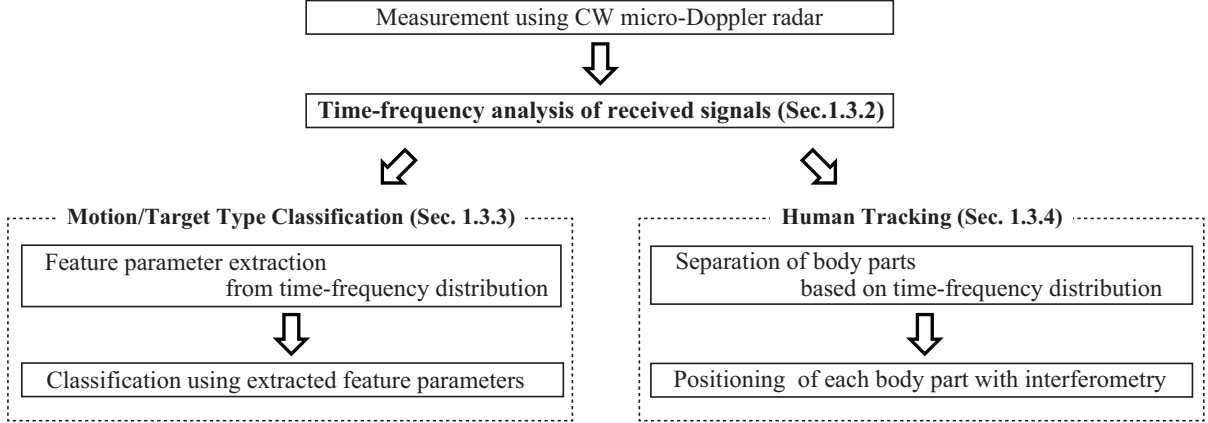
Figure 1.6: Basic procedure of target classification and tracking of humans using CW micro-Doppler radar.

The distance between the radar and the i-th scatterer is defined as R_i, and the radial velocity of the scatterer is defined as $v_{\mathrm{d}i}$. With these parameters, $\phi_i(t)$ is expressed as:

$$\phi_i(t) = -2\pi \left(\frac{2R_i}{\lambda} - \frac{2v_{\mathrm{d}i}t}{\lambda} \right), \tag{1.5}$$

where $\lambda = c/f_0$ is the wavelength and c is the speed of light. Thus, the Fourier transform of $f_{\mathrm{R}}(t)$ is expressed as:

$$S_{\mathrm{R}}(f) = \sum_{i=1}^{N} \eta_i A \delta \left(f - f_{\mathrm{d}i} \right), \tag{1.6}$$

where $\delta(f)$ is Dirac's delta function, and f_{d} is called the Doppler frequency expressed as:

$$f_{\mathrm{d}i} = \frac{2v_{\mathrm{d}i}}{\lambda}. \tag{1.7}$$

As shown in Eqs. (1.6) and (1.7), the micro-Doppler effects are extracted as the Doppler frequencies of the received signal, and the radial velocity of each scatterer is derived from the Doppler frequency spectrum.

The conventional CW micro-Doppler radar systems are mainly used for motion/target classification (Section 1.3.3) and tracking of humans (Section 1.3.4). Fig. 1.6 shows the outline of the micro-Doppler radar signal processing for these applications. These applications use micro-Doppler signatures extracted by time-frequency analysis of received signals (Section 1.3.2). The following subsections introduce several represented approaches for each part of Fig. 1.6, and review conventional studies.

1.3.2   Time-Frequency Analysis for Detection of Micro-Doppler Signatures

To extract the Doppler frequency, the frequency spectrum of the received signals must be determined. Moreover, the radial velocities (corresponding to the Doppler frequencies) of targets generally have time-variations. Thus, the micro-Doppler radar systems often use time-frequency analysis algorithms to obtain the time-variation of the spectrum. This section reviews the time-frequency analysis algorithms. Although a large number of time-frequency analysis algorithms have been proposed [110, 111], the focus in this work is on several algorithms which are often used for micro-Doppler radars.

Short-Time and Sliding-Window Discrete Fourier Transform

The most commonly used time-frequency analysis algorithm is the short-time Fourier transform (STFT). The STFT calculates the Fourier transform of each local section of the signal extracted using a window function which is non-zero for only a short period of time. The STFT of the received signal $s_\mathrm{R}(t)$ is determined by:

$$\mathrm{STFT}(t, f_\mathrm{d}) = \int_{-\infty}^{\infty} s_\mathrm{R}(t + \tau) w(\tau) \mathrm{e}^{-2\pi f_\mathrm{d}\tau} \mathrm{d}\tau, \tag{1.8}$$

where $w(t)$ is the window function. The STFT is obtained by sliding the window along the signal. In particular, if the STFT is evaluated for every time-shift of the window, this algorithm is called the sliding-window discrete Fourier transform (SDFT) [112]. The magnitude squared of the STFT is called the spectrogram, and is often used for displaying the results. The spectrogram is expressed as:

$$P_\mathrm{ST}(t, f_\mathrm{d}) = |\mathrm{STFT}(t, f_\mathrm{d})|^2. \tag{1.9}$$

The STFT is a popular algorithm because of its relatively short calculation time. Its disadvantage is in the trade-off between time and frequency resolutions, called the Gabor limit. Improvement in the frequency resolution is realized by a wide window function, which leads to a loss in time resolution. Consequently, STFT and SDFT do not realize good time and frequency resolutions simultaneously. Thus, in practice, the width of the window function $w(t)$ is an important parameter.

Many micro-Doppler radar analyses using STFT, of a human walking, have been performed. [84] and [85] show the STFT spectrogram for three types of walking motion: swinging both arms, swinging only one arm, and no arm motion, which extracts the difference in these motions using the image processing approach. Sume et al. [86] investigate the spectrogram of a pedestrian round a corner, and detect the human target using this spectrogram based on a moving target indicator algorithm. Many measurement results with STFT or SDFT for various motions and target types are given in [87–100] and in numerous other proceedings and papers. These indicate that although the appropriate

setting of the resolution with STFT or SDFT is difficult, micro-Doppler radar applications normally use these methods because of their simplicity.

Smoothed Pseudo Wigner Distribution

A smoothed pseudo Wigner distribution (SPWD) is a high-resolution time-frequency analysis method, which does not have the trade-off between time and frequency resolution. SPWD is acquired by smoothing the Wigner distribution. The Wigner distribution of the received signal is determined based on the Wiener–Khinchin's theorem as:

$$\mathrm{WD}(t, f_\mathrm{d}) = \int_{-\infty}^{\infty} s_\mathrm{R}(t + \tau/2) s_\mathrm{R}^*(t - \tau/2) \mathrm{e}^{-2\pi f_\mathrm{d}\tau} \mathrm{d}\tau. \tag{1.10}$$

The right-hand side of this equation expresses the Fourier transform of a time-varying auto-correlation function without time-averaging. According to the Wiener–Khinchin's theorem, the Fourier transform of the auto-correlation function is the power spectrum; thus Eq. (1.10) determines the power spectrum at all times with maximum frequency resolution. This means that the time-frequency resolution of the Wigner distribution is a physical limitation. Since averaging is not conducted, however, the Wigner distribution generates many cross-terms due to interference of multi-frequency components. Smoothing of the Wigner distribution is effective in rejecting the cross-terms, and is known as the smoothed pseudo Wigner distribution (SPWD) [111]. The SPWD is determined by:

$$\mathrm{SPWD}(t, f_\mathrm{d}) = \int_{-\infty}^{\infty} \Phi(t - t', f_\mathrm{d} - f_\mathrm{d}') \mathrm{WD}(t', f_\mathrm{d}') \mathrm{d}t' \mathrm{d}f_\mathrm{d}', \tag{1.11}$$

where $\Phi(t, f_\mathrm{d})$ is the smoothing function expressed as:

$$\Phi(t, f_\mathrm{d}) = \mathrm{e}^{-(t/\sigma_\mathrm{t})^2} \mathrm{e}^{-(f_\mathrm{d}/\sigma_\mathrm{f})^2}, \tag{1.12}$$

where σ_t and σ_f are the parameters that control the resolution. With a suitable setting of σ_t and σ_f, we can acquire a high-resolution time-frequency distribution with few cross-terms compared with STFT. Therefore, appropriate setting of the smoothing parameters σ_t and σ_f is very important in practice.

SPWD and related algorithms have been used for motion estimating in ISAR imaging with Doppler radar system [113, 114]. For micro-Doppler radar, SPWD analysis of simple micro-motion was investigated with numerical simulation by Chen et al. [82, 83]. However, their assumed motion is very different from human motion. Zhang [101] investigated the SPWD of a pedestrian, and discussed the comparison with STFT. However, his discussion was from the perspective of the resolution of time-frequency distributions, and positioning and imaging were not considered. This can be predicted because a complete rejection of cross-terms is difficult, interference from cross-terms and targets might be a serious problem for imaging and positioning. In contrast, the resolution of imaging using SPWD

is better than that using STFT. However, the calculation time of SPWD is larger than STFT. Considering these points, the imaging quality and real-time capability for STFT and SPWD need to be compared, and this is investigated in Chapter 2.

Other Representations

One of the other popular time-frequency representations is Wavelet Transform which is used for feature extraction from moving targets. The wavelet transform can provide the frequency of the signals and the time associated with those frequencies. Thayaparan et al. [102] analyzed the micro-Doppler signatures of a helicopter and a person walking using wavelet transforms. However, the same problem as STFT in terms of the trade-off between time and frequency resolution exists. In addition, the noise tolerance is inadequate for human sensing. Many other time-frequency analysis methods have been proposed to realize high-resolution (such as the SPWD) and reliable representation (like the STFT and SDFT). Recently, the more popular methods have been an S-method [116] and a Hilbert-Huang transform [117]. The S-method is defined by the STFT of the received signal as:

$$\mathrm{SM}(t, f_\mathrm{d}) = \int_{-\infty}^{\infty} P(\theta)\mathrm{STFT}(t, f_\mathrm{d} + \theta)\mathrm{STFT}^*(t, f_\mathrm{d} - \theta)\mathrm{d}\theta, \qquad (1.13)$$

where $P(\theta)$ is the frequency domain window. The cross-terms which occur when increasing the resolution are rejected by this window function. Oróvic et al. [103] showed the time-frequency distribution of arm and torso movements in various walking motions using the S-method. However, the setting of suitable $P(\theta)$ was difficult, and improvement in performance compared with STFT and SDFT was slight. The Hilbert–Huang transform provides high-resolution time-frequency distribution without cross-terms, which is based on the determination of the Hilbert spectrum for each intrinsic mode function of the signal. The Hilbert–Huang spectrum of a pedestrian was presented by Fairchild and Narayanan [104]. However, its calculation time was too long and control of the time-frequency resolution was difficult. Many other high-resolution time-frequency representations have been proposed, but their calculation times were also too long and their appropriate parameter settings are still important research tasks [110]. Thus, the basic methods, the SDFT and SPWD, are used and compared in this study.

1.3.3 Motion/Target Type Classification Algorithms

The motion features in time-frequency distributions can be recognized as described in the previous section. Based on these features, methods to classify and identify motion and target type have been proposed. Most of conventional researches extract feature parameters from the time-frequency distribution, and classify motion/target types using a variety of discriminant or cluster analysis algorithms. This subsection introduces popular algorithms, and reviews their application examples in CW micro-Doppler radar sensing.

Perceptrons

A perceptron is the simplest method used to find a linear separating hyperplane in feature space which separates classes of objects or events [118,119]. In this method, a separating hyperplane is determined from a training data set, and unlabeled input data is classified by a comparison with the determined separating plane. The left side of Fig. 1.7 shows a schematic of a perceptron for 2 class separation in 2-dimensional feature space. Let us consider the training data set D and a set of n points of the form:

$$D = \{(\mathbf{x}_i, y) | \mathbf{x}_i \in R^p, y_i \in \{-1, 1\}\}_{i=1}^n \tag{1.14}$$

where y_i is a label of $\mathbf{x_i}$ which is either 1 or -1. The perceptron determines a maximum-margin hyperplane that separates $\mathbf{x}_i$ of the class 1 and -1. The linear hyperplane is expressed as:

$$\mathbf{w}^{\mathrm{T}}\mathbf{x} + b = 0, \tag{1.15}$$

where $^{\mathrm{T}}$ denotes the transposition, $\mathbf{w}$ is a weight vector and b is the intercept. Here, the margin between the hyperplane and $\mathbf{x_i}$ is minimized under the condition that the target class of the training data set is correct. This optimization problem is formed as:

$$\max_{\mathbf{w}, b} \min_{i=1\cdots n} \frac{\mathbf{w}^{\mathrm{T}}\mathbf{x}_i + b}{\|\mathbf{w}\|},$$
$$\text{sub. to} \quad \text{sign}(\mathbf{w}^{\mathrm{T}}\mathbf{x}_i + b) = y_j \ (j = 1, \cdots, n), \tag{1.16}$$

where $\text{sign}(x)$ is a signum function. Eq. (1.16) can be simplified as [119]:

$$\min_{\mathbf{w}, b} \frac{1}{2}\|\mathbf{w}\|^2,$$
$$\text{sub. to} \quad y_j(\mathbf{w}^{\mathrm{T}}\mathbf{x}_i + b) \geq 1 \ (i, j = 1, \cdots, n). \tag{1.17}$$

Then, unlabeled data is classified using the hyperplane determined using the training data set. A label of an unlabeled query data $\mathbf{x}_{\mathrm{q}}$ is determined by:

$$y(\mathbf{x}_{\mathrm{q}}) = \begin{cases} 1 & (|\mathbf{x}_{\mathrm{q}}| \geq \mathbf{w}_{\mathrm{opt}}{}^{\mathrm{T}}\mathbf{x} + b_{\mathrm{opt}}) \\ -1 & (|\mathbf{x}_{\mathrm{q}}| < \mathbf{w}_{\mathrm{opt}}{}^{\mathrm{T}}\mathbf{x} + b_{\mathrm{opt}}) \end{cases}, \tag{1.18}$$

where $\mathbf{w}_{\mathrm{opt}}$ and b_{opt} are estimated parameters by solving the problem of Eq. (1.17).

For the case where the training data cannot be separated without error, Cortes and Vapnik [122] propose a modified maximum margin idea that allows for mislabeled examples, terming this technique the soft-margin hyperplane. The right side of Fig. 1.7 outlines the soft-margin hyperplane. This technique introduces slack variables ξ_i which measure the degree of misclassification of the data as shown in this figure. The hyperplane is

determined by optimizing a trade-off between a large margin and a small error penalty. Thus, the optimization problem of Eq. (1.17) is modified as:

$$\min_{\mathbf{w},\xi,b} \frac{1}{2}\|\mathbf{w}\|^2 + C\sum_{i=1}^{n}\xi_i,$$

$$\text{sub. to} \quad y_j(\mathbf{w}^{\mathrm{T}}\mathbf{x}_i + b) \geq 1 - \xi_i \ (i,j = 1, \cdots, n), \tag{1.19}$$

where C is a constant to control the balance of the first term (maximization of margin) and the second term (minimization of penalty).

Some researchers use the classification methods with the perceptrons for micro-Doppler radar systems [85, 120, 121]. Li et al. [85] realized the classification of arm-motion in walking with a soft-margin perceptron. However, the classification accuracy was 80-90 % with an input time duration of 7 s. These were insufficient values for human identification applications in real-time. The perceptrons are easily improved with advanced algorithms such as a support vector machine and an artificial neural network, which can realize more accurate separation using a non-linear hyperplane. Thus, many target classification and identification algorithms using CW micro-Doppler radars used these advanced algorithms.

Support Vector Machine

The support vector machine (SVM) is one of effective discriminant analyses capable of determining non-linear separating hyperplanes between two classes [123–126] based on the perceptron. Fig. 1.8 shows a schematic of an SVM in 2-dimensional feature space. Given a training data set, each element of which belonging to one of two classes, the SVM makes a model that assigns new examples into one class or the other. The basic concepts of the SVM are:

- Conduct a non-linear transform from input space to a high-dimensional feature space, which can classify the input data with a linear separating plane.

- In the high-dimensional feature space, the linear separating hyperplane is determined by the perceptron with Eq. (1.17) or Eq. (1.19).

The SVM can perform non-linear classification using the kernel function, which implicitly transform their inputs into high-dimensional feature spaces. Let us consider the non-linear separation of a feature vector $\mathbf{x}$. The kernel function $K(\mathbf{x}, \mathbf{x}')$ expresses both the transform to high-dimensional space and the distance between $\mathbf{x}$ and $\mathbf{x}'$ after the transform [123]. Using $K(\mathbf{x}, \mathbf{x}')$ and Eq. (1.15), the separating plane determined by the SVM is expressed as:

$$\sum_{i=1}^{N_{\mathrm{Tr}}} w_i K(\mathbf{x_i}, \mathbf{x}) + b = 0, \tag{1.20}$$

17
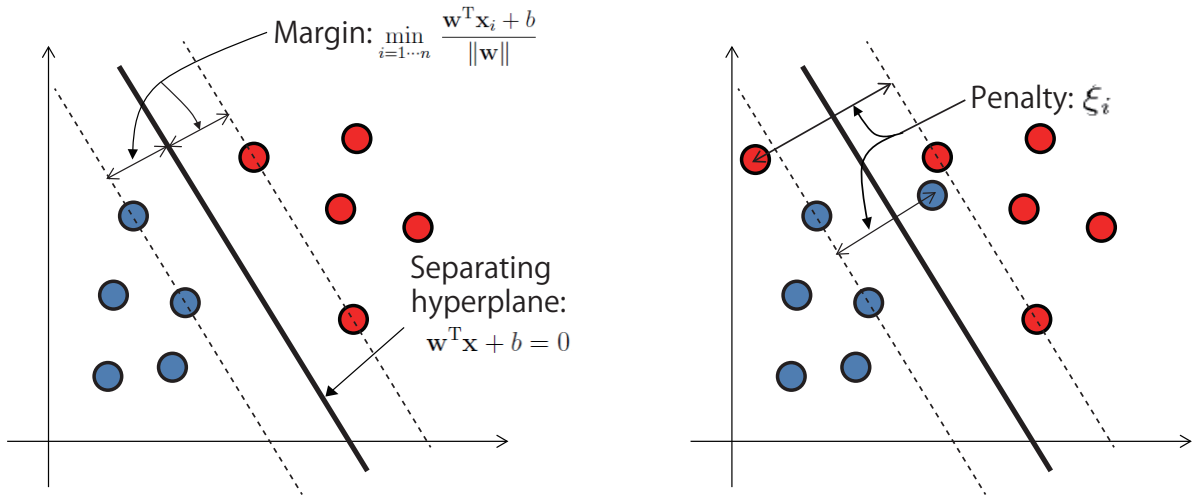
Figure 1.7: Schematic of the perceptron (Left) and the soft-margin hyperplane (Right). Color means class label of each data point.
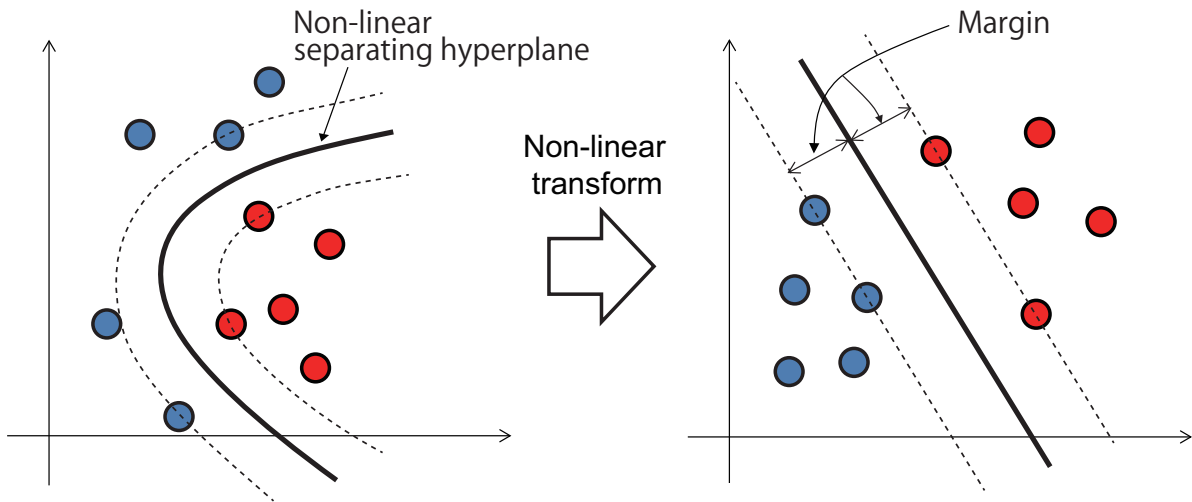
Figure 1.8: Schematic of SVM.

where N_{Tr} is the number of data. The optimum $\mathbf{w}$ and b are determined by solving the optimization problem in the same way as the perceptron. The SVM which is determined using Eq. (1.17) is called a hard-margin SVM, and when using Eq. (1.19), is called a soft-margin SVM. In practice, the soft-margin SVM is widely used because of its robustness [87, 89, 104, 125]. A variety of kernel functions are known and developed for various types of feature space. The most popular kernel function is the Gaussian kernel function, which

is known as a general-purpose function for the SVM. It is expressed as:

$$K(\mathbf{x}, \mathbf{x}') = \mathrm{e}^{-\sigma\|\mathbf{x}-\mathbf{x}'\|^2}, \tag{1.21}$$

where the parameter σ controls the expression capability of the separating plane. If a large σ is set, a complex boundary can be expressed using the kernel function. Generally, appropriate parameters are set using the cross-validation approach [124].

The SVM (including the perceptron), was originally proposed as a two-label classifier. In practice, however, multi classes of more than two often have to be dealt with. A classification method for multi classes based on the SVM has been proposed [126]. One approach commonly used in practice is to reduce the single multiclass problem into multiple binary classification problems. In this type of method, binary classifiers are built which separate between one of the labels and the rest (called one-versus-all) or between every pair of classes (called one-versus-one). Classification of data samples for the one-versus-all case is conducted by a winner-takes-all strategy, in which the classifier with the highest output function assigns the class. For the one-versus-one approach, data samples are classified by a max-win voting strategy, in which every classifier assigns the instance to one of the two classes, then the vote for the assigned class is increased by one vote, and finally the class with the most votes determines the classification outcome.

In micro-Doppler systems, the SVM has been a popular method for motion type classification in recent years. Kim and Ling [87] realized a classification of various human activities (walking, running, sitting, and so on) using the SVM in a feature space composed of parameters of time-frequency distribution, such as peak-to-peak value, cycle, and offset. Fairchild and Narayanan [104] achieved accurate human activity classification using a multi-class SVM with parameters of the Hilbert–Huang spectrum. However, for classification with sufficient accuracy using these methods, long-term data and/or time-consuming procedures are needed. For instance, the input time duration for the method in [87] required 3 s, which is not real-time for the assumed applications. Although many other applications for micro-Doppler techniques using the SVM have been proposed [88, 89], they have the same problems in terms of input/calculation time. The reasons for this are examined at the end of this section.

k-Nearest Neighbor

One other classification approach which is different from the perceptron is the technique based on the closest training samples in the feature space. k-nearest neighbor (k-NN) algorithm is a representative method of this type of classifier. Fig. 1.9 shows the schematic and procedure for k-NN in two-dimensional feature space. The training data set is first prepared, and the unlabeled data are then queried. In the classification process, k-NN algorithms calculate distance between a query point and all training data. The query point is then classified by assigning the most frequent label in k training samples nearest
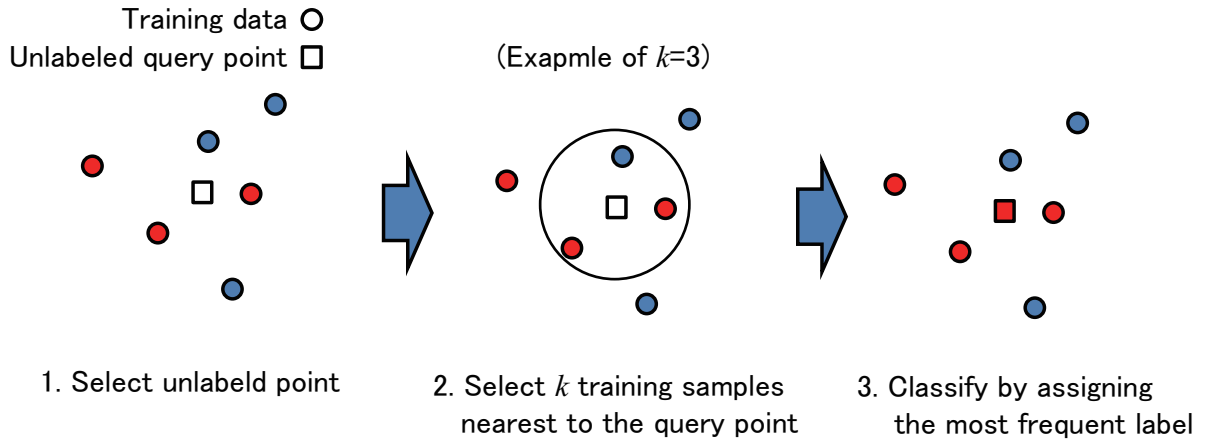
Figure 1.9: The procedure of the k-NN algorithm.

to the query point. Here, k is a user-defined constant, and if $k = 1$, the object is then simply assigned to the class of its nearest neighbor.

This algorithm is widely used for target identification in radar and other applications because of its simplicity. Moreover, classification of multi-classes is easy compared with the SVM. In micro-Doppler radar systems, the k-NN is used for motion classification with feature parameters extracted from the time-frequency distribution [63, 64, 90, 98, 105]. Liu et al. [89] proposed a fall detection method for humans using 3-NN in the features space composed of mel-frequency cepstral coefficients and achieved a detection accuracy of 96%. However, the main drawback of k-NN is that a relatively large number of training data are required. In particular, to express the complex class-boundary, many training data near the boundary are needed, and the preparation of an appropriate training data set is difficult in this case.

Naive Baysian Classifer

The Naive Baysian classifier (NBC) is a probabilistic classifier based on Bayes' theorem with naive independence assumptions of feature parameters. This method is known as an effective method for document categorization problems [129, 130]. Let us consider a dependent class variable C with a small number of classes, conditional on several feature variables $F_1, F_2, \cdots, F_n$. Using Bayes' theorem, the probability model for a classifier is:

$$p(C|F_1, F_2, \cdots) = \frac{p(C)p(F_1, F_2, \cdots |C)}{p(F_1, F_2, \cdots)}. \tag{1.22}$$

Here, NBC assumes that each feature is conditionally independent of other features for a given class. This means that $p(F_i|C, F_j) = p(F_i|C)$ when $i \neq j$. With this assumption,

Eq. (1.22) can be expressed as:

$$p(C|F_1, F_2, \cdots) = \frac{1}{p(F_1, F_2, \cdots)} p(C) p(F_1|C) p(F_2, \cdots |C, F_1)$$

$$= \frac{1}{p(F_1, F_2, \cdots)} p(C) p(F_1|C) p(F_2|C) \cdots . \tag{1.23}$$

$p(C)$ and $p(F_i|C)$ can be calculated using a training data set. The classification with NBC is then conducted by:

$$\text{classify}(f_1, \cdots, f_n) = \arg \max_c p(C = c) \Pi_{i=1}^n p(F_i = f_i | C = c). \tag{1.24}$$

This algorithm is also used for the micro-Doppler radar or sonar systems [63,91,92,106]. Igal and Joseph [91] accomplished the classification of vehicles and humans using the NBC with an accuracy rate of 99 %. Generally, an advantage of the NBC is that it only requires a small number of training data to estimate the parameter compared with the k-NN. However, the superiority of NBC is unclear in the comparison with k-NN and SVM in micro-Doppler radar applications. For example, the comparisons between the performances of NBC, k-NN and SVM were carried out in [92], and showed that k-NN realized the best classification accuracy for the fall detection application. Another study of the micro-Doppler sonar, however, reported that NBC is better than k-NN for the classification of three people with different figures [63]. These studies mean that the classification performance of each algorithm is dependent on the applications. In other words, the difference in performance is dependent on the feature space and distributions of the training data set. Examples of performance comparison for these algorithms are also given in Chapters 4 and 5 of this thesis.

Other Algorithms and Summary

Other popular classification algorithms used in the CW micro-Doppler radars are the artificial neural network (ANN) and cluster analysis algorithms. In this subsection, these classifiers and application examples are briefly explained, and the summary and drawbacks of the conventional classification methods described in this section are discussed.

ANN is a typical classification method based on the perceptron. This method realizes non-linear classification using a combination (network) of the perceptrons. A number of CW micro-Doppler radar systems used this method for target classification and identification [93–95,131]. However, application to the micro-Doppler radar system has declined in recent years because of the popularization of the SVM. This is because the separating hyperplane determined by ANN is very sensitive to the setting of initial values compared with the SVM.

Another type of classification method is the cluster analysis algorithm. The advantage of this type of method is that they do not need a training data set. The k-means method is

known as one of the effective clustering methods, and this is used for motion classification in the micro-Doppler radar systems [96]. However, this method is less accurate than other algorithms described in this section because it does not use a training data set.

Based on the discussions in this section, the important issue in developing a motion identification method is the appropriate selection of the classification algorithm and its parameters with consideration for the properties of a training data set and the feature space. In addition, the common problem of these conventional techniques is the requirement for long-term data and/or complicated procedures to realize sufficient accuracy. This is because the conventional methods used only feature paramters extracted from only time-frequency distributions, and sufficient input time duration was thus needed. As a solution to this problem, the use of parameters of not only time-frequency distribution but also positioning and imaging results that are acquried in real-time can be a considered approach. For instance, velocity and direction of moving humans can be extracted from orbit of positioning results, and figure parameters such as height and arm/leg-length can be extracted from images of target shape. Incorporating these parameters to the classification and identification methods may improve their accuracy in a shorter time data. Consequently, high-resolution and real-time imaging techniques are promising for human identification applications.

1.3.4 Human Tracking with CW Doppler Radar Interferometry

The micro-Doppler effect is useful not only for motion recognition but also for the positioning of multiple targets. Positioning and tracking results can improve the performance of human motion classification and identification systems described in the previous section. Development of the method to accurately acquire this information is thus very important. Lin and Ling [107–109] proposed a CW Doppler radar interferometry approach for the multiple target separation, positioning and tracking of persons. This algorithm separates human body parts based on the differences in their Doppler frequencies, and the position of each target is estimated using an interferometer composed of a small number of antennas. Fig. 1.10 shows the antenna configuration and the block diagram of the imaging system proposed in [109]. As shown in this figure, this system is realized by a simple system composed of three receiving antennas and two frequencies. The transmitting signal is a two frequency CW signal expressed as:

$$s_{\text{Tci}}(t) = A\text{e}^{j2\pi f_a t} + A\text{e}^{j2\pi f_b t}, \tag{1.25}$$

where $f_a > f_b$. First, the Fourier transform is applied to the received signals at all antennas, defined as $S_{\text{R1}}(f)$, $S_{\text{R2}}(f)$, $S_{\text{R3a}}(f)$ and $S_{\text{R3b}}(f)$. Multiple targets are resolved as shown in Eq. (1.6). A direction-of-arrival (DOA) and distance of each separated i-th target are then estimated. With the interferometer composed of the receiving antennas
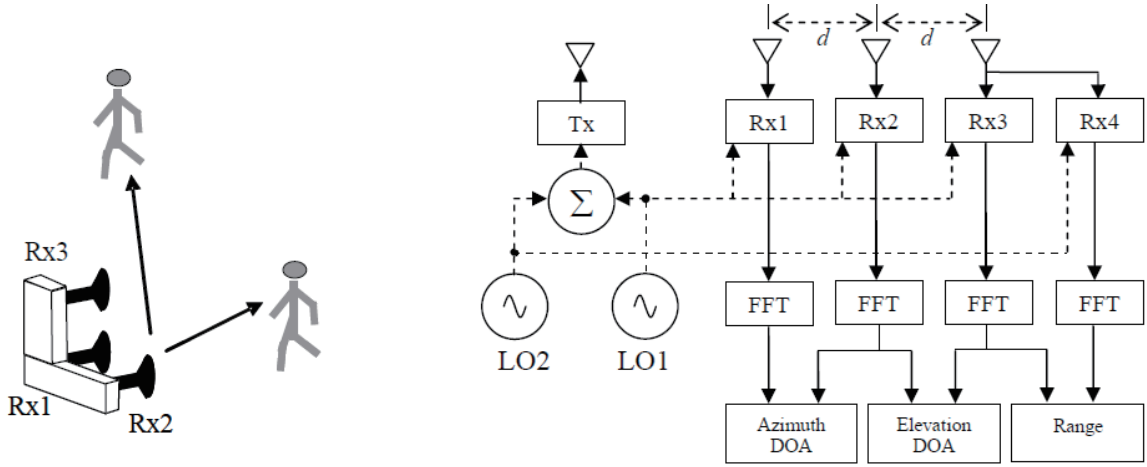
Figure 1.10: Antenna configuration (left) and block diagram (right) of the imaging system with CW Doppler radar interferometry (Lin and Ling [109]). Tx and Rx represent transmitting and receiving antennas, LO is local oscillator, FFT is fast Fourier transform, and DOA represents direction-of-arrival.

Rx$_1$ and Rx$_3$, the elevation DOA of the i-th target is determined by [107, 108]:

$$\theta_{\mathrm{EL}}(f_{\mathrm{d}i}) = \sin^{-1}\left[\frac{\angle S_{\mathrm{R1}}(f_{\mathrm{d}i}) - \angle S_{\mathrm{R3a}}(f_{\mathrm{d}i})}{(2\pi d/\lambda)}.\right], \tag{1.26}$$

In the same way, the azimuth DOA is determined by the interferometer composed of Rx$_1$ and Rx$_2$ as:

$$\theta_{\mathrm{AZ}}(f_{\mathrm{d}i}) = \sin^{-1}\left[\frac{\angle S_{\mathrm{R1}}(f_{\mathrm{d}i}) - \angle S_{\mathrm{R2}}(f_{\mathrm{d}i})}{(2\pi d\cos\theta_{\mathrm{EL}}(f_{\mathrm{d}i})/\lambda)}\right], \tag{1.27}$$

The distance is estimated by frequency domain interferometry as [109]:

$$R(f_{\mathrm{d}i}) = \frac{c\left[\angle S_{\mathrm{R3a}}(f_{\mathrm{d}i}) - \angle S_{R3b}(f_{\mathrm{d}i})\right]}{4\pi(f_a - f_b)}. \tag{1.28}$$

The human tracking [107, 109] examples using CW Doppler radar interferometry were performed, and the moving orbits were detected using only three receiving antennas. Moreover, a frontal image of a human was obtained in [108] from the experimental data. Fig. 1.11 shows the frontal image of a human target obtained from the estimated DOAs. The outline of the human shape was confirmed to some extent.

However, the resolution of these examples is insufficient to acquire the details of human shape and motion information because of:

- The acquisition of accurate ranges for all body parts is difficult because a CW is used.
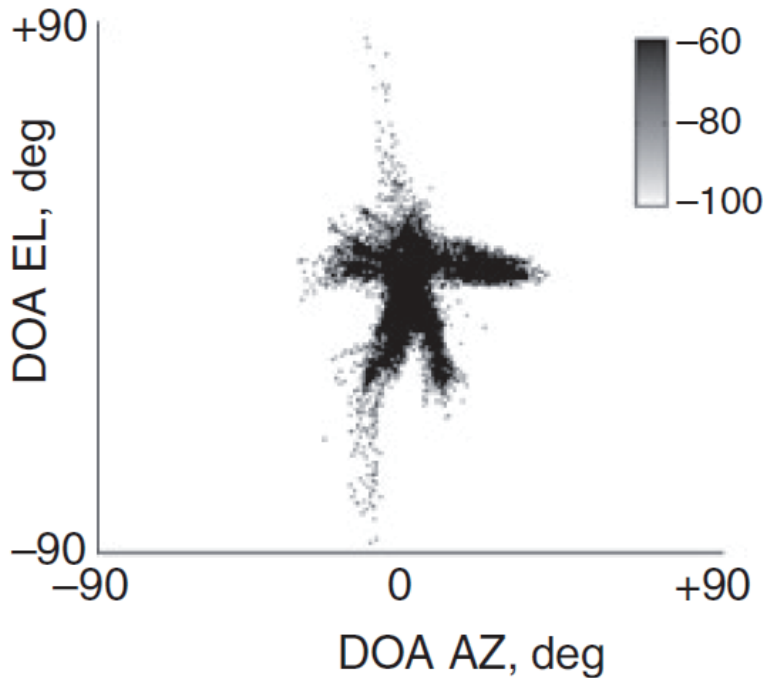
Figure 1.11: Frontal image (DOAs) of a human estimated by CW Doppler radar interferometry (Lin and Ling [108]).

- In the interferometry process, many false images occurred because it assumed all targets have different Doppler shifts, which is not satisfied in a real environment.

For these reasons, only the front view of a human outline could be confirmed as shown in Fig. 1.11. Thus, high-resolution range estimation without increasing system complexity is needed for human sensing using Doppler radar interferometry. The UWB radar techniques are good candidates as a solution to this problem.

1.4   UWB Radar Techniques

The main problem with conventional optical and radar techniques is that the acquisition of shape/motion details with a simple system is difficult because of poor range resolution. However, high-resolution tracking and imaging methods using UWB radar with a small number of antennas have been proposed in recent years. These UWB radar techniques provide a promising solution to the conventional problems. This section introduces the UWB signals, and reviews UWB radar techniques for high-resolution human sensing.
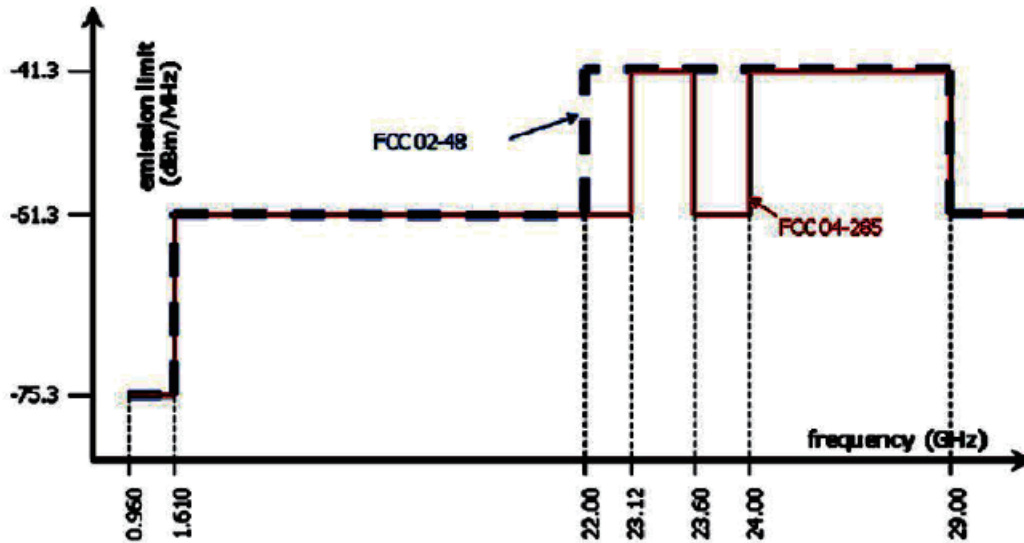
Figure 1.12: EIRP limitations on UWB signals of each frequency.

1.4.1 UWB Signals

A UWB signal is a very short pulse of a signal with a very large bandwidth. Thus, using this signal in radar systems can realize accurate range measurements, which leads to high-resolution sensing. In 2002, the Federal Communication Commission (FCC) of the United States regulated the 15 part rules concerning UWB signals [132]. The FCC defined a UWB device for civilian purposes as one with:

- a fractional bandwidth greater than 0.2,

- a bandwidth of signal greater than 500 MHz.

The fractional bandwidth and bandwidth were formulated by the Commission as $2(f_{\mathrm{H}} - f_{\mathrm{L}})/(f_{\mathrm{H}} + f_{\mathrm{L}})$ and $(f_{\mathrm{H}} - f_{\mathrm{L}})$, respectively, where f_{H} is the highest frequency of the -10 dB emission point and f_{L} is the lowest frequency of the same emission point. Fig. 1.12 shows the limitation on the EIRP (Equivalent Isotropically Radiated Power) of UWB signals. Fig. 1.13 shows the comparison between a conventional radar pulse and a UWB signal. Such short pulse can measure high-resolution range. Thus, UWB signals provide a great advantage for high-resolution, and enable proximity imaging using radar.

1.4.2 Human Positioning and Imaging Algorithms

The applications of UWB radar for human sensing have been widely studied for indoor security systems. Many high-resolution positioning methods with multi-static UWB radar
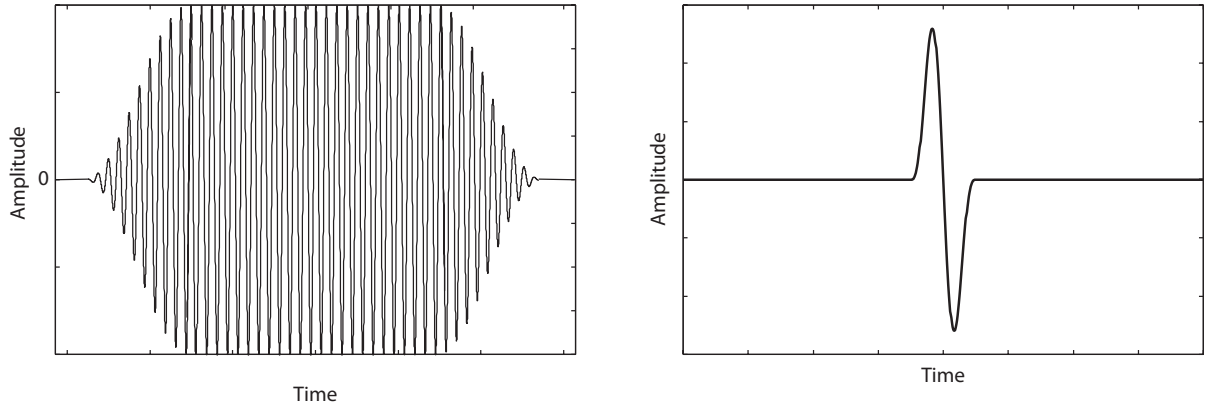
Figure 1.13: Conventional narrow band (left) and UWB signals (right).

systems including sensor networks [133–137] and multiple-input multiple-output system (MIMO) [138, 139] have been developed. These are based on classical pulse radar positioning techniques such as a tracking filter [133, 134], a migration algorithm [135, 136] and interferometry [137]. In particular, synthetic aperture radar (SAR) and time reversal (TR) techniques have been widely used and have indicated better results. In the following section, these representative conventional UWB radar positioning and imaging systems are reviewed, and their problems are identified.

SAR and ISAR Techniques

SAR is known as one of the efficient and useful techniques in pulse radar imaging systems. SAR is classically used for geographical imaging from airplanes and satellites [142], ground penetrating radar [143], and so on. The technique can be used for near-field sensing using UWB pulse radar. The principles of SAR imaging are summarized as follows. Fig. 1.14 shows the example of UWB-SAR imaging with a scanning antenna for a 2-D problem. The SAR technique coherently integrates signals observed at various places using small antennas, which create an equivalent wide antenna aperture. Two-dimensional imaging in the xz plane is considered where the mono-static antennas are located along the x-axis. The upper part of Fig. 1.14 shows the echo intensity at each antenna position. The SAR obtains an imaging result $I(x, z)$ by the summation of these echo intensities as:

$$I(x, z) = \int_{-\infty}^{\infty} s\left(X, \sqrt{(X - x)^2 + z^2}\right) dX, \qquad (1.29)$$

where $s(X, t)$ is the received signal in time t at the antenna location $(x, z) = (X, 0)$. In Eq. (1.29), the received signals focus on the target boundary, and the boundary enlightened with the amplitude intensity shown in the lower part of Fig. 1.14 can be recognized. The SAR technique has already been used for the UWB radar applications on human

26

Examples of $s\left(X, \sqrt{(x-X)^2 + z^2}\right)$

$I(x,z)$
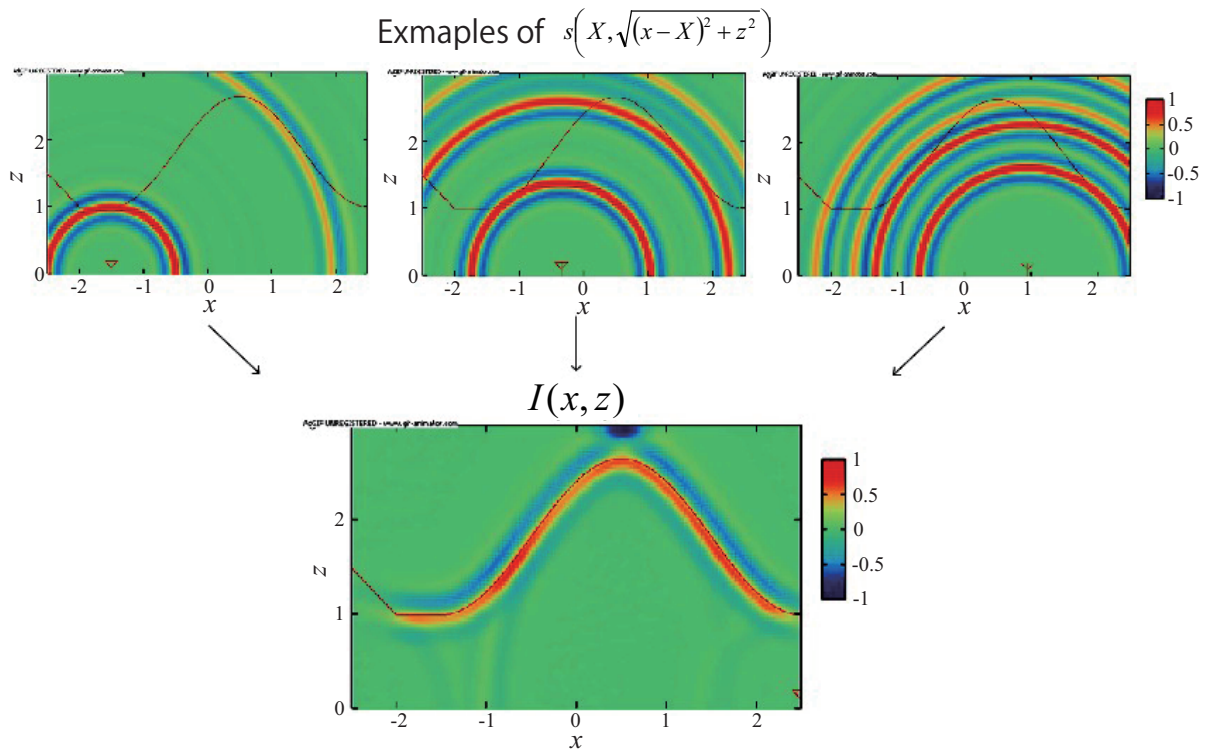
Figure 1.14: Principles and example of SAR imaging with antenna scanning. System model and received signals at various antenna positions (Above) and the imaging result using Eq. (1.29) (Below).

shape estimation [139–141]. Fig. 1.15 shows the system configuration of MIMO-SAR imaging and 3-D imaging of a mannequin with concealed weapons, using this technique as performed by Zhuge and Yarovoy [139]. Accurate shape estimates of the mannequin and weapons were achieved. However, the size of the scanning area was 130 cm × 130 cm, which is very large for the assumed applications. Other conventional techniques have also been applied to the antenna array systems but lead to complex systems that are too costly.

Although the SAR requires wide-scanning antenna and/or a large antenna array, an imaging technique with a small number of antennas based on the SAR is widely known as the inverse SAR (ISAR) technique [113, 144–148]. ISAR uses target motions instead of the antenna scanning in SAR systems, and thus images can be estimated by a small number of antennas. The target shape is extracted by the integration of signals with compensation for the estimated motion. ISAR techniques achieved shape estimation of rotating targets with estimates of motion parameters [144, 145]. Bertl et al. [146, 147] investigated the application of the ISAR to human imaging, and achieved three-dimensional scattering
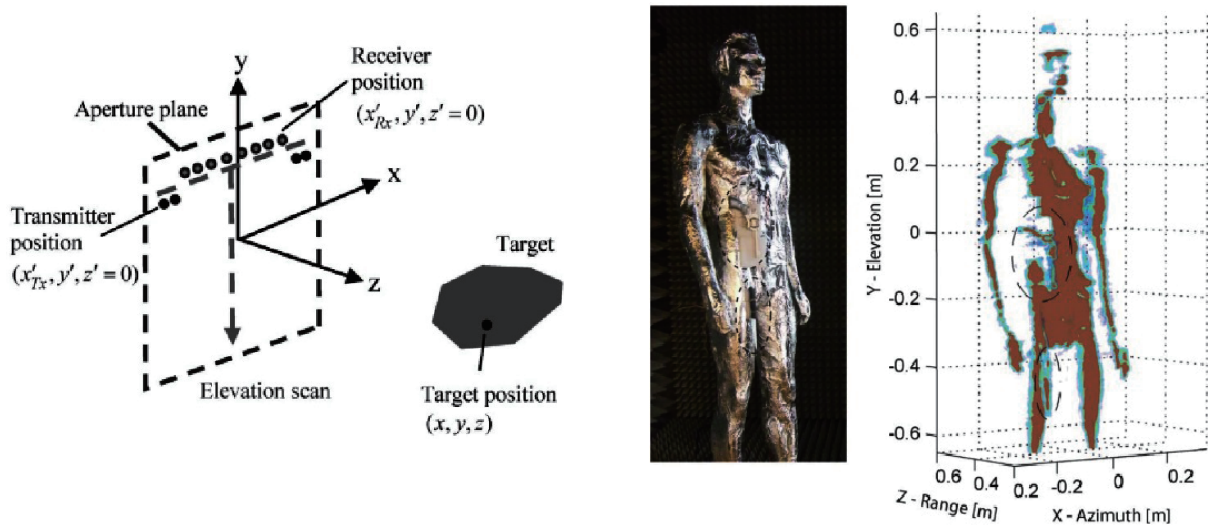
Figure 1.15: The system model of MIMO-SAR imaging (Left) and the mannequin target with concealed weapons and its estimated image (Right) shown by Zhuge and Yarovoy [139].

center extraction of an actual human target. However, they assumed that the person was rotated standing on a turntable, which was not a realistic situation. For shape estimation of a target with arbitrary motion, investigation on the modeling of targets and shape has been conducted using various time-frequency analysis and model fitting algorithms [113, 148]. However, for the intended application in this study, the problem is complex compared with their assumed model, because the target is relatively close to the antennas. This shifts the scattering centers on the target surface, depending on the relative positions of the antenna and target. In addition, human motion cannot be modeled as a simple function because it is basically arbitrary. Furthermore, these SAR-based techniques require a total search of the assumed region, and the calculation time is enormous. As such it cannot be applied to real-time operations.

TR imaging

The TR imaging algorithm [149–152] is used for positioning and tracking of scattering centers. First, the basic principles of TR imaging are explained [150]. A target is considered which is treated as M scattering centers, a linear antenna array composed of K receivers with the k-th receiver located at $\boldsymbol{r}_k$, and a single source at $\boldsymbol{r}_s$ shown as Fig. 1.16. The signals recorded at the array are time-reversed and re-emitted into the medium because the back-propagated field focuses near the active targets. The array acts as a mirror that refocuses the time-reversed signals back onto the source from which they emitted. The
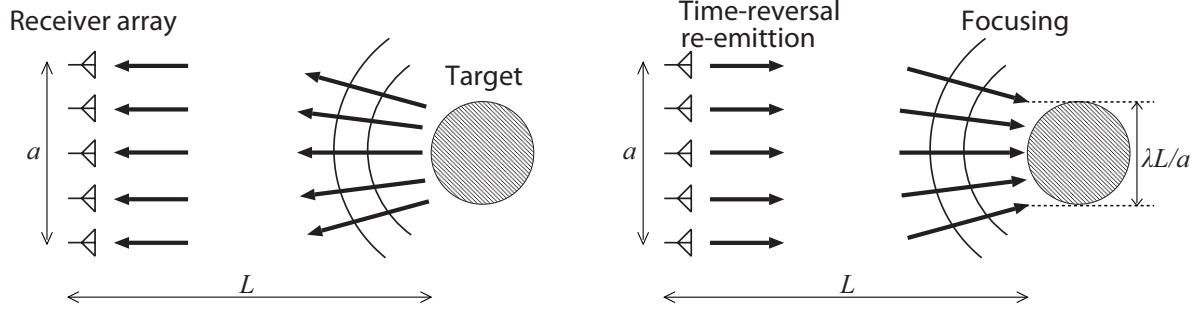
Figure 1.16: Schematic of TR imaging. Outline of Radiation and receiving process (Left) and time-reversal and focusing processes (Right).

focusing resolution is determined by the array size a, distance L and the transmitting wavelength as shown in Fig. 1.16, when $L \gg a$. Assume that a time domain pulse $s(t)$ is emitted from the transmitter at $\boldsymbol{r}_s$. The field incident on the target at $\boldsymbol{r}'$ due to the source is represented as:

$$E(\boldsymbol{r}, t) = s(t) * G_e(\boldsymbol{r}', \boldsymbol{r}_s, t), \tag{1.30}$$

where $G_e(\boldsymbol{r}', \boldsymbol{r}_s, t)$ is the Green's function representative of a source emitting in the presence of clutter and $*$ is the convolution operator. The scattered electric field at the k-th receiver $U_k(\omega)$ is expressed with the Born function and the high-frequency approximation as:

$$U_k(\omega) \simeq \sum_{m=1}^{M} B_m(\boldsymbol{r}') P(\omega) G_e(\boldsymbol{r}'_m, \boldsymbol{r}_s) G_e(\boldsymbol{r}_k, \boldsymbol{r}'_m), \tag{1.31}$$

where $B_m(\boldsymbol{r}'_m)$ is a function that represents the conversion of the excitation field $E(\boldsymbol{r}', t)$ into equivalent currents that re-radiate as secondary sources. For each receiver, the time-reversal signals $I_k(\boldsymbol{r}, t)$ are calculated as:

$$I_k(\boldsymbol{r}, t) = \int \left[\sum_{m=1}^{M} B_m(\boldsymbol{r}') P(\omega) G_e(\boldsymbol{r}'_m, \boldsymbol{r}_s) G_e(\boldsymbol{r}_k, \boldsymbol{r}'_m) \right]^* G_c(\boldsymbol{r}, \boldsymbol{r}_k) G_c(\boldsymbol{r}_s, \boldsymbol{r}) e^{j\omega t} d\omega, \tag{1.32}$$

where the subscript c emphasizes that Green's functions are computed within the imaging process. The TR image is focused on the target location by the summation for all receivers as:

$$I(\boldsymbol{r}, t) = \sum_{k=1}^{K} I_k(\boldsymbol{r}, t), \tag{1.33}$$

and calculating the total field at time $t = 0$, which corresponds to the time of arrival from the target. This method can also achieve robust imaging in a highly cluttered environment by choosing an appropriate Green's function. Because of the high-resolution and robust

capability, the TR imaging algorithm has been widely investigated in the development of an early-stage breast cancer detection method [153, 154] and through-the-wall human positioning and tracking systems [155–157]. For example, Maaref et al. [155] achieved high-resolution tracking of an actual pedestrian target behind a wall.

The general TR imaging systems explained above are composed of antenna arrays or antennas placed at various locations. TR imaging algorithms using a few antennas have been proposed in recent years [158–160]. The feature of these methods is the positive use of multipath echoes from walls and/or other fixed obstacles. Fig. 1.17 shows the system model for time-reversal imaging with a single antenna and the imaging result of a circular target in a room, which is shown in [158]. Although the actual antenna in this room is only $a^{(0)}$, a number of mirror image antennas $a^{(i)}$ ($i = 1, 2, \cdots$) can be assumed at symmetrical positions with respect to the walls of the room by considering the multipaths. The image $I(\boldsymbol{r})$ is produced using Eq. (1.33) using different antenna pairs after compensating for the time delay of the pulses. A positioning with a single antenna realized with focusing using the TR process is confirmed in Fig. 1.17.

However, the estimating region of the image is limited and its resolution is insufficient. In addition, the resolution and robustness depend highly on suitable selection of the Green's function, which is difficult. Moreover, intensive computation is required, as the calculations for these are based on, for example, the ray-tracing method [149]. The requirement of time-consuming calculations is a common problem for classical UWB pulse radar imaging algorithms which are mainly used for ground penetrating radars [161], which means that it is difficult for these conventional algorithms to achieve real-time monitoring.

1.4.3   Shape Estimation with SEABED-Class Algorithms

The most serious problem of conventional UWB radar positioning and imaging systems (and many other conventional radars and human sensing systems with other waves) is that time-consuming processes and/or complex systems are required to achieve high-resolution sensing. As an effective solution to this problem, the SEABED (Shape Estimation Algorithm based on BST and Extraction of Directly scattered waves) approach, which is a super-resolution and real-time imaging algorithm for UWB pulse radars, has been proposed by Sakamoto and Sato [162, 163]. SEABED is based on a reversible transform BST (Boundary Scattering Transform) between the received signals and the target shape, and can specify the target surface locations accurately. Fig. 1.18 shows the outline of SEABED [163]. A monostatic antenna is scanned on the $z = 0$ plane, and the antenna position is defined as $(x, y, z) = (X, Y, 0)$. At each antenna position, a UWB pulse is transmitted and the accurate range Z is estimated from the time-delay of the received signals after appropriate filtering [164]. The transform from the observed (X, Y, Z) to the target shape (x, y, z) is calculated using the transform called the inverse BST (IBST),
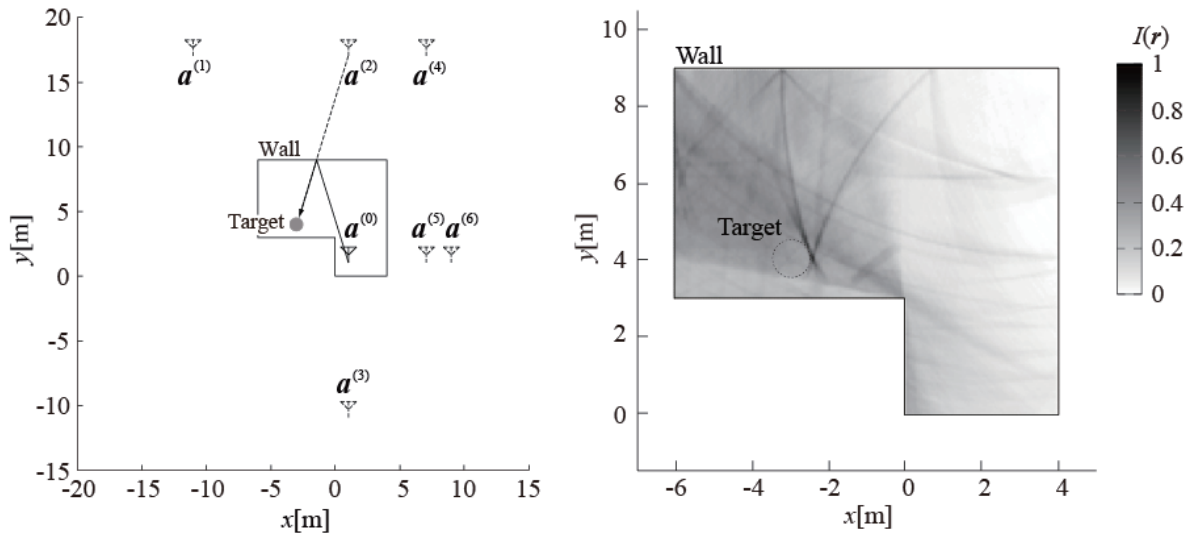
Figure 1.17: A TR imaging example using a single antenna and multipath by the wall. Assuming an imaging system composed of an actual antenna and mirror image antennas made by multipaths and a target (Left), and imaging result (Right) performed in [158].

which is expressed as:

$$\left.\begin{array}{rcl} x & = & X - Z\partial Z/\partial X \\ y & = & Y - Z\partial Z/\partial Y \\ z & = & Z\sqrt{1 - (\partial Z/\partial X)^2 - (\partial Z/\partial Y)^2} \end{array}\right\}. \tag{1.34}$$

SEABED realizes real-time shape estimation because it calculates this equation only after the ranging process. Moreover, an accurate shape is reconstructed because of the mathematically strict transform of IBST. Based on SEABED, many advanced algorithms have been proposed to realize improved robustness [52, 165] and to estimate using a variety of antenna locations [166, 167].

Although these conventional SEABED-class algorithms assume a wide scanning antenna or a large antenna array and a fixed target, extended algorithms for imaging a moving target are proposed using a small number of fixed antennas [168–172]. Matsuki et al. [169] proposed an extended SEABED for two-dimensional high-resolution shape estimation of a target with an arbitrary translational motion. Fig. 1.19 shows the basic concept of the extended SEABED. The focus of this method is the equivalence of an antenna scanning and a target motion. In this method, the target motion is estimated using the ranges obtained at three receiving antennas, and the equivalent antenna position X' is then determined based on the estimated motion. Finally, a target shape is estimated using IBST from (X', Z) to (x, z). This method has already been extended to arbitrary motion including rotation [170] and a three-dimensional problem [171]. These algorithms
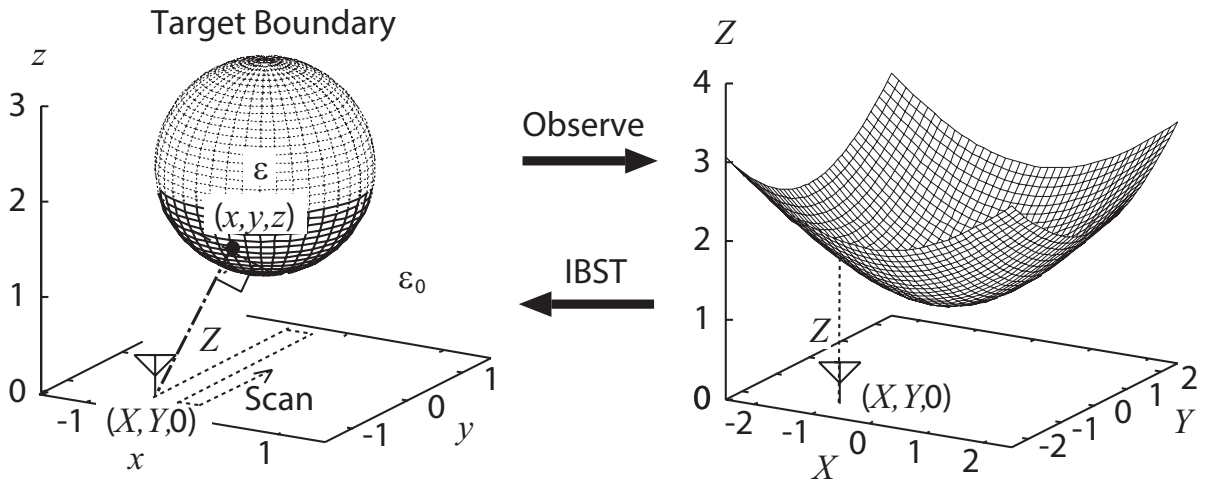
Figure 1.18: Outline of SEABED [163]. A target shape and antenna scanning (left) and observed data (right).
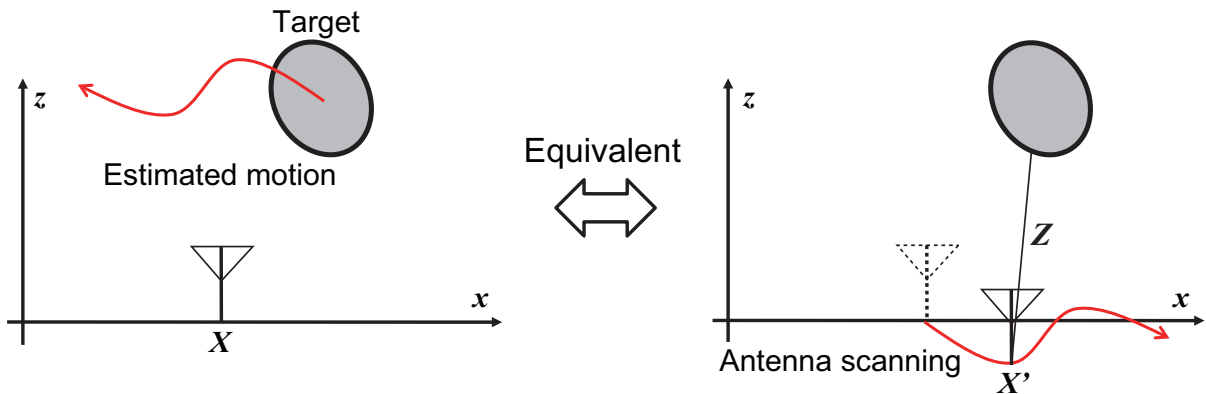
Figure 1.19: Relationship between a motion and an equivalent antenna scanning in the extended SEABED for a moving target [169].

realized high-resolution and real-time shape estimates of a moving target, whose accuracy was on the order of 1/100 of the center wavelength of the transmitting pulse.

However, because these algorithms consider only a simple and single target, it is difficult to apply these to complex targets such as the human body. The important feature of the SEABED-class algorithms is that they positively use range information acquired as peaks of the received signals. Because the shape of a human body is so complex, however, separation of echoes from various body parts is required for these algorithms. Several

approaches to extract a complex boundary were presented in [173–175]; however, their accuracy was insufficient for human imaging and an application to a moving target has not yet been reported.

1.4.4 UWB Doppler Radar Imaging

UWB Doppler radar is a combined technique of UWB and micro-Doppler radars, and has the advantages of both techniques: high-resolution capability and real-time motion recognition. Moreover, it is realized with a simple system, because it can obtain motion information with fixed antennas, similar to the CW micro-Doppler radar and SEABED-class algorithms. Recent popular application of the UWB Doppler radar is vital-sign monitoring [176–179]. These methods detect respiration and heart beat frequencies from micro-Doppler frequencies corresponding to breast motion, and estimate location by the delay of the detected signals. However, because the main purpose is to estimate respiration and heart beat frequencies, a precise positioning is not realized and an imaging application is not considered. Moreover, the applications of these methods are limited to sitting or sleeping subjects with slight movements, which is not a realistic assumption. Many researchers have challenged the application of UWB Doppler radar to a human with arbitrary motion including the detection of micro-motions using the time-frequency analysis described in Section 1.3.2 and ranging techniques using UWB signals described in this section [179–183]. The experiments and simulations in these papers estimated ranges for a moving human target, and qualitatively confirmed motion features from the spectrograms. Fogle and Rigling [179] proposed a ranging method for UWB Doppler radars using nonlinear least squares and expectation-maximization algorithms, and achieved accurate ranging of pedestrians moving in various directions. However, this method only acquires range information and is not able to provide shape information. Estimates of detailed shape/motion and their parameters have not been reported. Thus, the UWB Doppler radar techniques are still not suitable for human imaging and identification applications.

UWB radar has great potential for high-resolution imaging indicated by the SEABED-class of algorithms. In addition, the Doppler radar interferometry described in Section 1.3.4 can realize motion recognition and DOA estimations with real-time processing. Based on these, we can predict that high-performance human imaging satisfying the requirements of surveillance and monitoring systems is realized using the information of shape and motion, and these are obtained using Doppler radar interferometry and high-resolution range estimates using UWB pulses. This thesis thus deals with the combined technique of UWB Doppler radar and interferometry techniques to achieve high-resolution and real-time human imaging with small physical packaging. This combined technique is termed UWB Doppler radar interferometry, and is the focus of this thesis.

1.5 Targets of the Present Work

The targets of the present work are the development of human imaging algorithm, and the proposition of human identification algorithms using obtained images. The present study focuses on satisfaction of requirements of human monitoring systems described in Section 1.1 using UWB Doppler radar interferometry. Fig. 1.20 shows an outline of this thesis and a relationship between the present study and the conventional studies. Concrete targets of performance are summarized as:

- Shape and location of humans are obtained with a resolution with an order of 1 cm (or smaller than it).

- Acquired images are applicable to identification of several humans with various motions.

- Input time duration and total calculation time of imaging and identification processes are both within 1 s.

- These performances are realized with small number of antennas and narrow scanning area.

In this thesis, the high-resolution and real-time human imaging algorithm is firstly presented. The characteristics of UWB Doppler radar interferometry are investigated, and human imaging algorithms are proposed, which can solve several problems using this technique. Moreover, classification and separation algorithms for pedestrians based on the estimated human images are proposed.

In Chapters 2 and 3, the proposed high-resolution and real-time human imaging algorithms and their effectiveness in realistic environments are presented. Chapter 2 describes a high-resolution imaging algorithm using UWB Doppler radar interferometry, and shows its applications to multiple moving targets. A system configuration and basic imaging algorithm is first explained. As in CW Doppler radar interferometry explained in Section 1.3.4, targets are resolved in time-frequency analysis, and DOAs corresponding to each resolved target are estimated using interferometry. For the purpose of high-resolution imaging, the use of SPWD for time-frequency analysis is first considered. Moreover, to achieve range estimation with a resolution smaller than a pulse width, a range interpolation technique is introduced. An imaging example of a few revolving targets in a two-dimensional problem is shown for simplicity. The performance evaluation with numerical simulations and experiments verifies that the proposed algorithm achieves high-resolution shape estimation. Moreover, the performance of SPWD and SDFT are compared, and suitable conditions for each method are discussed. Based on the above investigations, UWB Doppler radar interferometry is applied to a numerical human model composed of multiple scatterers, and the imaging performance is clarified.
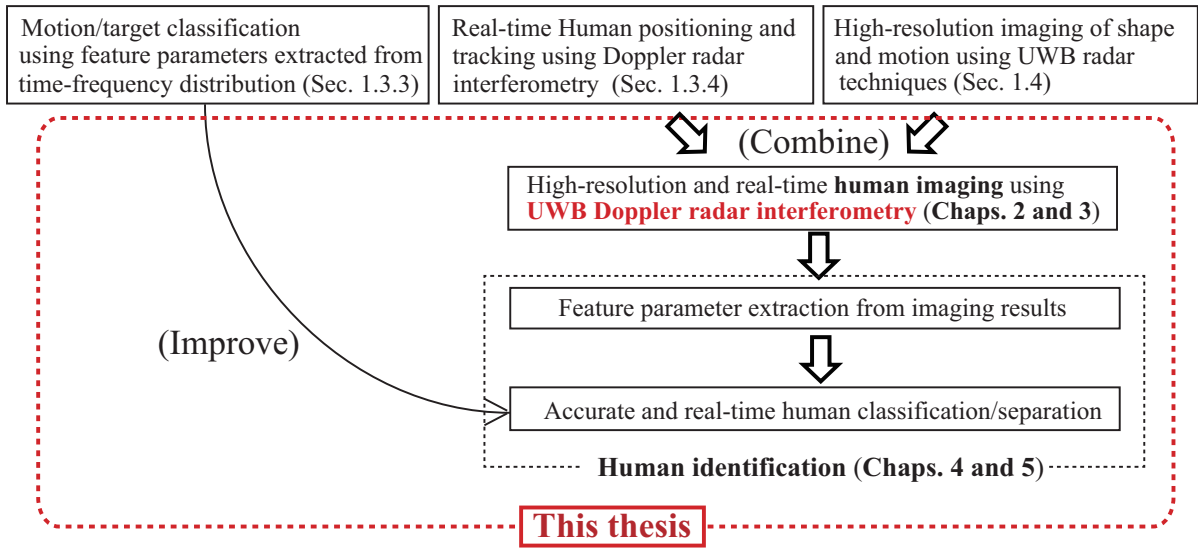
Figure 1.20: Outline of this thesis and relationship between the present study and the conventional studies described in Sections 1.3 and 1.4.

Chapter 3 presents the proposed human imaging algorithm for realistic situations. First, the false image examples in human imaging using UWB Doppler radar interferometry with experimental data are shown. With the results from this experiment and the numerical simulation conducted in Chapter 2, it is clarified that these false images are created by the interference of body parts. To resolve this problem, the mechanism for these types of false images is clarified and false image detection and rejection methods using velocity information are introduced. The experiments assume a pedestrian in an actual room and show that many false images are rejected by the proposed rejection methods. The proposed imaging algorithm achieves high-resolution and reliable human imaging in a real environment. Moreover, it is shown that accurate shape and motion parameters can be extracted from the estimated human image, and the proposed algorithm also realizes real-time imaging. Finally, the imaging examples of pedestrians walking in various directions are shown.

In Chapters 4 and 5, examples of human identification applications based on imaging results are presented. Chapter 4 describes an accurate and real-time pedestrian classification algorithm based on radial velocity features of UWB Doppler radar images. A classification of three groups of pedestrians is considered, mainly in a hospital monitoring environment: a normal pedestrian group, a group using crutches and a group with wheelchairs. In addition, a classification of more detailed pedestrian types is presented. Three types of human gait for the normal pedestrian group are assumed: with both arms swinging, holding a bag with one hand, and without swinging arms. The target group with wheelchairs is composed of two types: a pedestrian pushing a person in a wheelchair

and a person pushing himself or herself in a wheelchair. The classification of these three groups and six types of pedestrian targets is dealt with. Imaging results of these types of pedestrian with UWB Doppler radar are obtained experimentally, and the features of each pedestrian image are discussed. A feature parameter extraction algorithm from the estimated images and their radial velocity distributions are proposed, and a classification algorithm using these parameters are described. The experimental results show that accurate classifications of three groups and six types of pedestrians with real-time procedure are achieved.

Chapter 5 considers image separation and identification of two closely spaced pedestrian targets. First, the imaging example is shown of two pedestrians, the distance between whose torsos is relatively small, and a simple image separation method based on range profiles is introduced. This method is applied experimentally, and the separation accuracy of closely spaced pedestrians is found unsatisfactory. To solve this problem, an accurate separation method using a SVM is then proposed. An extraction method for training data based on range profiles is proposed, and the images are separated using the separation plane determined by the SVM using extracted training data. In addition, a method for rejecting false points existing around the separation plane is proposed. Experiments show that this method achieves accurate image separation and identification for various positions of two pedestrians.

Concluding remarks are given in Chapter 6. An overview of the proposed algorithms, their performance, and an achievement evaluation are given, and future developments for advanced monitoring systems are suggested.

Chapter 2

High-Resolution Imaging Algorithm for Multiple Moving Targets

2.1 Introduction

As described in the previous chapter, the UWB Doppler radar using interferometry techniques should have great potential in providing both moving target recognition and high-resolution imaging. This chapter proposes a high-resolution imaging algorithm with UWB Doppler radar interferometry, and shows its application examples for multiple moving targets. The key points of this algorithm are that multiple targets are resolved through peak extraction from a Doppler frequency spectrogram for each range, and the position corresponding to each peak is estimated using interferometry and a range estimation method with an interpolation technique. This algorithm also estimates the shape of targets by compensating for the motion of the estimated scattering centers. For simplicity, we first consider a 2-dimensional problem, and the imaging of a few targets on a rotating platform. For the purpose of high-resolution imaging, we use the smoothed pseudo Wigner distribution (SPWD, described in Section 1.3.2) for time-frequency analysis. Performance evaluations with numerical simulations and experiments verify that the proposed algorithm achieves high-resolution shape estimation for multiple revolving targets. Next, we compare the performance of SPWD and the sliding-window discrete Fourier transform (SDFT, described in Section 1.3.2) in the application to revolving targets, and discuss the suitable condition for each algorithm. Based on this analysis, we then apply the UWB Doppler radar interferometry to human imaging using a numerical walking human model composed of multiple point scatterers, and examine the imaging performance and its problem.

2.2 Imaging System and Algorithm

2.2.1 System Configuration

Figure 2.1 depicts a schematic of the imaging setup for UWB Doppler radar interferometry. A transmitting antenna Tx and three receiving antennas Rx_1, Rx_2, and Rx_3 are arrayed in the xz plane, at positions $(x, z) = (d/2, d/2+z_\text{c})$, $(-d/2, -d/2+z_\text{c})$, $(d/2, -d/2+z_\text{c})$, and $(-d/2, d/2+z_\text{c})$ respectively. The bottom pair Rx_1 and Rx_2 constitutes a horizontal interferometer and the pair Rx_1 and Rx_3 constitutes a vertical interferometer.

The transmitting/receiving signals and the data collection process are described below. Fig. 2.2 illustrates the time sequence of the received data from a UWB Doppler radar. The Doppler radar repeats pulse transmissions with an interval of T_s called the inter-pulse period (IPP). As shown in Fig. 2.2, we define two time variables: t corresponding to the time of pulse transmission, and τ corresponding to the time of echo reception associated with range R:

$$R = \frac{c\tau}{2}, \tag{2.1}$$

where c is the speed of light. A transmitting signal $s_\text{T}(\tau)$ is a UWB signal with central frequency f_0 in the form:

$$s_\text{T}(\tau) = T(\tau)e^{j2\pi f_0 \tau}, \tag{2.2}$$

where $T(\tau)$ is the transmitting waveform. In this chapter, $T(\tau)$ is expressed as:

$$T(\tau) = \begin{cases} \frac{A}{2}\left[1 + \cos\left(\frac{\pi\tau}{T_\text{p}}\right)\right] & \left(|\tau| < \frac{T_\text{p}}{2}\right) \\ 0 & \text{(Otherwise)} \end{cases}, \tag{2.3}$$

where A is the transmitting amplitude and T_p is the pulsewidth determined by the bandwidth W. T_p dictates a nominal downrange resolution ΔR. The relationship between these is:

$$\Delta R = \frac{cT_\text{p}}{2} = \frac{c}{2W}. \tag{2.4}$$

If the n-th target is moving with radial velocity $v_{\text{d}n}$, the frequency of the received signal is shifted by the Doppler frequency $f_{\text{d}n} = 2v_{\text{d}n}/\lambda$. The received signal at Rx_i is expressed as:

$$s_i(\tau) = e^{-j2\pi f_0 \tau} \sum_n \alpha_{\text{R}n} s_\text{T}(\tau - \tau_{\text{p}n}) e^{j2\pi f_{\text{d}n}(\tau - \tau_{\text{p}n})}, \tag{2.5}$$

where $\tau_{\text{p}n}$ is the time delay related to the range between the Rx_i and the n-th target, and $\alpha_{\text{R}n} = A_{\text{R}n}/A < 1$ is the ratio of the receiving amplitude $A_{\text{R}n}$ to the transmitting amplitude A. We acquire the received signal $s_{ik}(t)$ in range bin k using each Rx_i by a discretization of $s_i(\tau)$ in terms of the time delay for all t. The time delay after the discretization corresponding to range bin k is expressed as $\tau_{\text{p}k} = 2k\Delta R/c$. The Doppler frequency spectrogram is calculated by the time-frequency analysis of $s_{ik}(t)$ for all i and k.
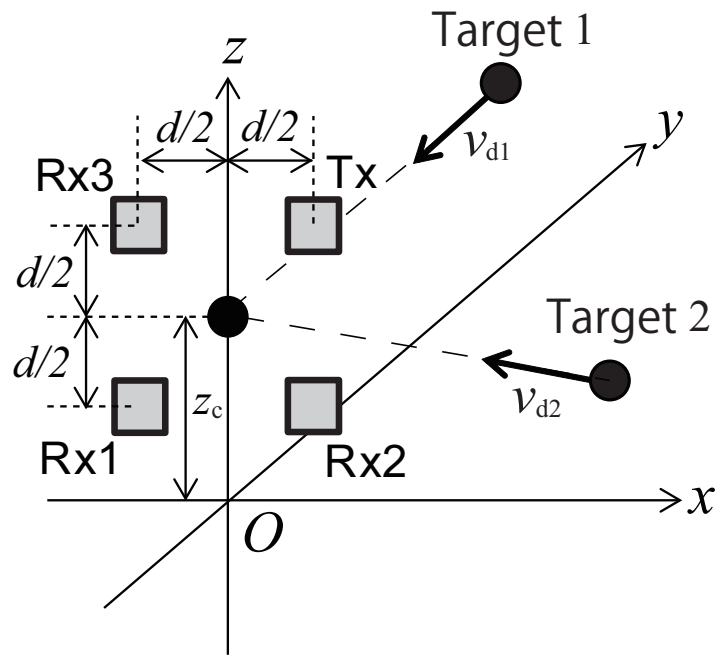
Figure 2.1: System configuration for UWB Doppler radar interferometry.
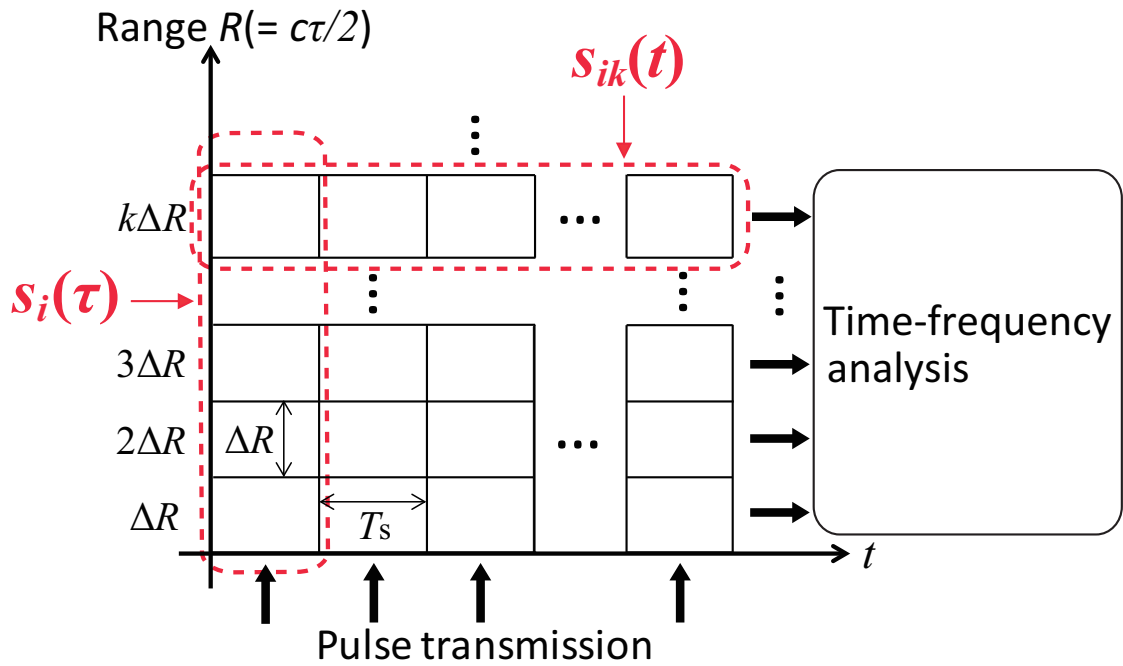
Figure 2.2: Time sequence of UWB Doppler radar pulse transmission and echo reception.

2.2.2 Target Separation with Time-Frequency Analysis

We estimate the time variation of the target's radial velocity with the time-frequency analysis, and separate multiple scattering centers using the obtained spectrograms. In this study, the time-frequency distribution $S_{ik}(t, v_d)$ is obtained by either the SDFT or the SPWD. A performance comparison of these methods shall be provided in Sec. 2.3.3. The SDFTs of signals $s_{ik}(t)$ are calculated with Eq. (1.8) as:

$$S_{ik}(t, v_d) = \int_{-\infty}^{\infty} s_{ik}(\nu) w_H(\nu - t) e^{-j4\pi\nu v_d/\lambda} d\nu, \tag{2.6}$$

where $w_H(t)$ is the Hamming window function,

$$w_H(t) = \begin{cases} 0.54 - 0.46 \cos \dfrac{2\pi}{T_w} t & (0 \le t \le T_w) \\ 0 & \text{(otherwise)}, \end{cases} \tag{2.7}$$

In contrast, using Eq. (1.11), the SPWDs of the $s_{ik}(t)$ are determined from

$$S_{ik}(t, v_d) = \int_{-\infty}^{\infty} \int_{-\infty}^{\infty} e^{-((t-t')^2/\sigma_t^2)} e^{-((v_d-v_d')^2/\sigma_v^2)}$$
$$\cdot \left\{ \int_{-\infty}^{\infty} s_{ik}(t + \nu/2) s_{ik}^*(t - \nu/2) e^{-j4\pi\nu v_d/\lambda} d\nu \right\} dt' dv_d'. \tag{2.8}$$

We next extract from the time-frequency distribution the peaks corresponding to the scattering centers. Significant peaks of $S_{ik}(t, v_d)$ are extracted using the following conditions:

$$\frac{d|S_{ik}(t, v_d)|}{dv_d} = 0, \tag{2.9}$$

$$|S_{ik}(t, v_d)|^2 > \rho \max_{t, v_d} |S_{ik}(t, v_d)|^2, \tag{2.10}$$

where $0 < \rho \le 1$ is the ratio of the peak extraction threshold power to the maximum power, and is empirically determined.

2.2.3 Range Estimation with Interpolation Technique with Calibration Function

Imaging is conducted through position estimations of scattering centers corresponding to each extracted peak. The position is determined by the range and direction-of-arrival (DOA). This subsection describes a method for range extraction using an interpolation technique from the calibration curve. The range $R_1(t, v_{dn})$ is estimated by finding the range that maximizes the echo intensity:

$$R_1(t, v_{dn}) = \Delta R \arg \max_k |S_{1k}(t, v_{dn})|. \tag{2.11}$$

To realize high-resolution imaging, however, we must estimate the range to an accuracy that is better than the nominal downrange resolution because our system assumes that ΔR is of order 10 cm. This resolution is insufficient in estimating human shapes. For this purpose, the proposed algorithm uses an interpolation between the range gates based on the echo power ratio around the peak. Fig. 2.3 shows an example of the received signal and true range $R(t, v_{\mathrm{d}n})$. We estimate $R(t, v_{\mathrm{d}n})$ using the fractional range $D(\rho_p)$ determined by a calibration experiment. We first performed calibration experiments, in which the echo power ratio was measured at the two adjacent range gates around the peak when the fractional range D $(0 \leq D < \Delta R)$ of a point target was varied. During calibration, we measured the maximum power P_1 of the received signal, and the power P_2, which is the larger value of the adjacent powers of the maximum power point. Then, the echo power ratio $\rho_{\mathrm{p}}(D)$ is defined as:

$$\rho_{\mathrm{p}}(D) = P_1/P_2. \tag{2.12}$$

We use a calibration function $D(\rho_{\mathrm{p}})$, which is the inverse function of $\rho_{\mathrm{p}}(D)$ to determine the accurate position $R(t, v_{\mathrm{d}n})$ of the target, which is estimated by summing $R_1(t, v_{\mathrm{d}n})$ and the fractional range $D(\rho_{\mathrm{p}})$ (see Fig. 2.3):

$$R(t, v_{\mathrm{d}n}) = R_1(t, v_{\mathrm{d}n}) + D(\rho_{\mathrm{p}}). \tag{2.13}$$

2.2.4   Scattering Center Positioning by Interferometry

The elevation DOA $\theta_{\mathrm{EL}n}$ and azimuth DOA $\theta_{\mathrm{AZ}n}$ of n-th target are calculated from interferometry:

$$\theta_{\mathrm{EL}n}(t) = \sin^{-1}\left[\frac{\angle S_{1k'}(t, v_{\mathrm{d}n}) - \angle S_{3k'}(t, v_{\mathrm{d}n})}{(2\pi d/\lambda)}\right], \tag{2.14}$$

$$\theta_{\mathrm{AZ}n}(t) = \sin^{-1}\left[\frac{\angle S_{1k'}(t, v_{\mathrm{d}n}) - \angle S_{2k'}(t, v_{\mathrm{d}n})}{(2\pi d \cos \theta_{\mathrm{EL}n}(t)/\lambda)}\right], \tag{2.15}$$

where k' is the range bin where n-th target is detected. Having acquired $R(t, v_{\mathrm{d}n})$, $\theta_{\mathrm{AZ}}(t, v_{\mathrm{d}n})$ and $\theta_{\mathrm{EL}}(t, v_{\mathrm{d}n})$, the positions of the scattering centers $\mathbf{x}_{\mathrm{s}}(t, v_{\mathrm{d}n})$ can be determined:

$$
\mathbf{x}_{\mathrm{s}}(t, v_{\mathrm{d}n}) =
\begin{bmatrix} x_{\mathrm{s}}(t, v_{\mathrm{d}n}) \\ y_{\mathrm{s}}(t, v_{\mathrm{d}n}) \\ z_{\mathrm{s}}(t, v_{\mathrm{d}n}) \end{bmatrix} =
\begin{bmatrix} R(t, v_{\mathrm{d}n}) \cos \theta_{\mathrm{EL}}(t, v_{\mathrm{d}n}) \sin \theta_{\mathrm{AZ}}(t, v_{\mathrm{d}n}) \\ R(t, v_{\mathrm{d}n}) \cos \theta_{\mathrm{EL}}(t, v_{\mathrm{d}n}) \cos \theta_{\mathrm{AZ}}(t, v_{\mathrm{d}n}) \\ R(t, v_{\mathrm{d}n}) \sin \theta_{\mathrm{EL}}(t, v_{\mathrm{d}n}) + z_{\mathrm{c}} \end{bmatrix}. \tag{2.16}
$$

Finally, we compensate for the motion of the target on the acquired orbit of the scattering centers to acquire shape information of targets. The procedure for the proposed imaging algorithm with UWB Doppler radar interferometry is summarized in Fig. 2.4. The proposed algorithm provides not only accurate separation of multiple moving targets, but also high-resolution shape estimation. Moreover, we can estimate three-dimensional images using only three receiving antennas.
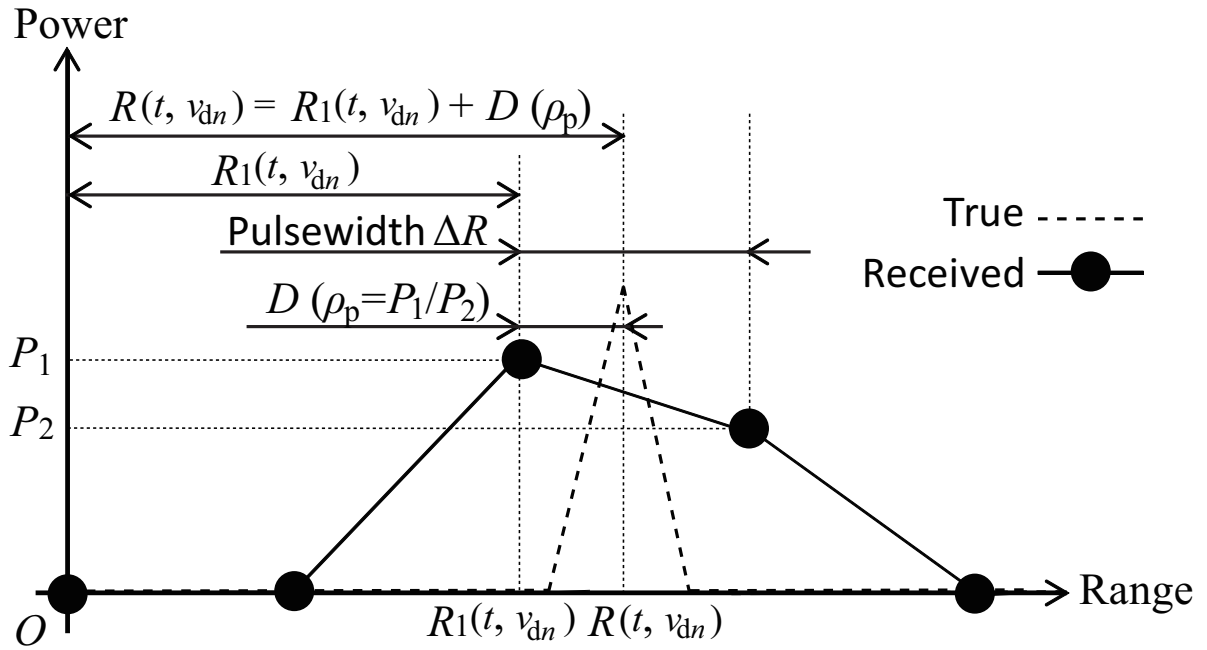
Figure 2.3: Relationship between received signal and true range.
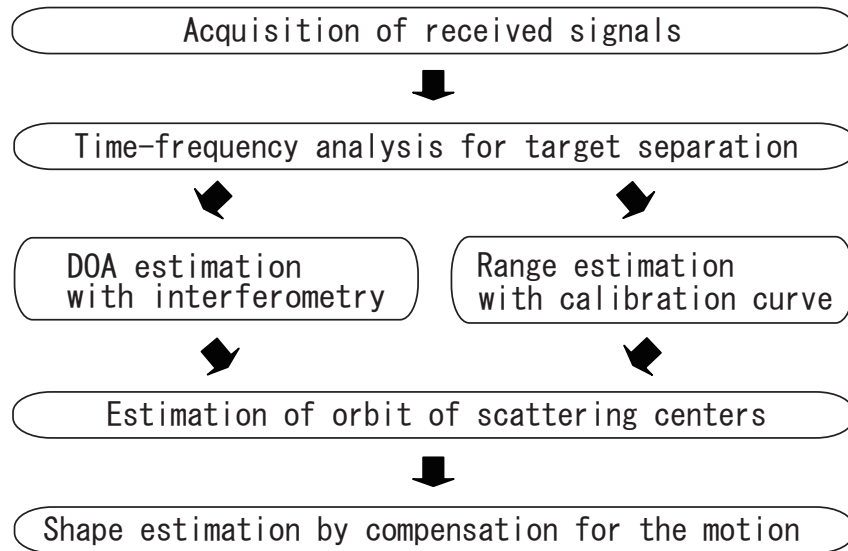
Figure 2.4: Procedure within the proposed imaging algorithm using UWB Doppler radar interferometry.
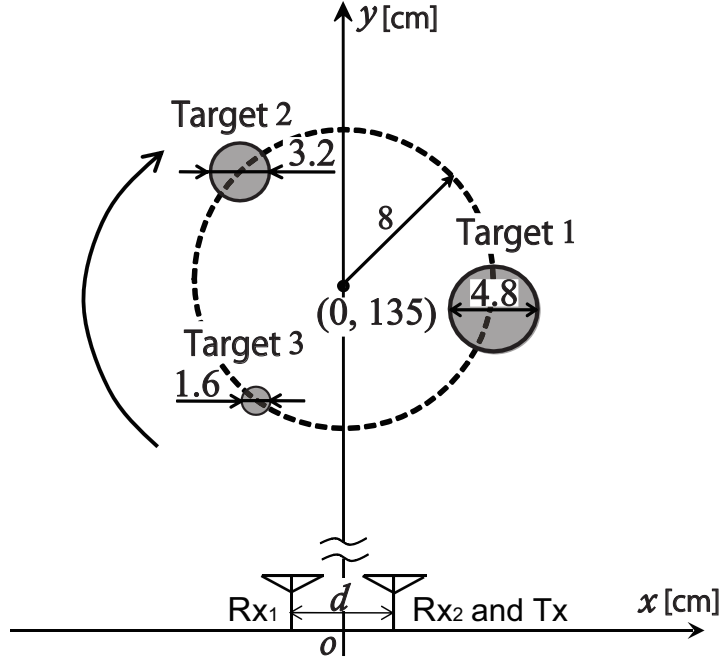
Figure 2.5: Three revolving targets assumed in the simulation.

2.3 Application to Multiple Revolving Targets

2.3.1 Performance Evaluation with Numerical Simulation

This subsection presents examples of target separation and shape estimation with the proposed algorithm using both numerical simulation and experiment. To begin, an idealized two-dimensional imaging example is considered in a numerical simulation without noise, shadowing, and other obstacles. We use a UWB pulse with carrier frequency $f_0 = 26.4$ GHz and a bandwidth $W = 500$ MHz, corresponding to a range resolution ΔR of 30 cm. The antennas are omni-directional, and their separation d is 5 cm. The setup (see Fig. 2.5) involves three revolving circular targets of different sizes, one mono-static antenna, and one receiving antenna. The IPP T_s and the observation time are 1.29 ms and 1.32 s. The received signals are calculated using ray-tracing. The calibration function $D(\rho_p)$ is numerically calculated. We use the SPWD in this and following subsections to achieve high-resolution imaging, and we set $\rho = 0.2$, $\sigma_t = 3T_s$, and $\sigma_v = 4\Delta v_d$, where Δv_d is the resolution of the radial velocity. The angular velocity of the targets is 1.5π rad/s and the center of rotation is $(x, y) = (0, 1.35$ m$)$. This simulation assumes that motion of targets (revolving) and their parameters (the angular velocity and the center of rotation) are known and the shape and number of targets are unknown. We estimate target shape by compensating for the estimated points using the angular velocity and the center of ratation.

43
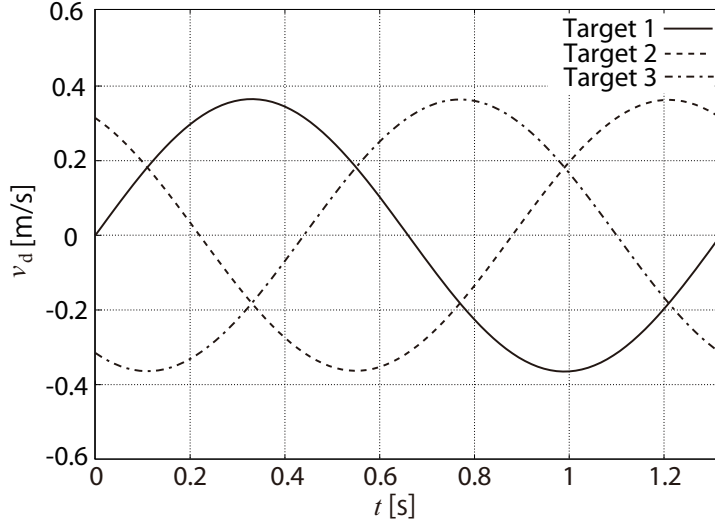
Figure 2.6: True radial velocity of the three revolving targets.

The true radial velocities of the targets and the SPWD spectrograms are shown in Figs. 2.6 and 2.7. The targets are in the range bins 4 (1.2 m) to 5 (1.5 m) in this setup, thus we have given spectrograms $S_{14}(t, v_d)$ and $S_{15}(t, v_d)$. The SPWD have obviously detected the time-varying radial velocities of all three targets accurately. Fig. 2.8 shows a range estimation result for each extracted v_d. As shown in this figure, the ranges of all separated targets are estimated, and a correspondence between these ranges and radial velocities v_d is correctly confirmed. Fig. 2.9 presents a construction of the orbits of the scattering centers estimated with the acquired SPWD; accurate locations of scattering centers are obtained. Fig. 2.10 shows the estimated image compensating for the revolving motion. A satisfactory high-resolution estimation of the shape of all three targets is obtained. The root mean square (RMS) error of the estimated image is 0.35 mm. These results indicate that the proposed algorithm realizes accurate separation of multiple moving targets, and achieves high-resolution imaging for all targets.

2.3.2 Performance Evaluation with Experiment

In the numerical simulation, accurate images were obtained under several simple assumptions. This subsection investigates the performance of the proposed algorithm when using experimental data. Fig. 2.11 shows the experimental arrangement. We use two circular stainless steel targets of diameter 6.6 cm placed on a rotating platform. The platform's center of rotation is located $(x, y) = (0, 1.3 \text{ m})$, and its angular velocity is 1.5π rad/s. The distance between the center of rotation and the center of the targets is 8 cm. We use a single transmitter and two receivers; each is horn antenna with -3dB beamwidth of $\pm 11°$. The transmitted pulse and the arrangement of the receiving antennas are the same
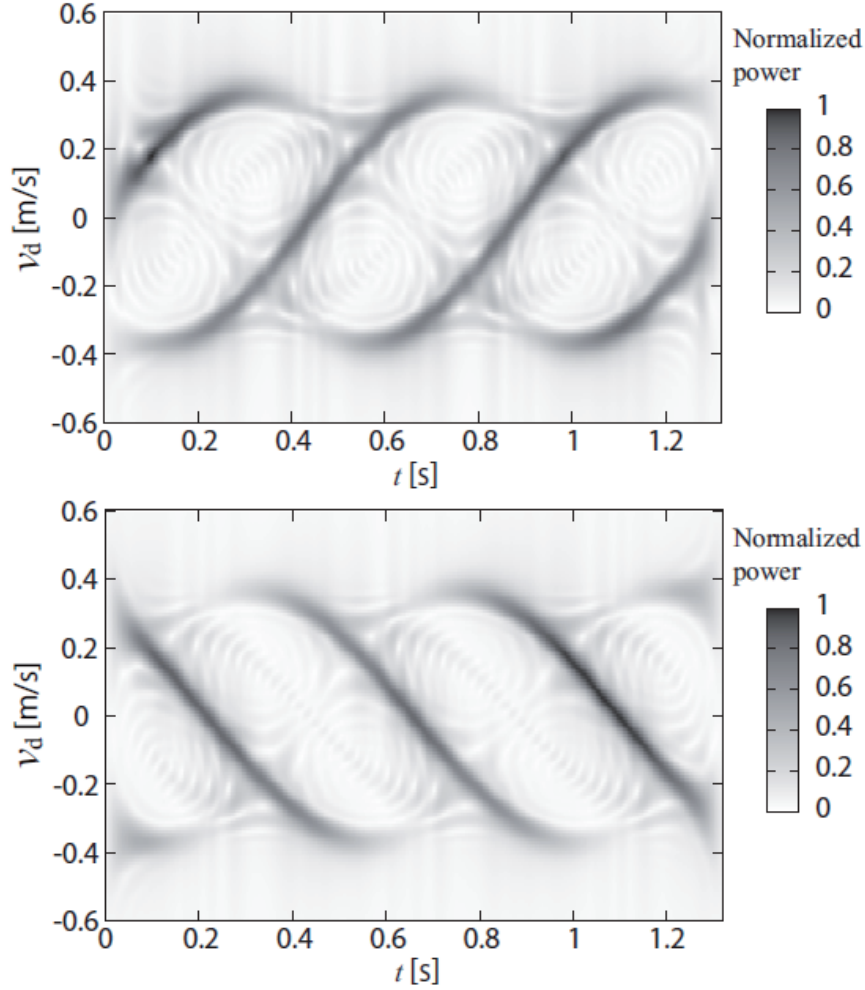
Figure 2.7: SPWD spectrograms of Rx_1 in range bins 4 (below) and 5(above) in the simulation involving three revolving circular targets.

as described in the previous section. Same as the previous section, the angular velocity and the center of the rotating platform are known, and shape and number of targets are unknown. The corresponding spectrograms $S_{14}(t, v_d)$ and $S_{15}(t, v_d)$, (see Fig. 2.12) demonstrate that the SPWD accurately separates the two targets in a real environment setting.

First, we determine a calibration function $D(\rho_p)$ for the range interpolation with a simple experiment. Fig. 2.13 outlines the calibration experiment. A target is a sufficient large copper plane. We scan the target in $0 \leq D < \Delta R$, and the peak ratio $\rho_p(D)$ is measured at each target position. In this experiment, we scan the copper plane in 30 cm $\leq R_{cp} < 60$ cm with steps of 1 cm, where R_{cp} is a distance between the antenna and the target. This scanning range corresponds to the fractional range of $0 \leq D < 30$ cm because
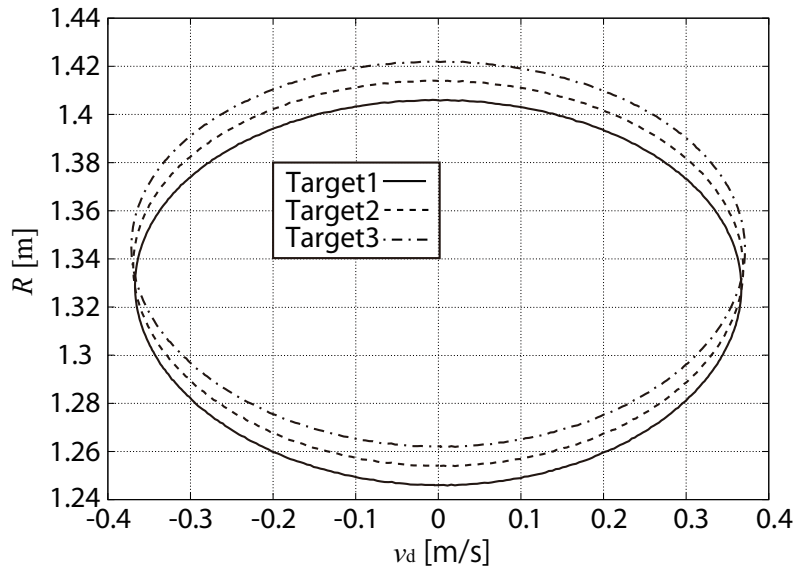
Figure 2.8: Relationship between extracted radial velocities and estimated ranges of the separated targets.
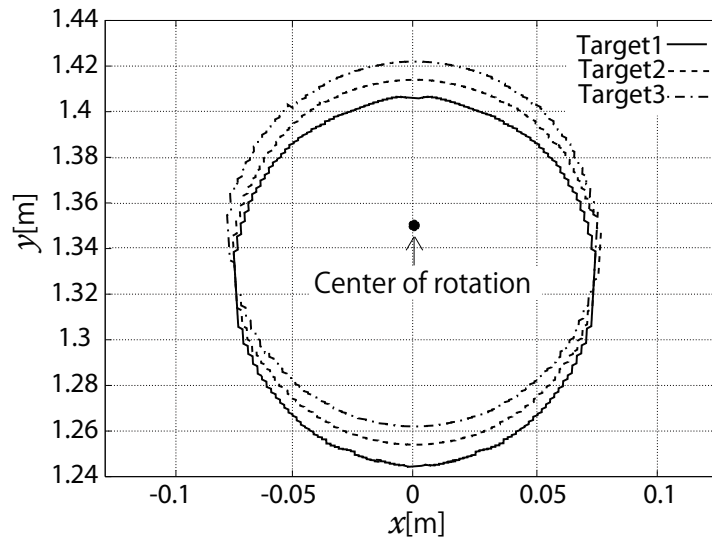
Figure 2.9: Estimated orbits of the scattering centers for each target in the simulation.

ΔR is 30 cm. Fig. 2.14 shows the observed points and the determined $D(\rho_\mathrm{p})$ by a fitting of these data points using seven order polynomial function. Then, distance for each peaks of Fig. 2.12 are estimated by this function and Eq. (2.13). Fig. 2.15 shows a relationship between the radial velocity and estimated range. Here, we use in the estimation process only the points for which signal to noise ratio is relatively high. This is because there
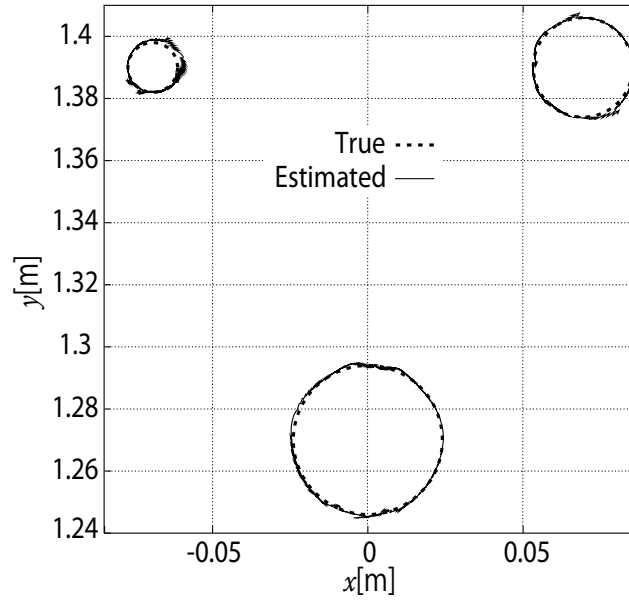
Figure 2.10: Estimated images of the three revolving targets in the simulation.
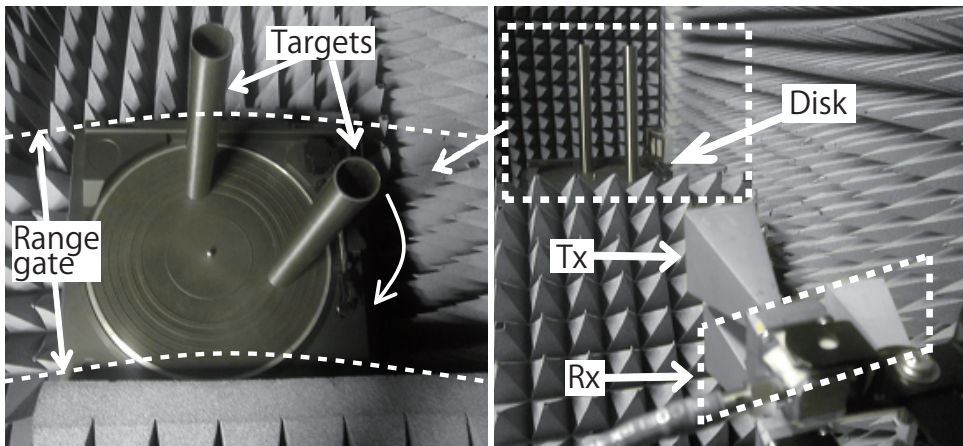
Figure 2.11: Photos of the experimental setup showing two targets on a revolving disk and the antenna array.

are distortions in the orbit due to shadowing and interference from the other targets. Although distortions due to noise and interference are remained, ranges of both targets corresponding to each radial velocity are estimated.

Fig. 2.16 shows the estimated orbit of the scattering centers. The estimated images (Fig. 2.17) demonstrates that the proposed algorithm can provide high-resolution image estimates for both targets. The RMS error of the estimated image is 5.2 mm corresponding to 1/58 of the nominal resolution determined by the bandwidth. This result means that
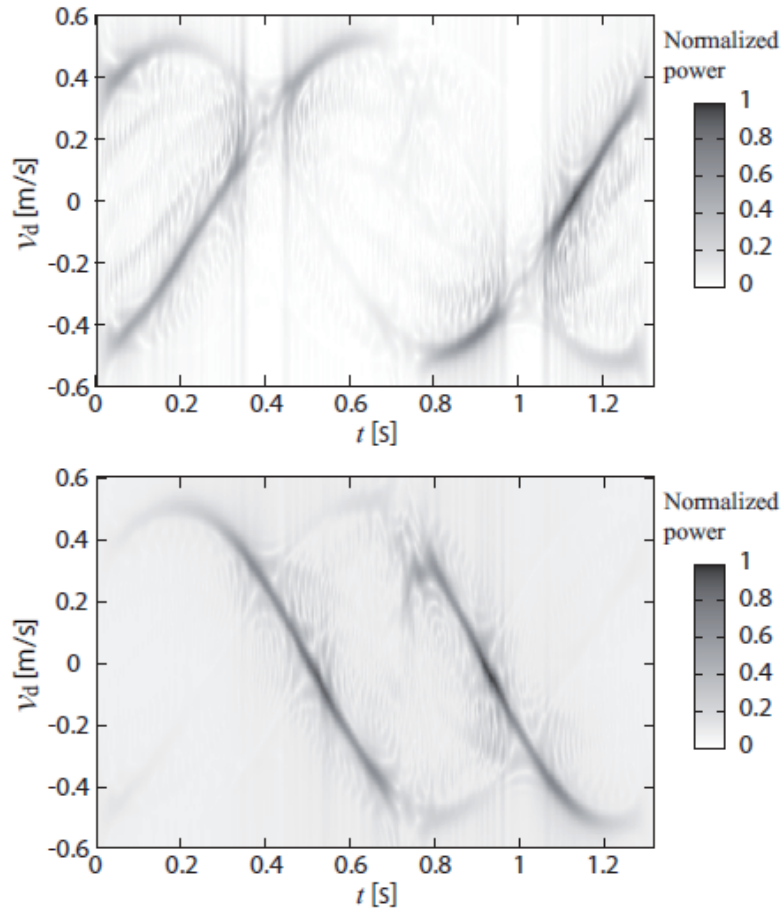
Figure 2.12: SPWD spectrogram of Rx$_1$ in range bins 4 (below) and 5 (above) from experimental data.

high-resolution images of both targets are accurately estimated.

2.3.3 Performance Comparison of SPWD and SDFT

The high-resolution imaging of multiple revolving targets using SPWD was verified with the numerical and experimental data. However, the SPWD have two critical drawbacks. The first is a performance deterioration resulting from cross-terms involving multiple target signals from multiple frequencies. Fig. 2.18 shows the SPWD spectrogram obtained from experimental data for the three revolving targets. We used three circular stainless steel targets, two of diameter 3.2 cm and one of diameter 2.6 cm. The platform's center of rotation is located at (0, 1.15 m), and its angular velocity is 1.1π rad/s; the distance to each target center is 8 cm. As evident in Fig. 2.18, cross-term effects remain, and these lead to errors in separation and the occurrence of false images. In this case, we confirm
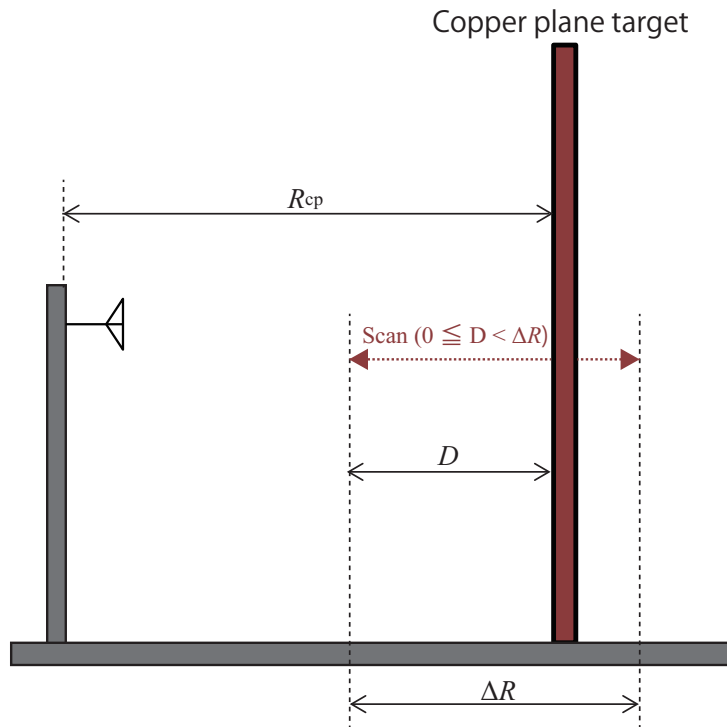
Figure 2.13: Outline of calibration experiment.
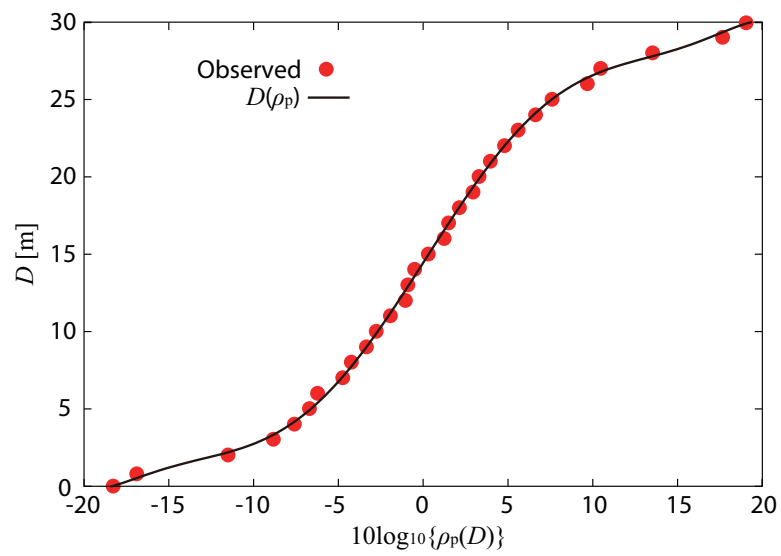
Figure 2.14: Result of calibration experiment and determined $D(\rho_{\rm p})$.

49
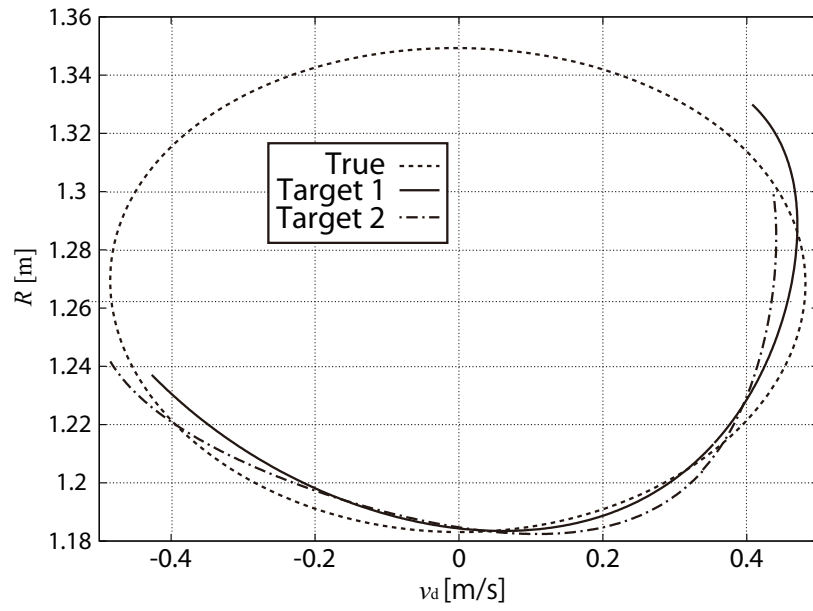
Figure 2.15: Relationship between radial velocity and estimated range from experimental data with determined $D(\rho_{\mathrm{p}})$.
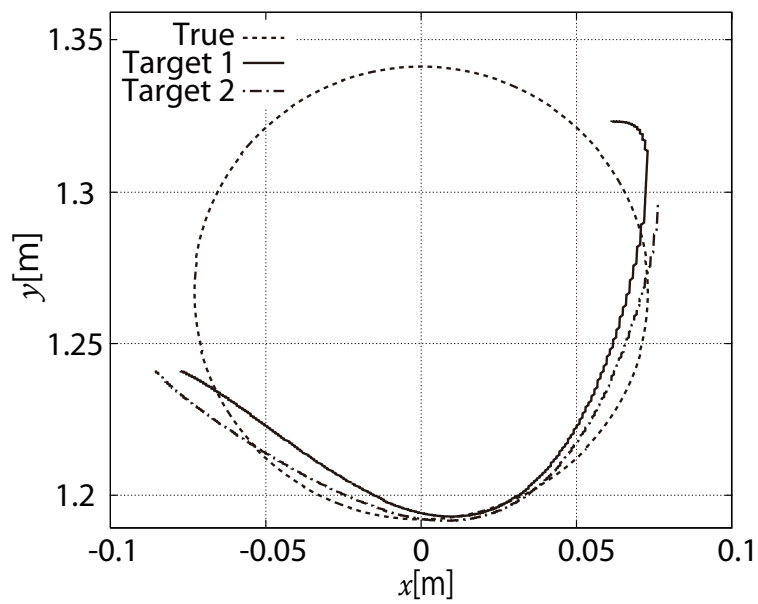
Figure 2.16: Estimated orbits of the scattering centers from experimental data of the two revolving targets.
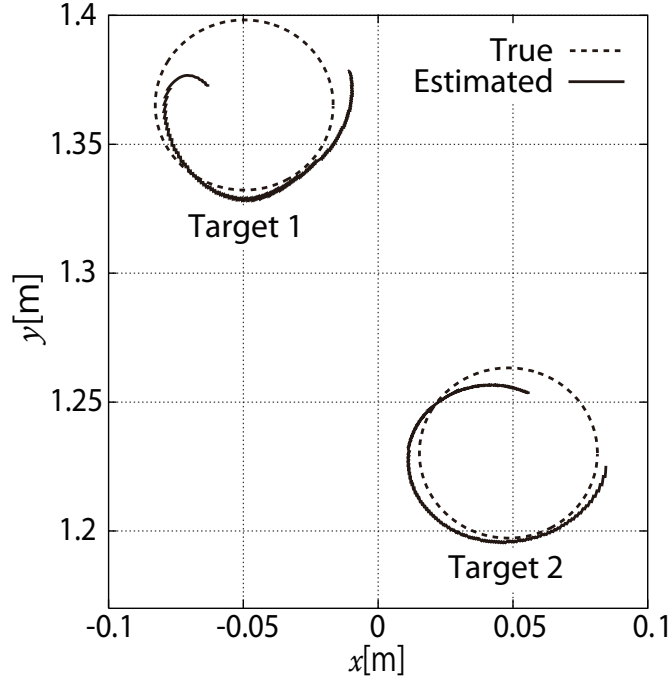
Figure 2.17: Estimated images generated with the proposed algorithm using experimental data of the two revolving targets.

that accurate imaging is not possible because of signal interference from multiple radial velocities and these cross-terms. Moreover, selection of appropriate smoothing parameters is difficult for various practical scenarios. Therefore, SPWD may be applicable under limited situations only.

In contrary, the SDFT does not generate cross-terms [112]. Fig. 2.19 shows the SDFT spectrogram obtained from the same experiment of Fig. 2.18. Although the resolution for time-frequency distribution is low compared with that for the SPWD, cross-terms are not apparent. Fig. 2.20 shows estimated images of these targets. Because the resolution is low and the amount of interference is large compared with the two-target case, the imaging area is narrow when compared with that in Fig. 2.17. However, we can provide reliable multiple target detection even when target separation with SPWD is difficult. In addition, although the RMS error of the estimated image is 1.5 cm, which is larger than that in Fig. 2.17 produced from the SPWD due to low resolution from SDFT, we assess that this accuracy is sufficient for human monitoring. Moreover, from the view point of real-time capability, SDFT is better than SPWD. The calculation times to produce Figs. 2.18 and 2.19 are 71 s and 0.22 s, respectively with intel Core 2 Duo 3.33 GHz processor, stemming from a smoothing process in evaluating double integrals involved in the SPWD calculation.

The properties for each method are summarized in Table 2.1. The problems using

51
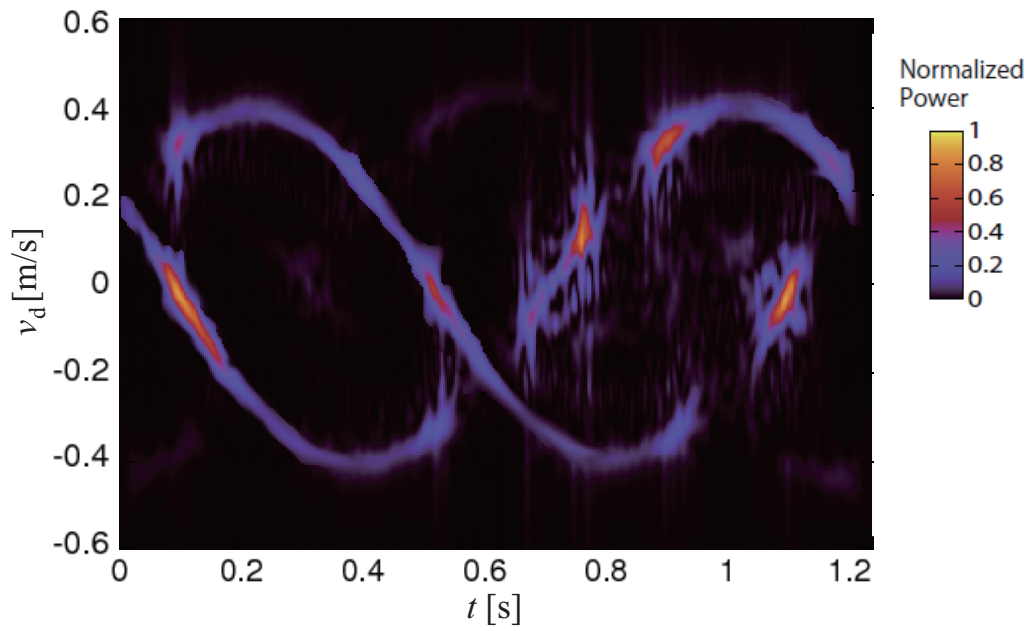
Figure 2.18: Summation of SPWD spectrograms of the three revolving targets using experimental data from range bins 3 (0.9 m) and 4 (1.2 m).
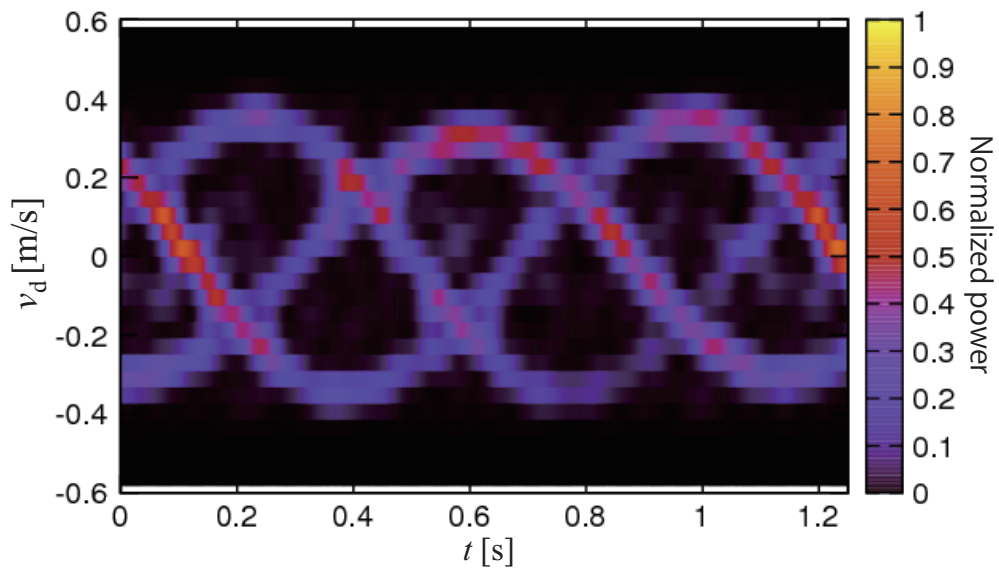
Figure 2.19: Summation of SDFT spectrograms of three revolving targets using experimental data from range bins 3 (0.9 m) and 4 (1.2 m).
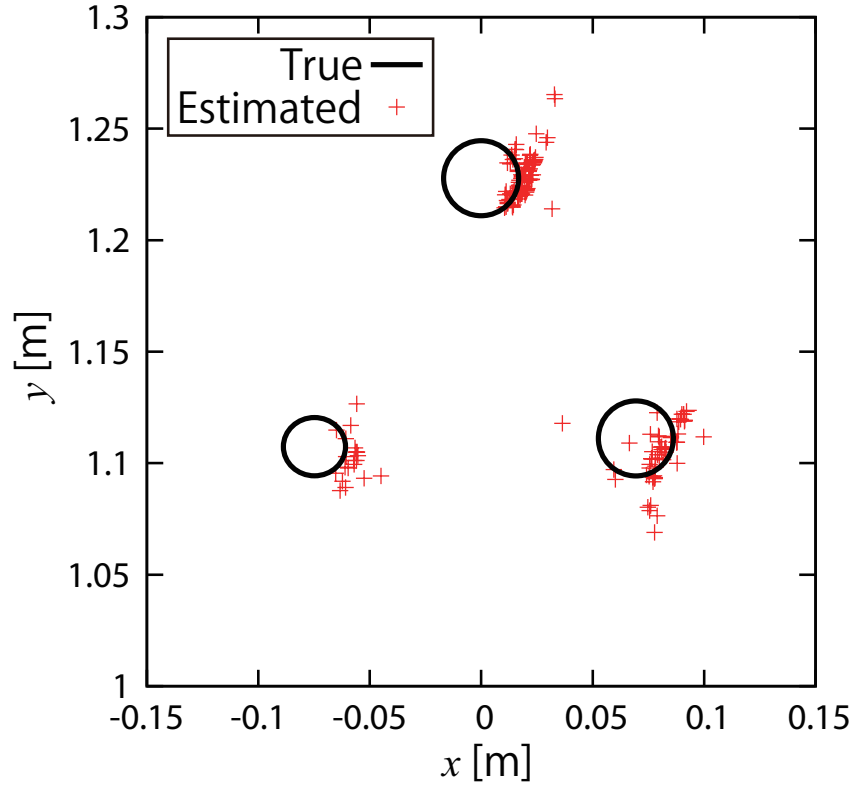
Figure 2.20: Images of three revolving targets from experimental data estimated by the proposed algorithm using SDFT.

Table 2.1: Property comparison for SPWD and SDFT.

	Computation time	Imaging accuracy	Separation capability
SPWD	Large	Very good	Bad
SDFT	Small	Sufficient	Good

the SPWD are the large calculation times and the mis-extraction of peaks due to cross-terms. In contrast, the SDFT technique produces fast calculations without cross-terms. Summarizing these discussions, if the number of scattering centers is sufficiently small and the main purpose is acquiring high-resolution images, SPWD is suitable for this situation. On the other hand, while fast calculation is required and there are many scattering centers, SDFT is more suitable and the more appropriate algorithm to be used for our applications.
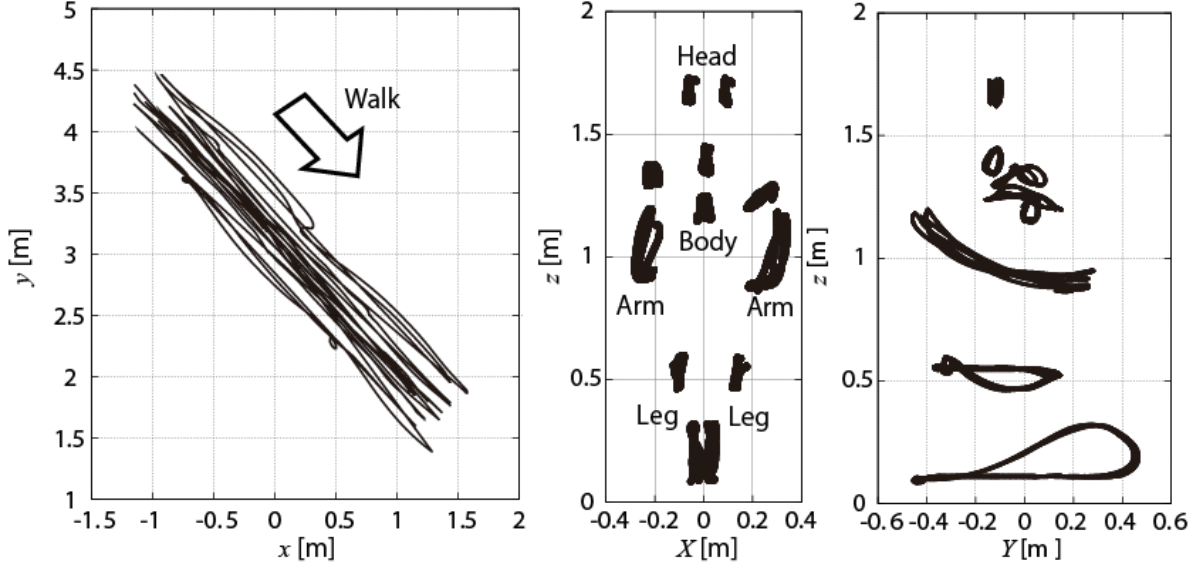
Figure 2.21: True target points and their trajectories for a simulation model of a walking human (Left: Top view   Center: Frontal view, Right: Side view).

2.4   Application to Numerical Human Model

This section investigates the application of the UWB Doppler radar interferometry to human sensing by means of numerical simulation. Multiple point targets representing the scattering centers on various parts of the body are assumed. Our simulation uses twelve points selected from the data points in the "Motion Capture Data Pack" (Eyse JAPAN Corporation), which is comprised of motion capture data of pedestrians, and generates received signals by ray-tracing. The true trajectory of the walker is given in Fig. 2.21; here Y is the forward direction of the walker and X is the positive (right-hand) axis perpendicular to the walking direction. The walking speed and period are 1.59 m/s and 1.16 s, respectively. The antenna separation d is 6 mm and the height of the central antenna position z_c is 30 cm. The center frequency and bandwidth are same as the previous section, and T_p and the observation time are 1.04 ms and 2.1 s, respectively. Based on discussions in the previous section, we use the SDFT with window width of 66 ms to determine the time-frequency distribution. The peak extraction threshold parameter ρ is 0.2.

We estimated the orbit of the scattering centers and the walking velocity based on these estimated points, and extracted a shape of pedestrian outline with motion compensation using the estimated walking velocity. Fig. 2.22 shows the summation of spectrograms from Rx_1 for the range bins. We can see the various peaks corresponding to the motions of the arms and legs. Fig. 2.23 shows the overhead view of the estimated scattering centers. The orbit of the walking target is confirmed to some extent. We next extract the walking
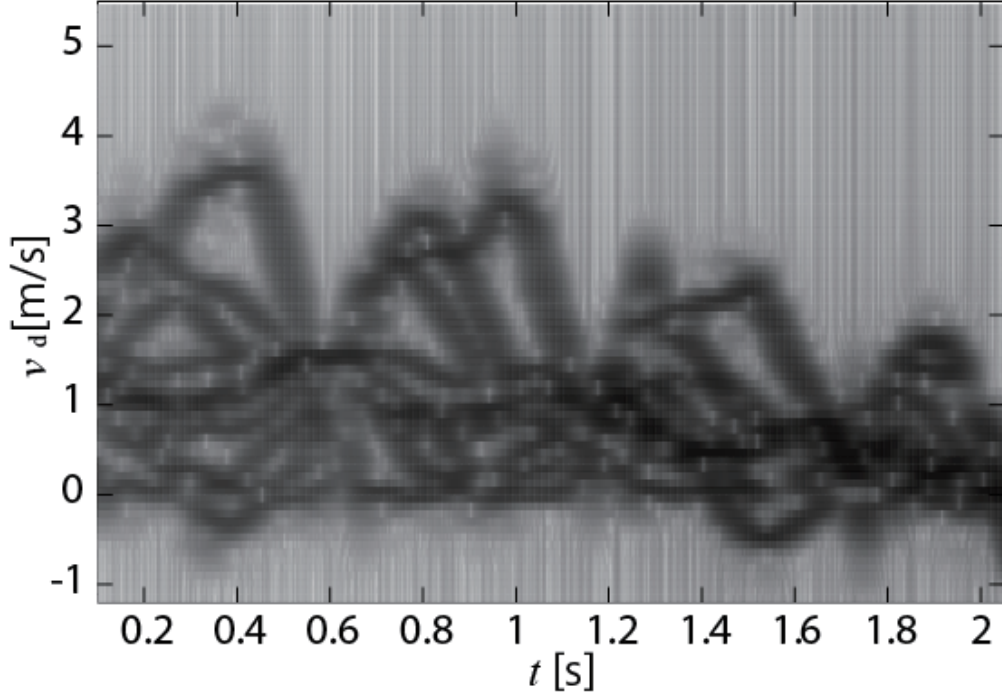
Figure 2.22: Summation of SDFT spectrograms of the numerical human model at Rx_1 for the range bins.

velocity. An orbit of the torso is estimated as a power-weighted mean of scattering center positions:

$$x_o(t) = \frac{\int x_s(t, v_{dn})p(t, v_{dn})dv_{dn}}{\int p(t, v_{dn})dv_{dn}}, \tag{2.17}$$

$$y_o(t) = \frac{\int y_s(t, v_{dn})p(t, v_{dn})dv_{dn}}{\int p(t, v_{dn})dv_{dn}}, \tag{2.18}$$

where $p(t, v_d)$ is a sum of the received power for range bins at (t, v_d) for Rx_1. The walking orbit is then estimated as a low-pass filtering of $x_o(t)$ and $y_o(t)$. Fig. 2.24 shows the true and estimated walking orbits. An accurate estimation of the walking orbit is achieved using the images. The RMS error of the estimated orbit is 5.46 cm. The walking velocity is estimated from the time-derivative of the walking orbit:

$$\mathbf{v}_w(t) = \left(\frac{dx_o(t)}{dt}, \frac{dy_o(t)}{dt} \right). \tag{2.19}$$

Fig. 2.25 shows the imaging result obtained after motion compensation using the estimated $\mathbf{v}_w(t)$. We can establish an outline of a human shape in the frontal view and the leg and arm trajectories in the side view. However, many false images are confirmed, especially among the targets.

55
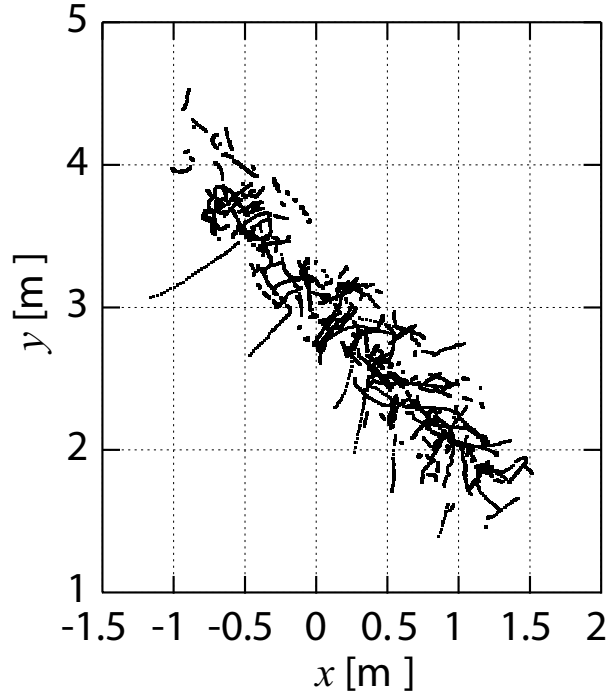
Figure 2.23: Overhead view of the estimated scattering centers of a simulated walking human.

2.5   Conclusions

This chapter proposed a high-resolution imaging algorithm for multiple moving targets using UWB Doppler radar interferometry. Assuming revolving circular targets, we confirmed by simulations and experiments that high-resolution image is obtainable with such interferometry and the SPWD. The mean error of the estimated image is 5.2 mm, which corresponds to 1/58 of the nominal resolution determined by the bandwidth. Next, a performance comparison between SPWD and SDFT showed that the advantages of SDFT are fast calculations and reliable target separations whereas the advantage of SPWD is its high-resolution capability. Based on this comparison, we judged that SDFT is suitable for practical use in human sensing. We also investigated whether this technique is suited for sensing the motion of walking humans. Numerical simulation showed that the scattering center points of the model can be obtained and the walking orbit can be accurately extracted with RMS error of 5.46 cm. Moreover, an outline of a human shape can be extracted by motion compensation using the walking velocity estimated from the walking orbit. However, many false images are confirmed mainly among the targets. These false images lead to mis-extraction of human targets, and this problem represents a serious hurdle in applications monitoring humans. To resolve this problem, we propose in the next chapter an imaging algorithm that is applicable to more realistic situations.
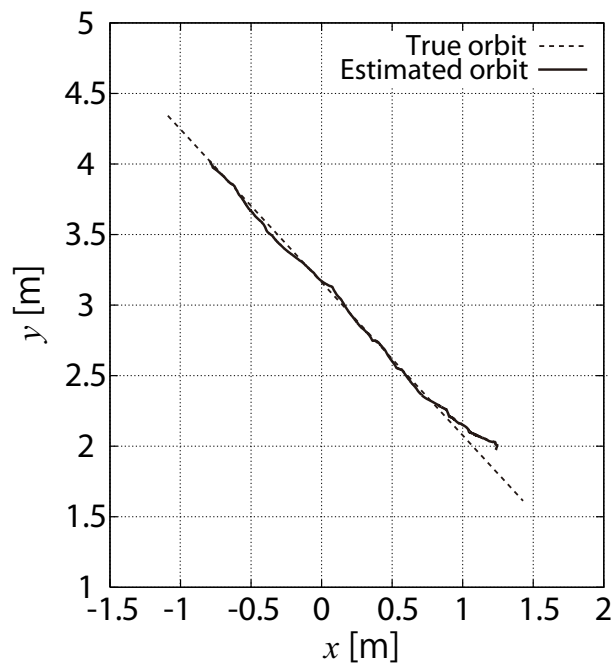
Figure 2.24: Estimation of the orbit for a simulated walking target torso.
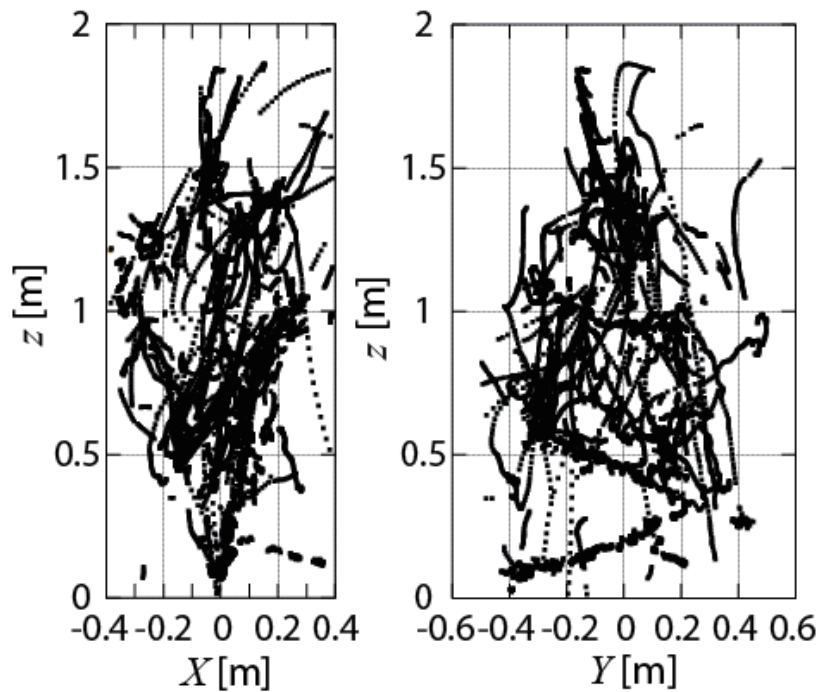
Figure 2.25: Estimated images a simulated walking human after motion compensation using walking velocity (Left: Frontal view   Right: Side view).

Chapter 3

Human Imaging in Realistic Situations

3.1 Introduction

This chapter presents a human imaging based on the imaging algorithm with the UWB Doppler radar by means of experiments assuming realistic situations. The experimental example firstly shows that many false images are estimated owing to interference from body parts similar to the numerical simulation in Section 2.4. To resolve this problem, the mechanism of this type of false images is investigated with simple numerical simulation, and two false image detection and rejection methods that use velocity information are proposed based on the revealed mechanism. The experiment assumes a pedestrian and shows that most of false images are rejected by the proposed methods, and the proposed imaging algorithm achieves accurate and reliable human imaging. Moreover, accurate shape/motion parameters can be extracted from the estimated human image, and real-time imaging with sufficient accuracy is demonstrated. Finally, we confirm that the proposed imaging algorithm is effective to the pedestrians walking in arbitrary directions.

3.2 Human Imaging Experiment

The numerical simulation in the previous chapter indicated that the outline of human shape is extracted and many false images are estimated with the UWB Doppler radar interferometry. In this section, we conduct an experiment to investigate the performance in a realistic situation. The configuration of the experimental system is firstly explained, and a human imaging result and its problem are then presented.
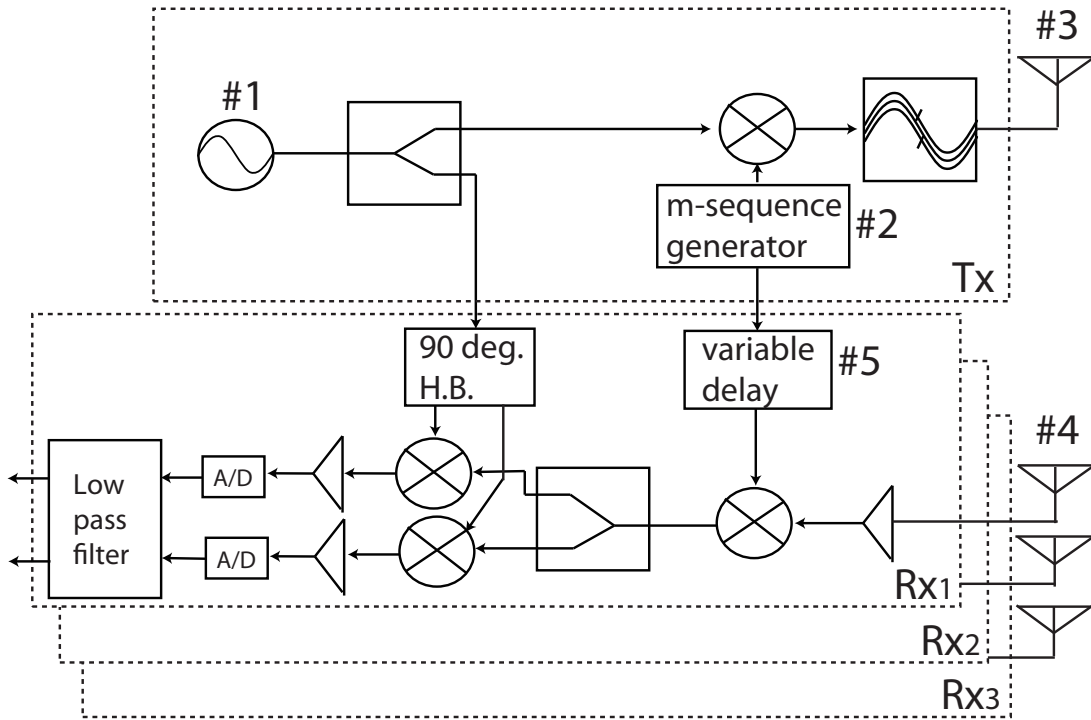
Figure 3.1: Block diagram of the spread spectrum UWB Doppler radar.

3.2.1 Radar System Configuration

The transmitting signals of our experiments are spread spectrum UWB signals in order to acquire sufficient signal-to-noise ratio [184, 185]. Fig. 3.1 shows the block diagram of the spread spectrum UWB Doppler radar. The oscillator #1 generates a CW signal with a frequency of f_0, and the shift register #2 generates a m-sequence of chip width t_C. The CW signal is modulated with the m-sequence, and this modulated signal is transmitted by #3. Then, echoes are obtained by the receiver #4, and the delay circuit #5 generates a time-shifted m-sequence. We take a cross-correlation of the raw received signal obtained in #4 with this time-shifted m-sequence to acquire the signal with high signal-to-noise ratio [185]. These processes gives a range resolution of $\Delta R = ct_C/2$ [184]. Finally, the received signal waveform $s_{ik}(t)$ is acquired with the de-modulation and the low-pass filtering processes. In our all experiments, the radar parameters are f_0=26.4 GHz, t_C= 2 ns and ΔR= 30 cm.

Figs. 3.2 and 3.3 show the system model and the experimental site. The antenna configuration is same as in the previous chapter, and a pedestrian target and measurement at several antenna positions are assumed. In this experiment, we assume a pedestrian target on a treadmill with a belt speed of 3 km/h and the distance between the antennas and the target's torso is fixed to 2.7 m by using the treadmill to clarify the characteristics
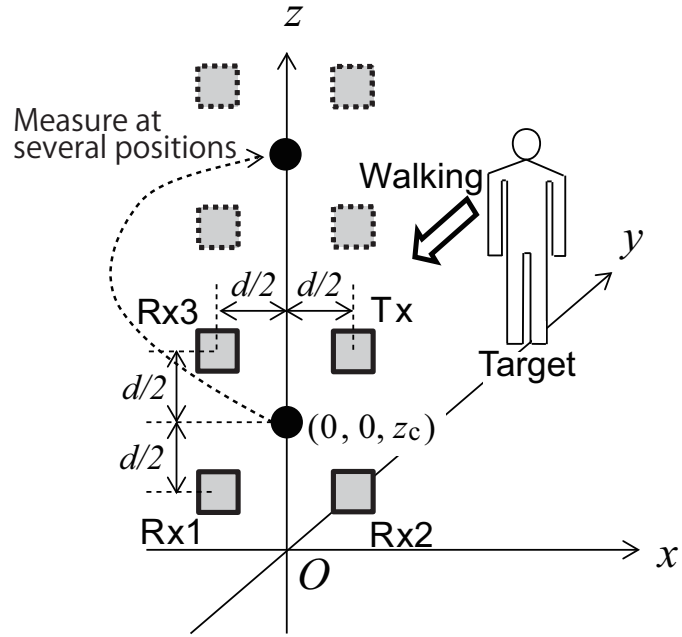
Figure 3.2: System model for a realistic situation.
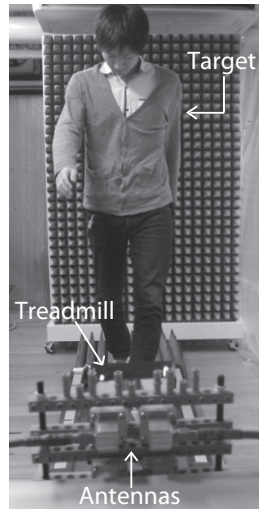
Figure 3.3: Experimental site of the target on the treadmill.

and problems of the UWB Doppler radar interferometry. The heights of the pedestrian and the treadmill are 182 and 14 cm. Horn antennas are used with -3dB beamwidth of $\pm 11°$ in both the E- and H-planes. The antenna separation d is set by consideration of aliasing and accuracy in the DOA estimation process. As shown in Eqs. (2.14) and (2.15), DOA estimation accuracy is improved by setting a large d. However, an unambiguous range
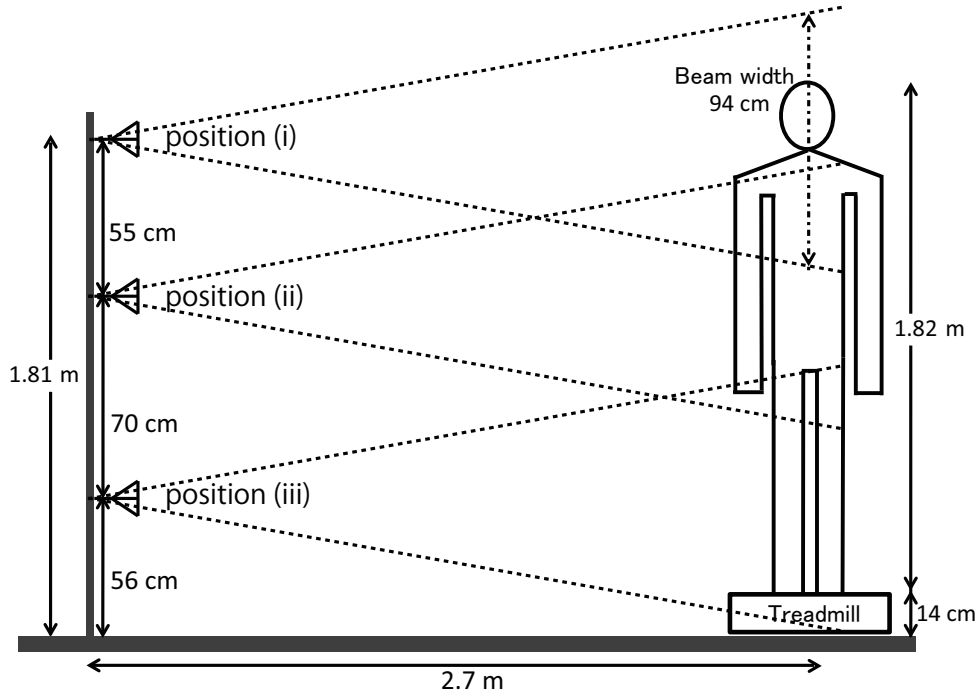
Figure 3.4: Outline of relationship between target and illumination area of transmission beam.

of DOA is determined by d because of the aliasing. From Eq. (2.14), the unambiguous range of the elevation DOA is $\pm \sin^{-1}(\lambda/2d)$. Consequently, we must choose as large d as possible, taking the observation area into consideration. Our experiments set $d = 3.5$ cm, and the unambiguous range of elevation and azimuth DOAs are both $\pm 9.47°$. This range is sufficient for our experimental setting. The inter pulse period is 1.29 ms, and the window size for SDFT is 165 ms. We take measurements at three antenna positions for the acquisition of data that correspond to the whole body : z_c=0.56, 1.26, and 1.81 m. Fig. 3.4 shows the outline of the relationship between the target and the illumination area of the transmission beam at each antenna position. The antennas receive the echoes mainly from the head in position (i), arms and body in position (ii), and legs in position (iii). Image is obtained by the superposition of image estimated at each antenna position.

3.2.2 Result and Problem

Fig. 3.5 shows a spectrogram at the range bin 9 (2.7 m) $|S_{19}(t, v_d)|^2$ for each antenna position. The radial velocity variations of the arms and legs are detected at antenna positions (ii) and (iii), and oscillations of the head and the body are observed at positions (i) and (ii). Fig. 3.6 shows the human image estimated by the UWB Doppler radar interferometry described in the previous Chapter. Here, we use the data of half of a

61
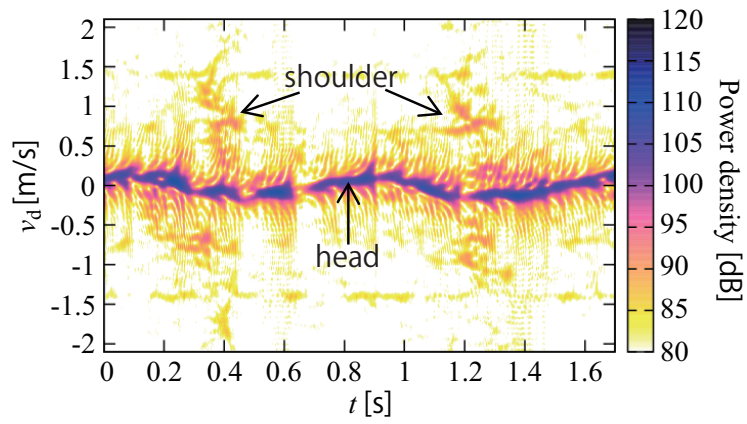
(a) position (i) (Head and shoulder)
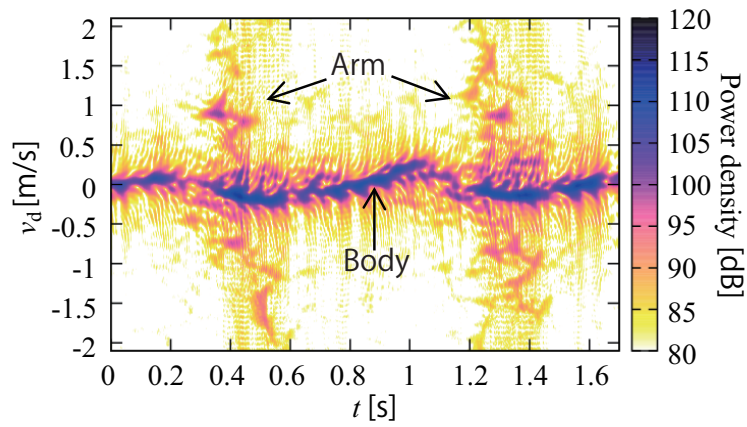
(b) position (ii) (Body and arms)
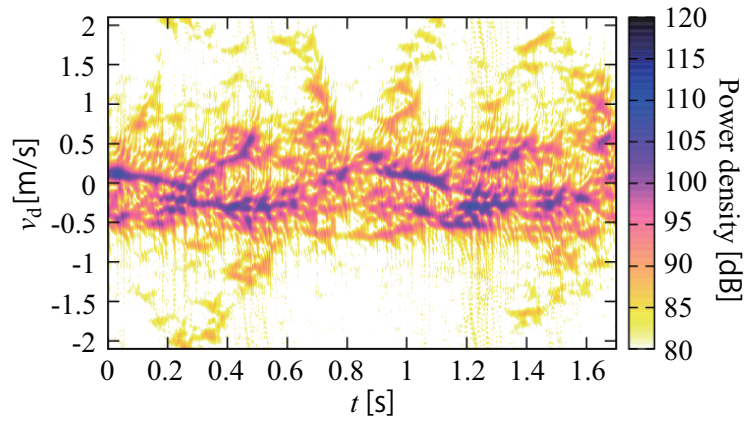
(c) position (iii) (Legs)

Figure 3.5: Spectrogram $|S_{19}(t, v_{\mathrm{d}})|^2$ in each antenna position.
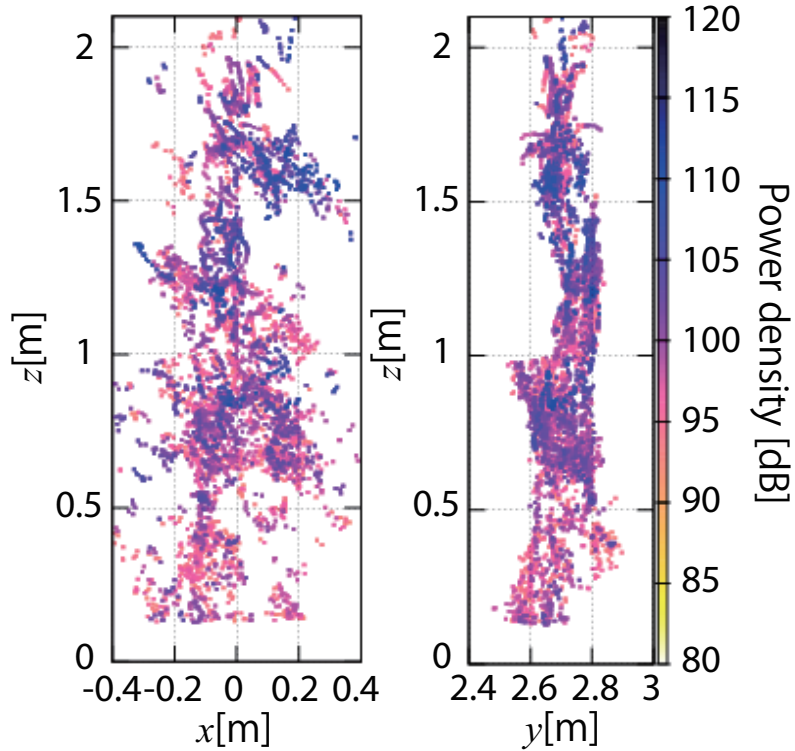
Figure 3.6: Frontal (Left) and side views (Right) of image estimated by UWB Doppler radar interferometry.

walking cycle for imaging, and set $\rho=0.25$ which is peak extraction threshold in Eq. (2.10). This result means that the UWB Doppler radar interferometry obtains a human outline to some extent even using the experimental data. However, since many false images are confirmed, we cannot accurately reconstruct the image of the human body from this result. According to the numerical simulation in Section 2.4 and this experiment, these false images are caused by the interference of the echoes from multiple scattering centers corresponding to various body parts.

3.3 False Image Detection and Rejection Method

3.3.1 Mechanism of False Images

To resolve the problem described in the previous section, we propose a false image detection and rejection method. First, we clarify the mechanism of such false images with a simple numerical simulation. We assume two point targets that have a pendulum motion, and set the antenna separation $d=5$ mm and the center position of the antennas $z_{\mathrm{c}}=0$. With this antenna setting, unambiguous range of DOA becomes $\pm\pi/2$. Fig. 3.7 shows the
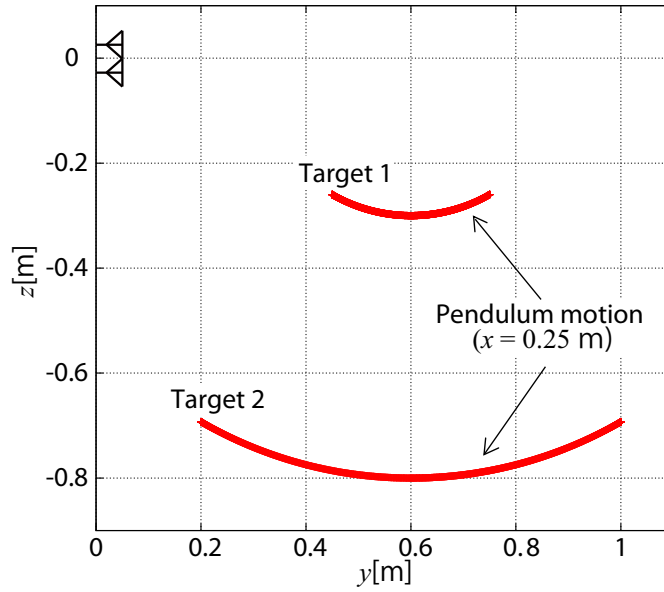
Figure 3.7: Orbit of targets and antenna setting in a simple numerical simulation assuming two point targets that have a pendulum motion.
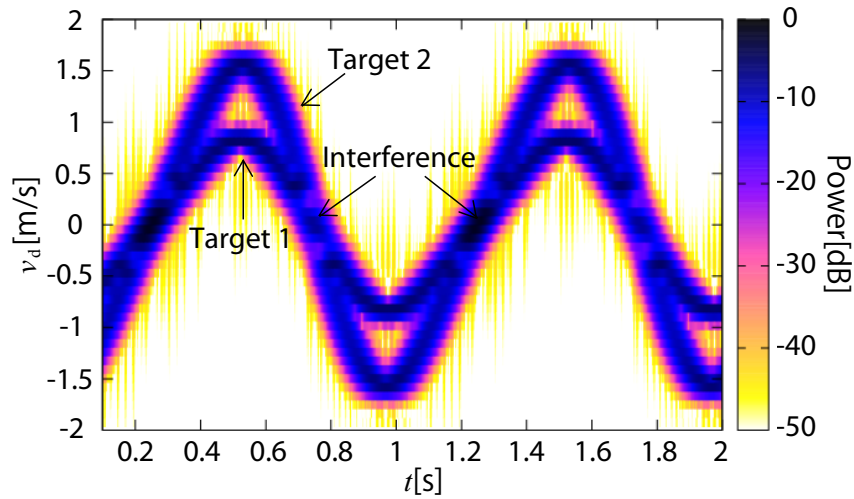
Figure 3.8: Summation of acquired spectrograms for range bins in the simulation of Fig. 3.7.

orbits of the targets. Omni-directional antennas are assumed, and the received signals are calculated with ray-tracing. Other radar settings and parameters are the same as in the previous section. Figs. 3.8 and 3.9 show the spectrogram and the estimated image. The false images are estimated where the target does not exist. Comparing Figs. 3.8 and 3.9 (b), we find that false images are generated when interference of the echoes has

(a) Frontal view   (b) $z(t)$
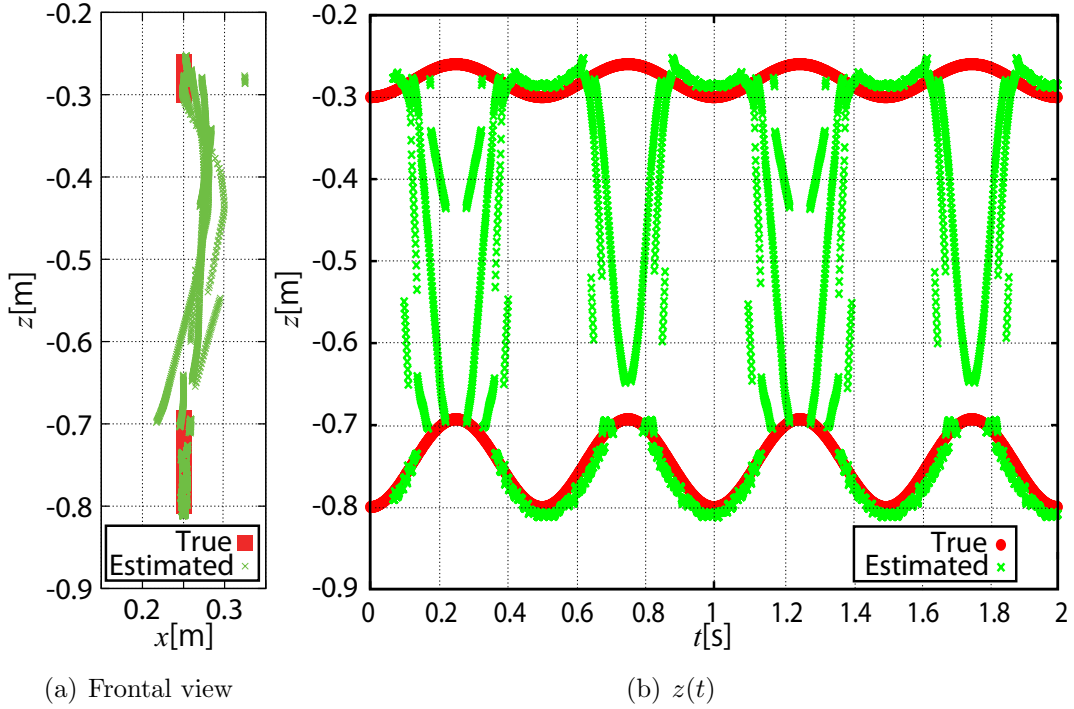
Figure 3.9: Estimated image in the simulation of Fig. 3.7.

occurred. The DOA is estimated using the phase difference between two antennas, as expressed in Eqs. (2.14) and (2.15); however, the phase estimation errors are caused by interference. Fig. 3.10 (a) shows the outline of the phase estimation error at an antenna, where the horizontal and vertical axes are the real and imaginary parts of a received signal. Since this error is occurs at all antennas, the estimated phase differences also have errors. For this reason, the DOA is estimated in the direction where the target does not exist. In addition, amplitude variation of the echo leads to fast motion of the false images. Fig.3.10 (b) shows the effect on the amplitude variation and the phase error that occurred owing to the amplitude variation. For example, in Fig. 3.8, the amplitude ratio of targets 1 and 2 varies from 1.26 to 1.45 in 0.2 s $< t <$ 0.3 s, and scattering centers corresponding to these data move at a velocity of approximately 4 m/s. This velocity is greater than the maximum velocity of the assumed target, which is 2.5 m/s. Therefore, many false images have a velocity greater than the maximum velocity assumed by the motion type.

3.3.2 False Image Rejection Method using Velocity Information

Based on the above discussion, we propose a false image rejection method. First, we reject the estimated points with relatively large velocities and remove the images that satisfy

65

(a) Effect on interference   (b) Effect on amplitude variation
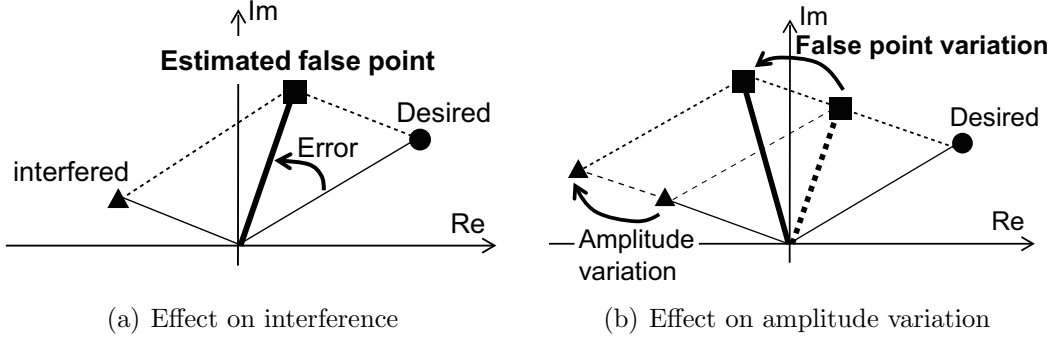
Figure 3.10: Outline of mechanism of false images.

the following condition:

$$v_{\max} < |\mathbf{v}(t, v_{\mathrm{d}})|, \tag{3.1}$$

where $v_{\max}$ is the assumed maximum speed, and $\mathbf{v}(t, v_{\mathrm{d}})$ is the velocity estimated as the time-derivative of a scattering center position as:

$$\mathbf{v}(t, v_{\mathrm{d}}) = \mathrm{d}\mathbf{x}_{\mathrm{s}}(t, v_{\mathrm{d}})/\mathrm{d}t. \tag{3.2}$$

Next, isolated points are removed. We assume a sphere with radius R_{F} whose center is at $\mathbf{x}_{\mathrm{s}}(t, v_{\mathrm{d}n})$, and count the number of scattering centers N_{F} within it. We reject the scattering centers that satisfy the condition:

$$N_{\mathrm{F}}/N_{\mathrm{A}} < \alpha, \tag{3.3}$$

where N_{A} is the total number of estimated points, and $0 < \alpha < 1$ is the threshold ratio of the number of false points to the total number of points. α is empirically determined by the spatial resolution.

Fig. 3.11 shows the estimated image after applying the false image reduction method to the same data as in Fig. 3.6. We empirically set $v_{\max}$=2.5 m/s, $R_{\mathrm{F}} = \Delta R/10 = 3$ cm, and α=0.003. The proposed method removes most of the false images. However, the estimated region becomes small, because weak echoes from some body parts are also suppressed by this simple false image reduction method. For example, the echo intensity from the arms is lower than that from a torso as shown in Fig. 3.5(b).

3.3.3 Adaptive Peak Extraction

For detection of low power echoes, relatively low ρ must be set in Eq. (2.10). However, false peaks caused by interference are not suppressed when threshold ρ is small. Fig. 3.12(a) and (b) shows examples of echo peaks estimated for $\rho = 0.25$ and 0.15. Here, the false image rejection method described in the previous section is applied. As illustrated in
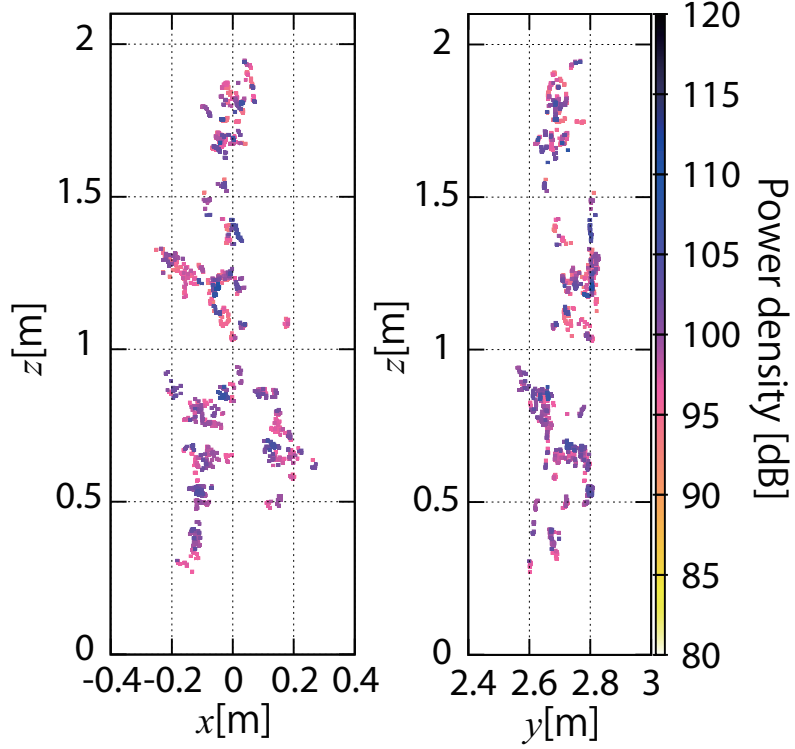
Figure 3.11: Frontal (Left) and side views (Right) of estimated image after applying the false image rejection method.

these examples, number of extracted peaks corresponding to the arms is relatively small for $\rho = 0.25$, and many false peaks remained for $\rho = 0.15$. This is because the threshold that we used was fixed independently of v_{d}. To resolve this problem, we modified the Eq. (2.10):

$$|S_{ij}(t, v_{\mathrm{d}})|^2 > \rho(v_{\mathrm{d}}) \max_{v_{\mathrm{d}}} |S_{ij}(t, v_{\mathrm{d}})|^2. \tag{3.4}$$

This condition means that threshold ρ depends on v_{d}. In walking motion, for example, the swinging motion of the arm has large radial velocity compared with the body oscillation. Thus, if v_{d} is large, $\rho(v_{\mathrm{d}})$ should be small at large $|v_{\mathrm{d}}|$ range for the position (ii).

We next explain how to determine the threshold $\rho(v_{\mathrm{d}})$. As discussed above, $\rho(v_{\mathrm{d}})$ should be changed depending on the echo power. In addition, false echo peaks are not suppressed by the false image rejection method when ρ is set to be small. Consequently, if the amount of interference is relatively large, $\rho(v_{\mathrm{d}})$ should be set to a large value. We divide the radial velocity axis between N_{v} segments: $v_{\mathrm{dmax}} - (k-1)\Delta v_{\mathrm{d}}$-$v_{\mathrm{dmax}} - k\Delta v_{\mathrm{d}}$ ($k = 1, 2, \cdots, N_{\mathrm{v}}$) where $\Delta v_{\mathrm{d}} = 2v_{\mathrm{dmax}}/N_{\mathrm{v}}$ and v_{dmax} is the maximum radial velocity. The threshold for each segment k is defined as $\rho(k\Delta v_{\mathrm{d}})$. For each segment k, the following procedures determine $\rho(k\Delta v_{\mathrm{d}})$:
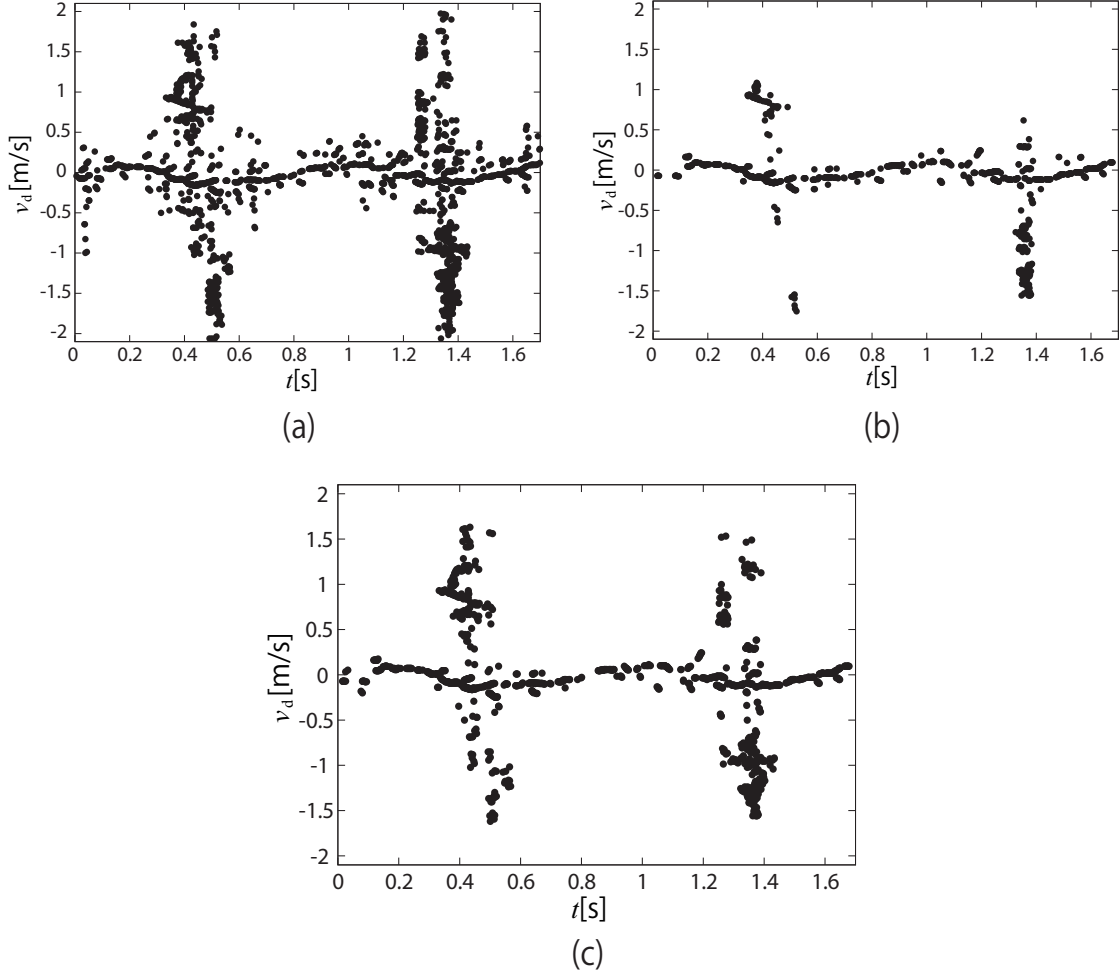
Figure 3.12: Extracted peaks from spectrogram in position (ii). (a) with ρ=0.15, (b) with ρ=0.25 and (c) with proposed method.

1. Estimate the maximum power density $P_{\mathrm{max}k}$ and noise power density $P_{\mathrm{N}k}$, and set $\rho_k = \gamma P_{\mathrm{max}k}/P_{\mathrm{N}k}$.

2. Extract the peaks satisfying Eq. (3.4) for $\rho(k\Delta v_{\mathrm{d}}) = \rho_k$ and obtain an image.

3. Count the number of points $N_{\mathrm{I}k}$ satisfying Eqs. (3.1) and (3.3).

4. Estimate $\beta_k = N_{\mathrm{I}k}/N_{\mathrm{A}k}$, where $N_{\mathrm{A}k}$ is the total number of estimated points.

5. If $\beta_k < \beta_{\mathrm{th}}$ or $N_{\mathrm{A}k} = 0$, determine $\rho(k\Delta v_{\mathrm{d}}) \leftarrow \rho_k$. Otherwise, $\rho_k \leftarrow \rho_k + \Delta\rho$ and go to 2.

Fig. 3.12(c) shows the peaks extracted using the proposed extraction method. We empirically set $N_{\mathrm{v}} = 16$, $\beta_{\mathrm{th}} = 0.6$, $\gamma = 1/10000$ and $\Delta\rho = 0.01$. This figure indicates that

START

Acquisition of signals $s_{ij}(t)$

Calculation of $S_{ij}(t, v_{\mathrm{d}})$ by SDFT

Initial ρ_k determination

Peak extraction with ρ_k

Scattering center positioning

False image detection and rejection

$N_{\mathrm{A}k} = 0$ or $\beta_k < \beta_{\mathrm{th}}$ for all segment k ?

Update ρ_k

No

Yes

Output imaging result
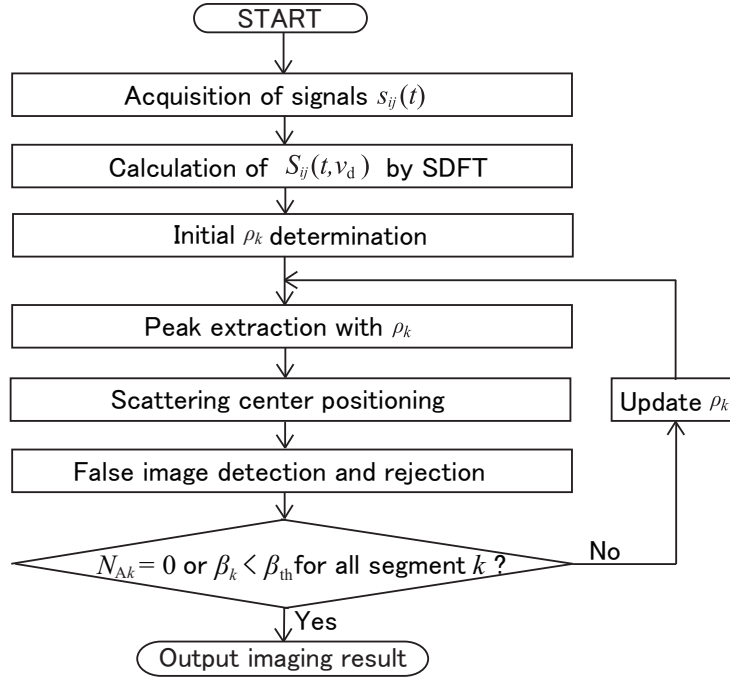
Figure 3.13: Procedure of proposed imaging algorithm.

peaks corresponding to both the body and the arms are accurately extracted. Moreover, number of false peaks is reduced compared with the image in Fig. 3.12(b) for a fixed-threshold $\rho = 0.15$.

The procedure of the proposed imaging algorithm is summarized in Fig. 3.13. The proposed algorithm generates images using the UWB Doppler interferometric imaging algorithm described in Chapter 2 and extracts reliable images using the methods described in Sections 3.3.2 and 3.3.3.

3.4 Results and Discussion

3.4.1 Human Imaging Results and Performance

Fig. 3.14 shows the estimated image after applying the adaptive peak extraction method to the data of Fig. 3.11. The estimated region becomes large without increasing number of false images, and an outline of the human body is estimated. In addition, the proposed imaging algorithm also acquires the radial velocity of each estimated scattering center. Fig. 3.15(a) shows the radial velocity of Fig. 3.14. This figure indicates that radial velocities corresponding to the walking motion were detected. From the data of Fig. 3.14, when the right foot swings forward, the positive radial velocity corresponding to this motion is observed, and the left foot has negative radial velocity. In addition, Fig 3.15(b) shows
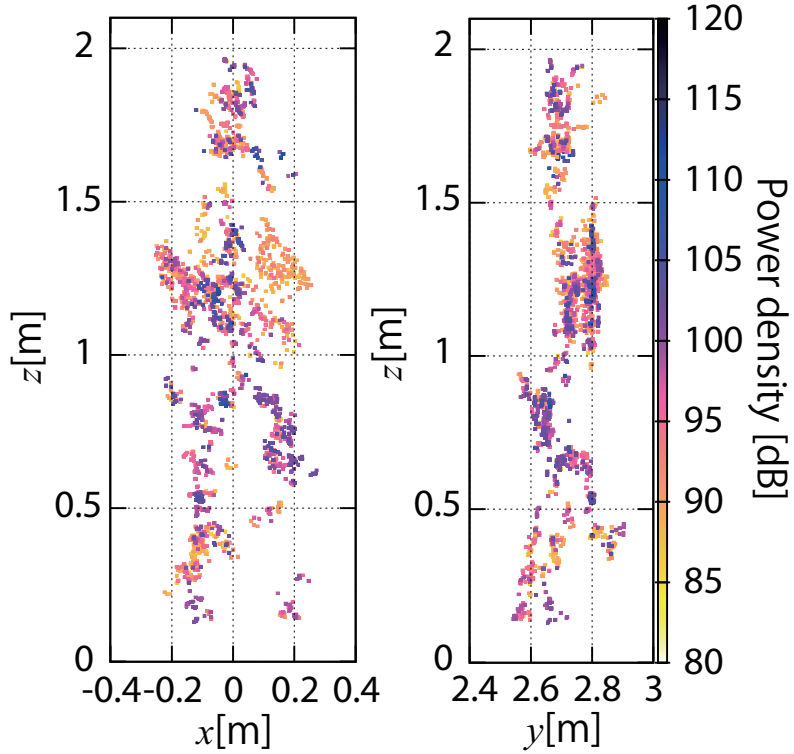
Figure 3.14: Frontal (Left) and side views (Right) of estimated image using the proposed imaging algorithm.

the image estimated from the data of the next half of a walking cycle of Fig. 3.15(a). The signs of the radial velocities of the legs and arms are reversed compared with Fig. 3.15(a). This important pedestrian feature is observed.

Next, we investigate accuracy of the estimated image from its side view. We compare the scattering center positions extracted from the video and the image estimated by the proposed imaging algorithm. A scattering center is the position where a radar radial direction and a target surface intersect perpendicularly. We calculate such points from the video. Fig. 3.16 shows the scattering center position extracted from the video and estimated side views in positions (ii) and (iii). Although many estimated scattering centers are matched, some imaging points are estimated where scattering centers are not obtained from the video. In Fig. 3.16(b), the extraction of the scattering centers corresponding to shoes from the video is difficult. Thus, we might think that the imaging points near $(y, z) = (2.85$ m, 0.4 m$)$ and $(2.7$ m, 0.35 m$)$ correspond to the shoes. Similarly, in Fig. 3.16(a), strict scattering center estimation from the body is difficult. However, we can confirm that many scattering centers are accurately estimated except for such points. These results verify that the proposed imaging algorithm achieves adequate human imaging in a real environment and can acquire features of the image motion.
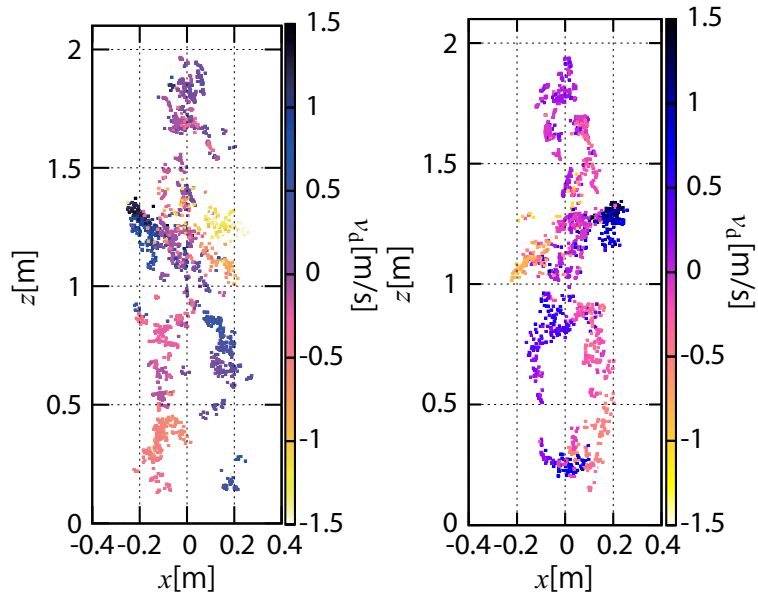
(a) With data of Fig. 3.14

(b) With data of next half of a walking cycle of Fig. 3.14

Figure 3.15: Radial velocity of each estimated point.

(a) Position (ii)

(b) Position (iii)
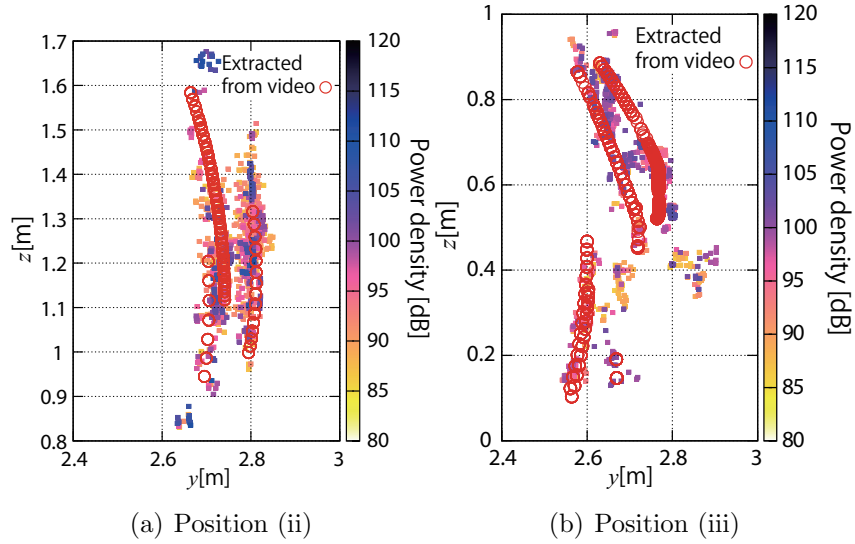
Figure 3.16: Estimated points and scattering centers extracted from the video in side view

Moreover, we investigate the real-time capability of the proposed algorithm. We used the data of half a walking cycle (0.78 s) to acquire the image depicted in Fig. 3.14. For the purpose of real-time imaging, time-variation of the estimated image aquired with the relatively short-time data is important. Fig. 3.17 shows the time variation of Fig. 3.15(a) with time steps of 0.1 s at $t < 0.7$ s. We are able to recognize the motion of each body part by comparing Figs. 3.17 and 3.15(a). For instance, when the right foot swings forward, we observe the radial velocity and position variations corresponding to this motion. In addition, the left foot have negative radial velocity. As discussed above, a pedestrian's features are detected in Fig. 3.17. We are able to identify a pedestrian in the real-time imaging system from these results.

3.4.2   Shape/Motion Parameter Extraction

This subsection describes shape/motion parameter extraction examples. These parameters might be effective for human identification. We extract these parameters: walking cycle, step, shoulder width, and height. A walking cycle corresponds to two spectrogram cycles. Hence we estimate the cycle of the spectrogram T_s using the Fourier transform, and then the walking cycle is estimated as $T_w = 2T_s$. Next, a walking step is estimated from T_w and the walking velocity. The walking velocity is estimated by deriving it from the scattering centers of the body. However, in this study, a pedestrian is walking on a treadmill; therefore the walking velocity v_w is set as the treadmill's belt speed. Walking step A_w is estimated by:

$$A_w = \frac{v_w T_w}{2}.$$ (3.5)

Shoulder width and height are directly estimated from a frontal view of the human image. The maximum and minimum values of the estimated image in terms of the x axis are x_{max} and x_{min}. Shoulder width L_s is estimated by:

$$L_s = x_{max} - x_{min}.$$ (3.6)

In the same way, height L_h is estimated by:

$$L_h = z_{max} - z_{min}.$$ (3.7)

Table 3.1 shows the true and estimated parameters of a pedestrian target of Fig. 3.3. We use the same data as in Fig. 3.15. All parameters were accurately extracted.

Next, we demonstrate the parameter extraction for identification of a variety of pedestrians. Table 3.2 shows the assumed targets and their heights and steps. We assume three pedestrian subjects whose heights are different. Each pedestrian walks with three types of steps on the treadmill. We identify nine types of targets by extracted height L_h and step A_w and measure them sequentially. The experimental setting and parameters are the same as in the previous section. Fig. 3.18 shows the relationship between the extracted
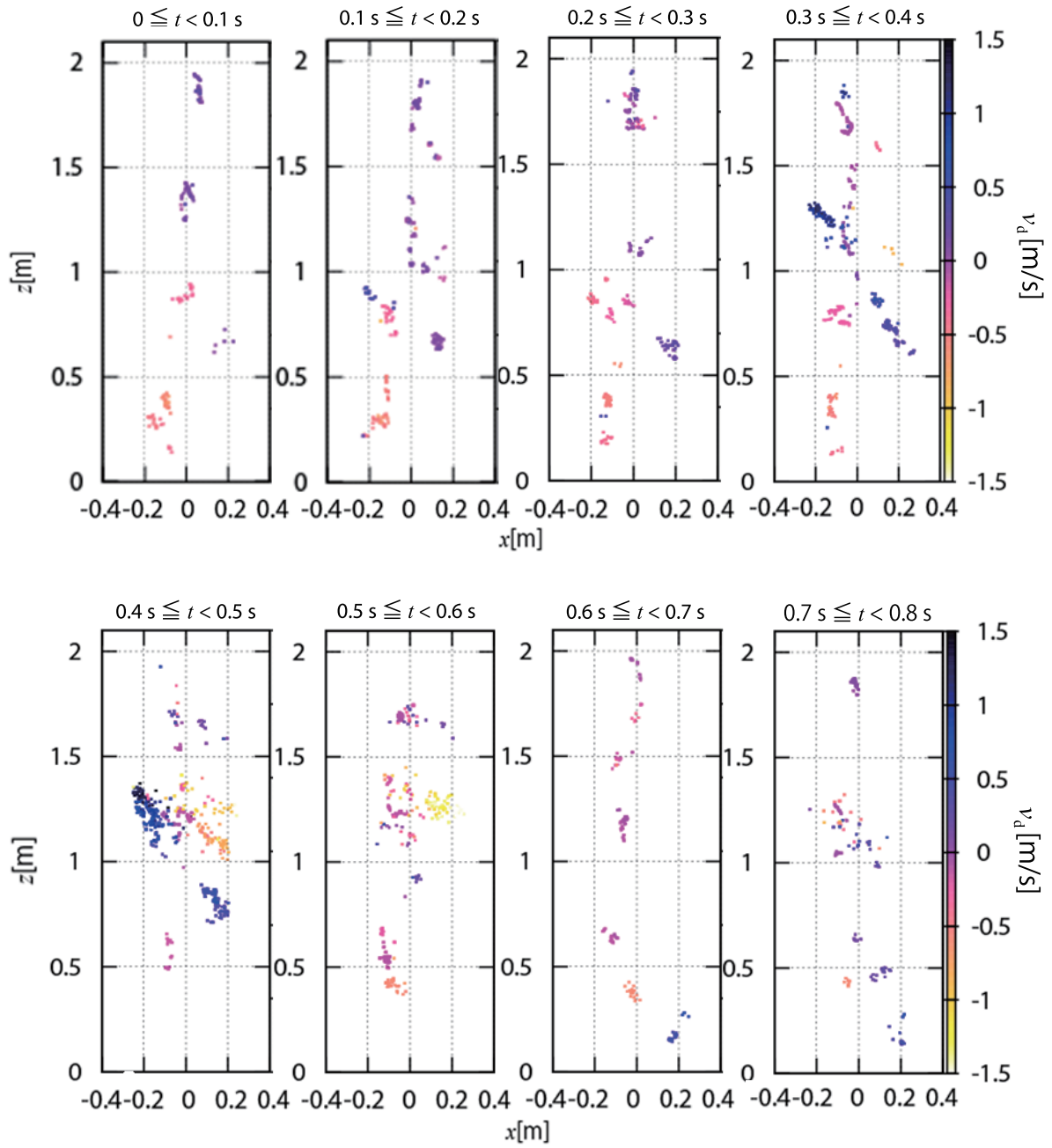
Figure 3.17: The time variation of the estimated human image of Fig. 3.15(a) in $t < 0.8s$.

Table 3.1: True and estimated parameters for target of Fig. 3.3.

Parameter	True	Estimated
Walking cycle T_w	1.44 s	1.50 s
Step A_w	60.0 cm	62.5 cm
Shoulder length L_s	46.0 cm	49.4 cm
Height L_h	182 cm	184 cm

Table 3.2: Assumed targets for the experiment of shape/motion parameter extraction, and their true heights and steps.

	Target A	Target B	Target C
Height	182 cm	170 cm	158 cm
Step a (small)	46 cm	44 cm	44 cm
Step b (middle)	60 cm	52 cm	52 cm
Step c (large)	67 cm	64 cm	58 cm

A_w and L_h. In this figure, we used the data of a walking cycle to estimate A_w and L_h, and plot the parameters of five walking cycles for each target. We realized accurate parameter extraction, and it is easy to recognize that nine types of data were used. The mean errors of A_w and L_h are 1.45 cm and 4.17 cm. These results verify that accurate extraction of walking parameters is achieved from the human image estimated by the proposed imaging algorithm, and target identification with these parameters can be realized.

3.4.3 Application to a Pedestrian Target Walking Toward the Antennas

In this subsection, we assume an actual pedestrian target without a treadmill, and clarify the performance of the proposed imaging algorithm in a realistic situation. Fig. 3.19(a) shows the experimental site. The target walks from $(x, y) = (0, 3.9 \text{ m})$ to $(0, 1.5 \text{ m})$ with a walking step of 0.6 m and a mean speed of 0.86 m/s. Height of the examinee is 1.75 m. We
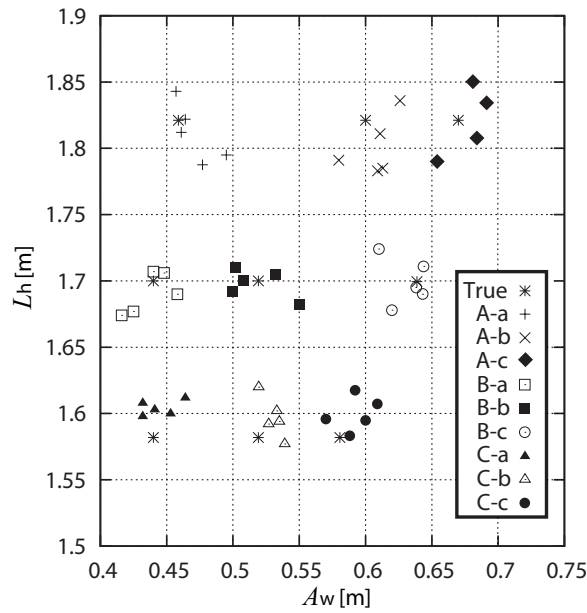
Figure 3.18: Relationship between extracted A_w and L_h of each target.

(a) Experimental site
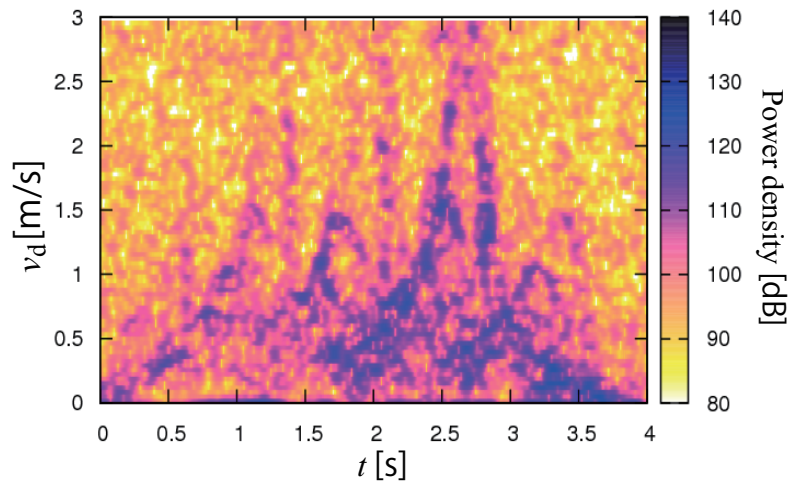
(b) Summation of the spectrograms for range bins

Figure 3.19: Experimental setup and spectrogram at $z_\mathrm{c} = 0.36$ m of a pedestrian target without a treadmill.

measure at four antenna positions: z_c=0.36, 0.82, 1.29, and 1.54 m. We measured data at not three but four different positions in this case because three antenna positions cannot cover the whole body when the target is close to the radar system. Fig. 3.19(b) shows
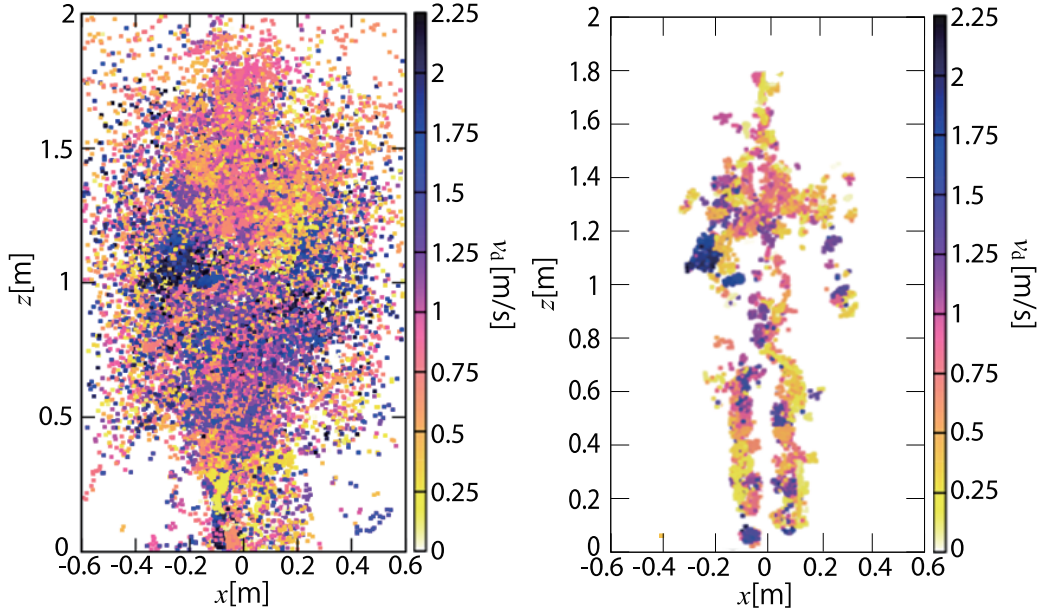
Figure 3.20: Frontal views of the estimated image without (left) and with (right) the false image rejection method.

the summation of the spectrograms for all range bins at $z_c = 0.36$ m. The radial velocity variations of his legs are confirmed, and the offset of the spectrograms corresponds to the mean walking speed.

Fig. 3.20 shows the frontal views of the estimated image without and with the proposed false image rejection method using the data of $t \geq 1.5$ s. This is because that the SNR at $t < 1.5$ s is insufficient for an imaging. Parameters v_{max}, R_F, and α have the same values as in the previous section. With only UWB Doppler radar interferometry, many false images are confirmed and human outline is not recognized. In contrast, the proposed algorithm extracts the outline of the human and the radial velocity features of the walking motion. These results mean that the proposed imaging algorithm can reject almost false images and relizes the reliable and high-resolution human imaging in a realistic situaion. Fig. 3.21 shows the side view of the estimated image by the proposed imaging algorithm. We can see the walking motion which corresponds to three steps. In $z < 0.8$ m, the scattering centers with relatively large velocities corresponds to the swinging of the leg, and the scattering centers with small v_d corresponds to the other leg in contact with the ground. Moreover, the arm swinging motion is detected as relatively large velocities over about 0.8 m $< z <$ 1.3 m. These results mean that we can recognize the walking motion features, and the effectiveness of our proposed algorithm is also confirmed for an actual pedestrian target without a treadmill.

In addition, the real-time imaging result is presented. Figs. 3.22 and 3.23 show the
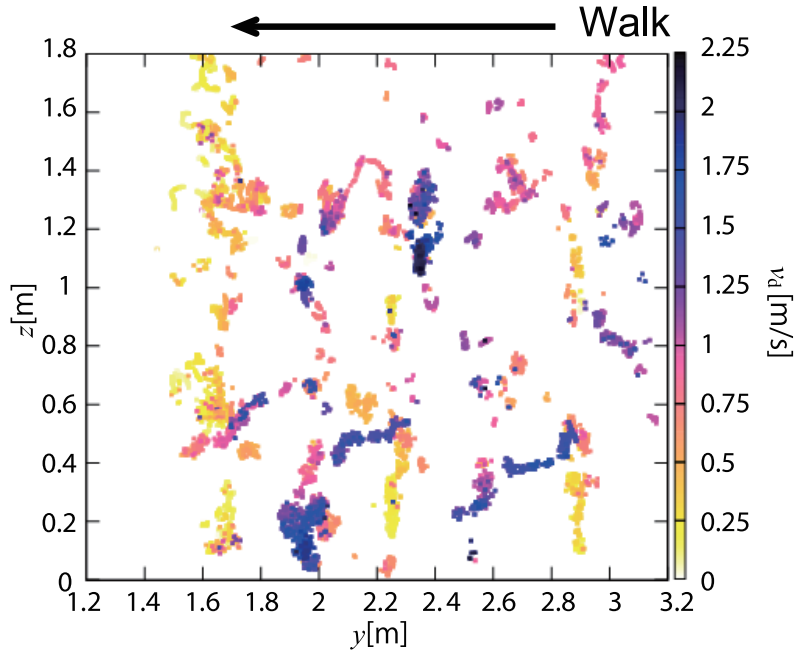
Figure 3.21: Side view of the estimated image shown in Fig. 3.20.

time variation of the frontal and side images of Fig. 3.20 with time steps of 0.1 s. As shown in these figures, the pedestrian features are even detected using real-time images. We can confirm that the time variation of the legs corresponding to the walking motion is the same as in Fig. 3.17. Moreover, as shown in Fig. 3.23, the translation of the body and the swinging of the hands and feet that accompany the walking are confirmed. The time variation of the estimated points with a relatively high velocity at $z < 0.6$ m corresponds to the forward motion of the foot. These results show that we achieved real-time pedestrian identification using the proposed imaging algorithm in a realistic situation.

3.4.4 Imaging Examples of a Pedestrians Moving in Various Directions

This subsection shows imaging examples of pedestrian targets having a variety of directions. The parameters of the radar and the proposed algorithm are the same as in the previous section. First, we assume a pedestrian who walks away from the radar. The target walks from (x, y)=(0 m, 1.5 m) to (0 m, 3.9 m) with a walking step of 0.6 m and a mean speed of 0.86 m/s. The height of the examinee is 1.63 m. Fig. 3.24 shows the frontal and side views of the estimated image using the data with sufficient signal-to-noise ratio. This figure confirms that the human outline and the features of walking motion are obtained same as the example described in the previous section.
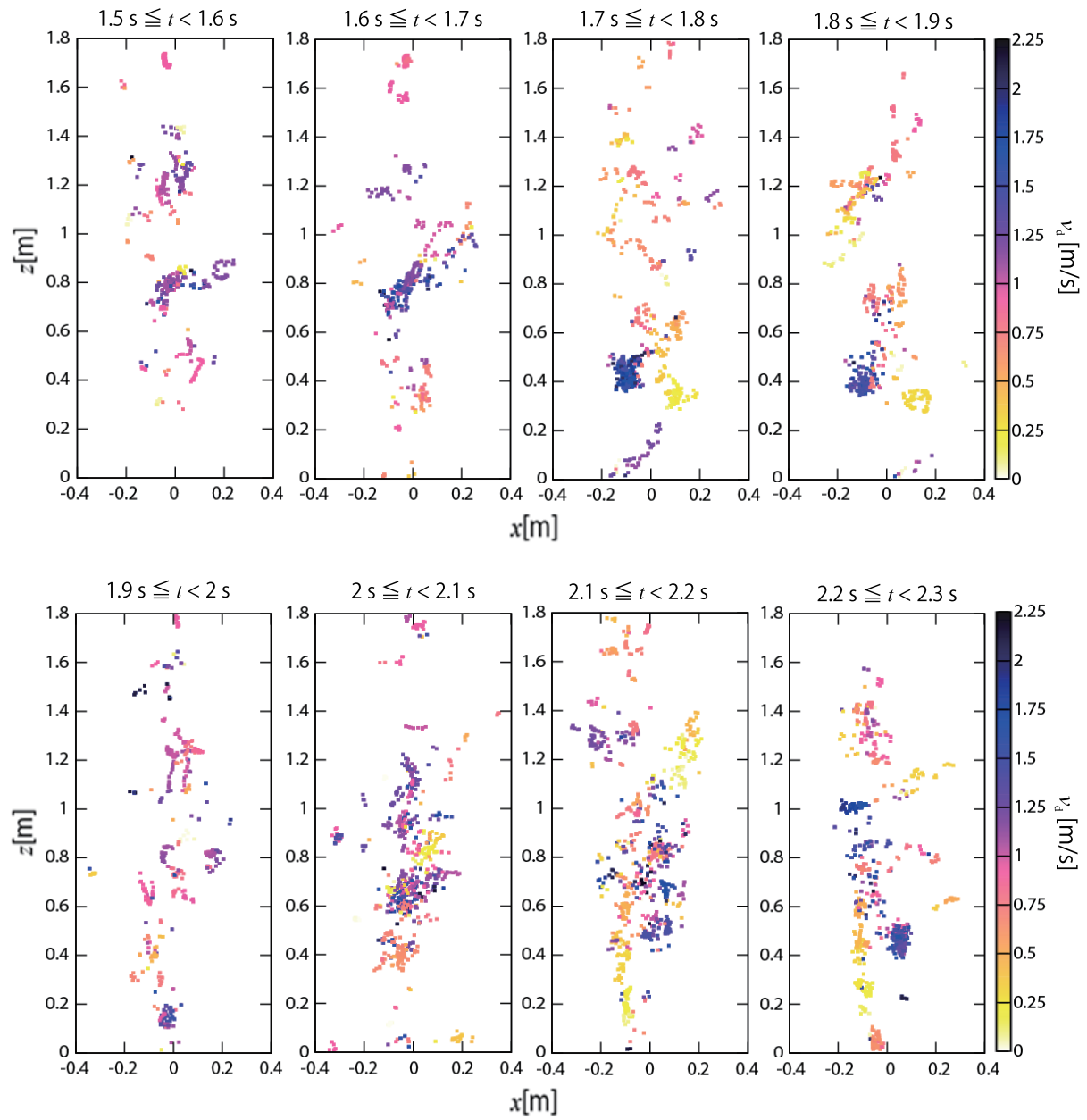
Figure 3.22: Time variation of the frontal view of the estimated image of Fig. 3.20 in 1.5 s $\leq t < 2.3$ s.
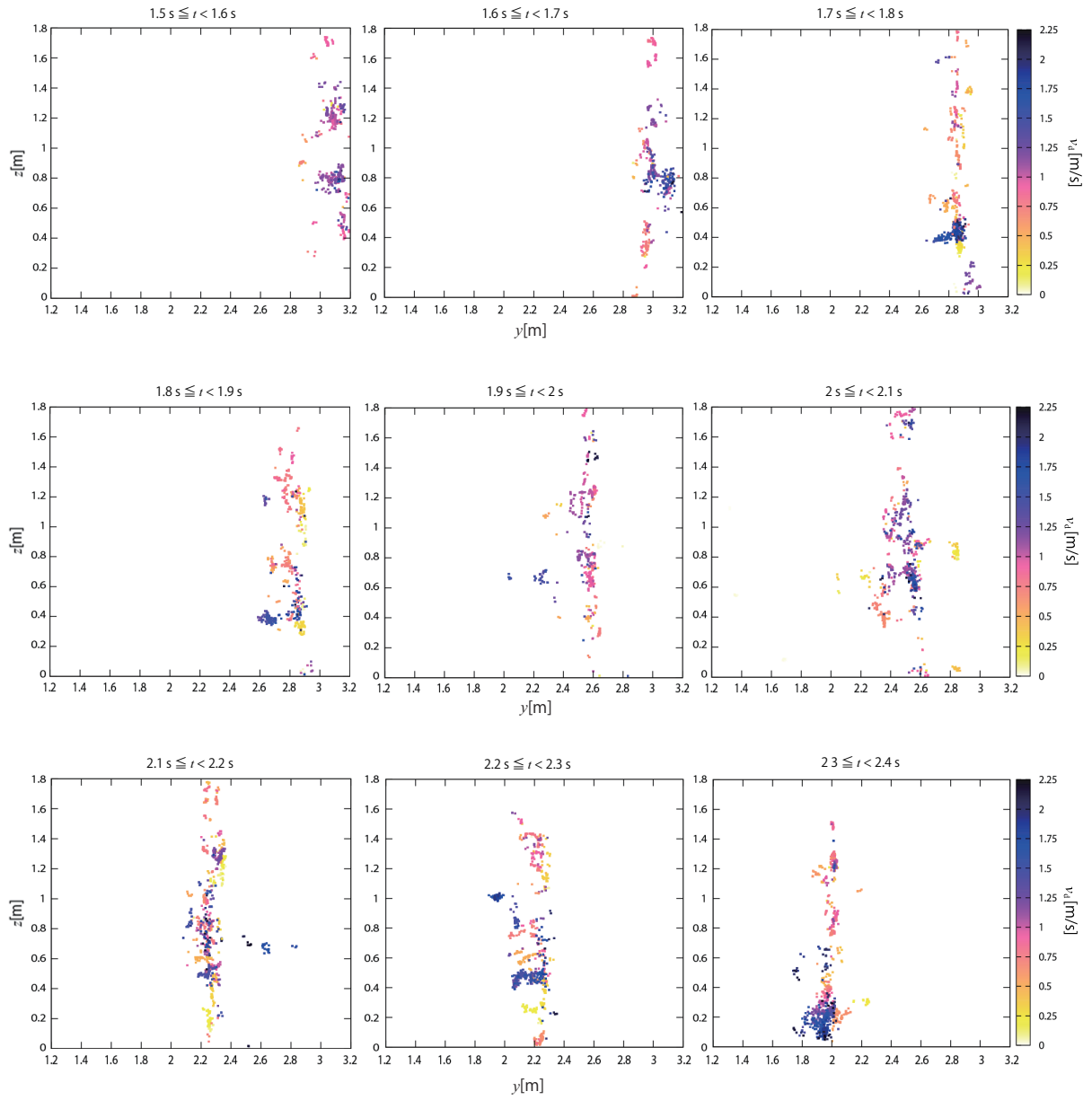
Figure 3.23: Time variation of the side view of the estimated image of Fig. 3.20 in 1.5 s $\leq t < 2.4$ s.
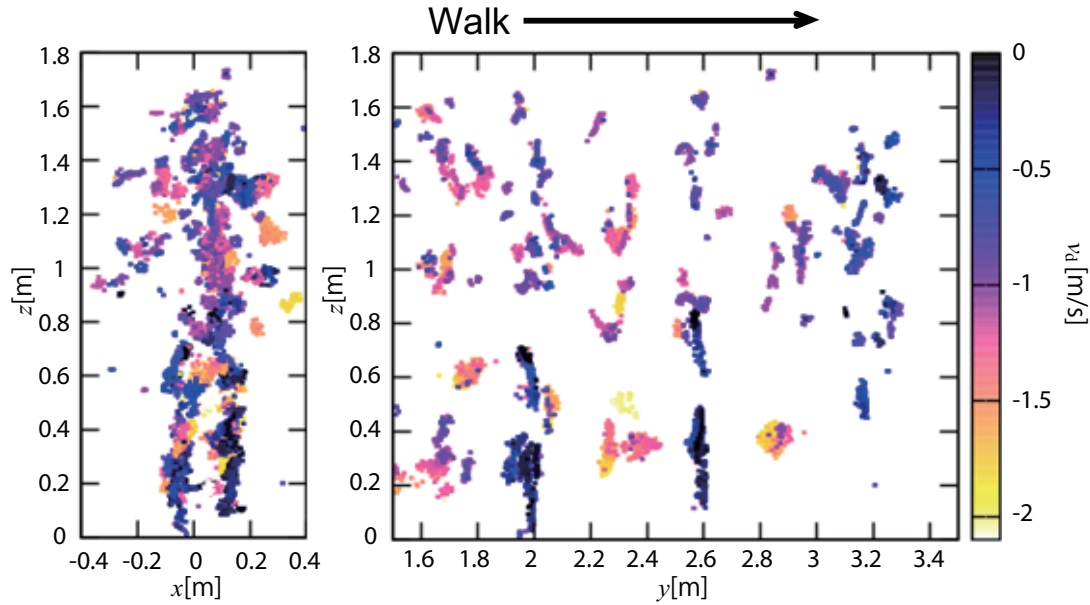
Figure 3.24: Frontal (Left) and side views (Right) of estimated image of a pedestrian who walks away from the radar along the y-axis.

Finally, we show the imaging results of pedestrians having oblique walking directions. We assume two scenarios: case A assumes the target walks from (x, y)=(-1.03 m, 2.69 m) to (1.03 m, 1.51 m) and case B assumes the target walks from (x, y)=(-1.03 m, 2.41 m) to (1.03 m, 1.79 m). In both scenarios, the mean speed and the height of the target are 0.8 m/s and 1.78 m. Fig. 3.25 shows the top and frontal views of the estimated image for case A, where X is the axis perpendicular to the walking direction. We use the data which corresponds to the target within the beam illumination area. Although the number of scattering centers in the relatively large X is small because of shadowing, a human outline and walking orbit are sufficiently detected. Fig. 3.26 shows the top and frontal views of the estimated image for case B. The radial velocities become small compared with case A because the walking orbit is close to cross-range direction. In addition, the effect on the shadowing is larger than case A. However, the walking orbit and the human outline are extracted to some extent. These results indicate that the proposed imaging algorithm is applicable to target motion with arbitrary directions.
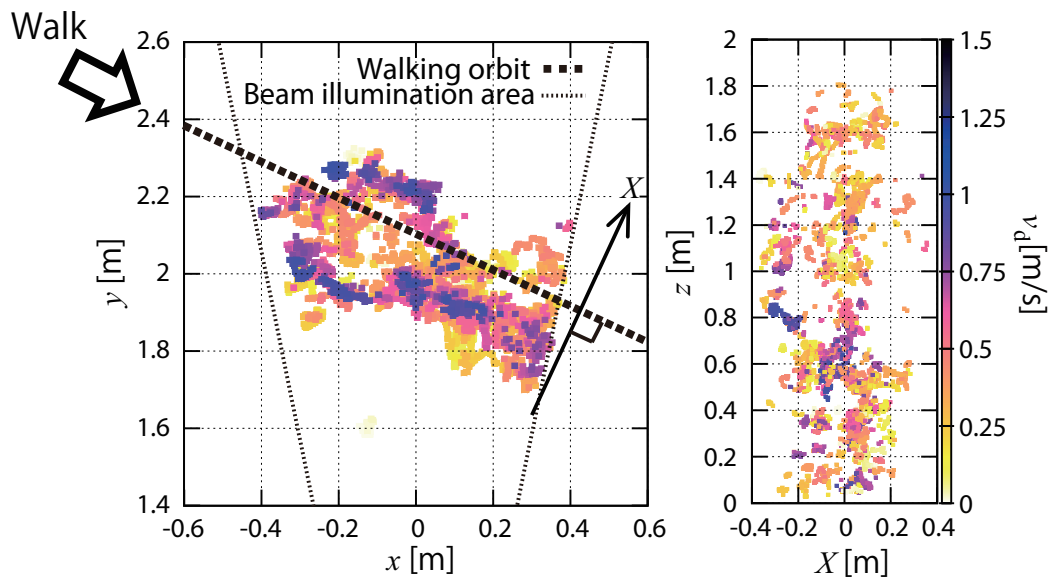
Figure 3.25: Top (Left) and frontal views (Right) of estimated image of a pedestrian with an oblique walking direction (case A).
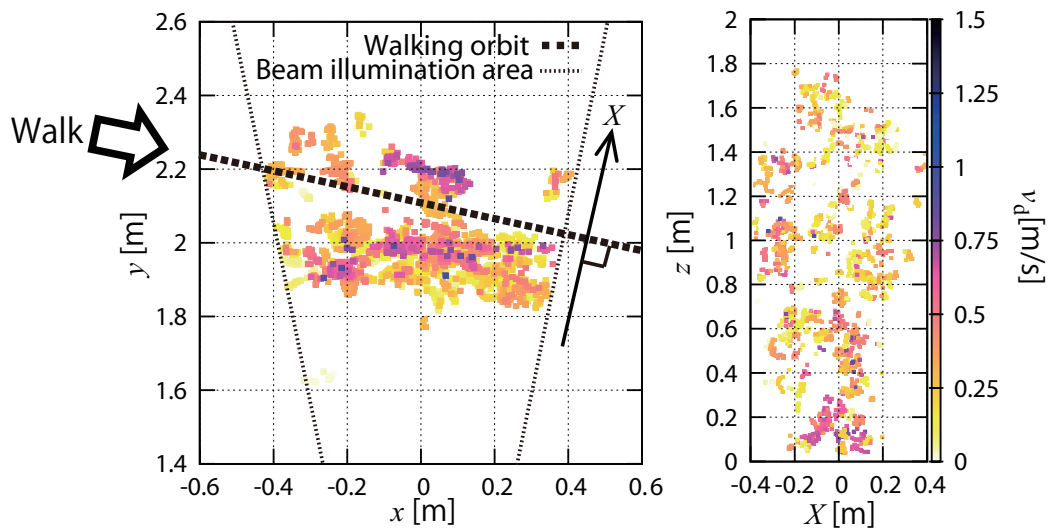
Figure 3.26: Top (Left) and frontal views (Right) of estimated image of a pedestrian with an oblique walking direction (case B).

3.5 Conclusions

This chapter proposed the human imaging algorithm with the UWB Doppler radar interferometry. The experimental example showed that its use for the human imaging yields many false images because of interferences of body parts. We then clarified the mechanism of such false images, and proposed false image detection and rejection methods using velocity information. The experiment, which assumed a pedestrian on a treadmill, indicated that the proposed imaging algorithm achieved adequate and reliable human imaging. Walking motion features were also confirmed. We also examined shape and motion parameter extraction, and verified that accurate parameters can be extracted from the estimated human images. Moreover, we conducted experiments that assumed an actual pedestrian target without a treadmill. These experiments verified that the proposed imaging algorithm achieved estimation of a human outline and a walking orbit for the pedestrian targets walking in various directions. In addition, the real-time capability of the proposed imaging algorithm was confirmed. As verified in these results, the proposed imaging algorithm can generate high-resolution, reliable and real-time human image with a low-complexity system in a realistic environment. For practical use, the subsequent chapters consider human identification applications based on UWB Doppler radar imaging results.

Chapter 4

Pedestrian Classification Based on Radial Velocity Features

4.1 Introduction

Motion classification is one of important problems for target identification in human monitoring systems. Many researchers have challenged to realize a classification of a various motion types using micro-Doppler radars as reviewed in Section 1.3.3. However, reliable long-term data (at least 2 s [84, 103]) and/or complicated procedures were needed to accurately classify motion with the conventional methods and the accuracy and real-time capabilities of these methods are therefore inadequate. These were because that they used only information of the time-frequency distributions. Thus, a utilization of real-time human images has a great potential to overcome these problems.

This chapter presents an accurate and real-time pedestrian classification algorithm based on UWB Doppler radar images. We consider a classification of three groups of pedestrians mainly in a hospital monitoring environment: a normal pedestrian group, a group using crutches and group with wheelchairs. In addition, we consider a classification of more detailed pedestrian types. Three types of human gait for the normal pedestrian group are assumed: with swinging arms, holding a bag with one hand, and without swinging arms. The target group with wheelchairs is composed of two types: a pedestrian pushing a person in a wheelchair and a person driving himself in a wheelchair. This chapter deals with the classification of these three groups and six types of pedestrians. We experimentally acquire images of these types of pedestrian with the imaging algorithm proposed in Chapter 3, and discuss the features of each pedestrian image. We then propose feature parameters extracted from the silhouette of the estimated images and their radial velocity distributions, and describe a classification algorithm using these parameters and a k-nearest neighbor (k-NN) algorithm [127] which is explained in Section 1.3.3. The results reveal that three groups and six types of pedestrians are accurately classified in real-time by the proposed classification algorithm.

4.2 Imaging of Various Types of Pedestrians

This section presents examples of imaging various types of pedestrians in the experiment, and discusses the features of each image. Fig. 4.1 has photographs of the types of pedestrians we assumed. This study took into account the classification of three groups and six types of pedestrians. We assumed three groups of pedestrians: targets in group A were walking targets with normal leg motion, targets in group B were pedestrians with a three-point crutch swinging gait, and targets in group C were walking with a wheelchair. Moreover, target group A had three walking styles: target A-a was a normal pedestrian who swung his arms, target A-b carried a bag in one hand, and target A-c walked with his hands in his pockets. Target group C had two target types: target C-a was a pedestrian pushing a person in a wheelchair, and target C-b was a person propelling himself in a wheelchair. All targets walked from (x, y) =(0, 3.9 m) to (0, 1.5 m). The mean speeds of target groups A, B, and C were 0.8, 0.76 and 0.7 m/s, and they walked at an approximately constant speed. The parameters of the radar and the imaging algorithm are same as in Section 3.4.3. We use data corresponding to one cycle of a time-frequency distribution (corresponding to half of the walking cycle) for imaging and classification.

Fig. 4.2 shows the frontal views of the estimated images for all pedestrian types. As we can see from Fig. 4.2(a), there is an outline of the human shape in all the frontal views of the estimated images. Moreover, we can recognize from radial velocity information that the left leg and the right arm have forward motion in this half of the walking cycle. Although target A-b has nearly the same properties as target A-a, the number of scattering centers corresponding to arms is relatively small as seen in Fig. 4.2(b). This is because his arm-swing amplitude is limited because of having the bag. We can observe the scattering centers on the bag at approximately (x, z) =(0.25 m, 0.5 m), as shown in Fig. 4.2(b). Fig. 4.2(c) indicates that scattering centers corresponding to arms have not been acquired. This is because the peaks corresponding to the arms were not detected because radial velocities of arms and torso were almost same values due to NAM. Since the UWB Doppler radar interferometry separates targets based on difference of their radial velocities, the separation of arms and torso is difficult in this case. We can confirm the images of crutches and their relatively high velocities that correspond to their forward motion as seen in Fig. 4.2(d). Although the radial velocities of both crutches have close value, a separation of these is realized because walking with strict same crutches' motion is very difficult. Fig. 4.2(e) shows the scattering centers are concentrated in a relatively narrow region in terms of both the position and v_{d}. This is because the wheelchair was moving toward the radar at an approximately constant velocity. The same feature can also be confirmed in target C-b. Moreover, we can confirm scattering centers that slightly correspond to arm motion from Fig. 4.2(f) at approximately (x, z) =(-0.2 m, 0.75 m), and the image is shorter than those of the other types. These results indicate that the method of UWB Doppler radar imaging extracts various characteristics of pedestrians, and the features of each pedestrian may be confirmed from the estimated images and v_{d} information.
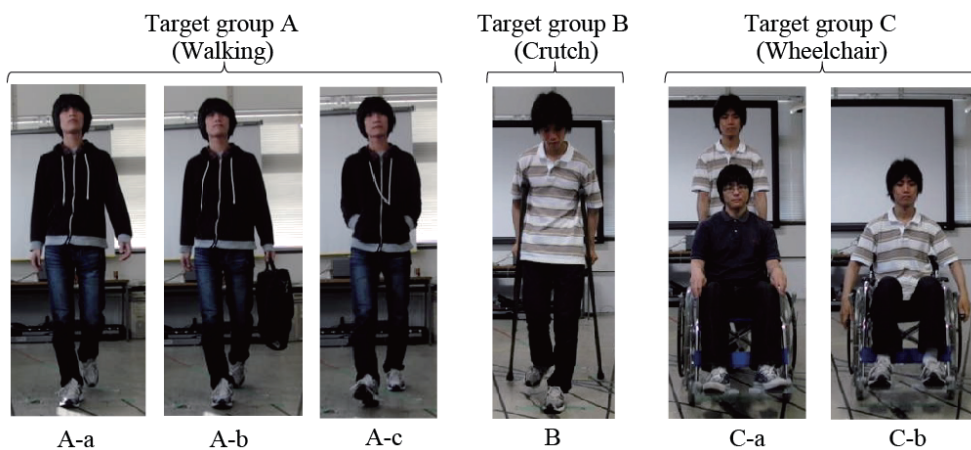
Figure 4.1: Assumed pedestrian types.
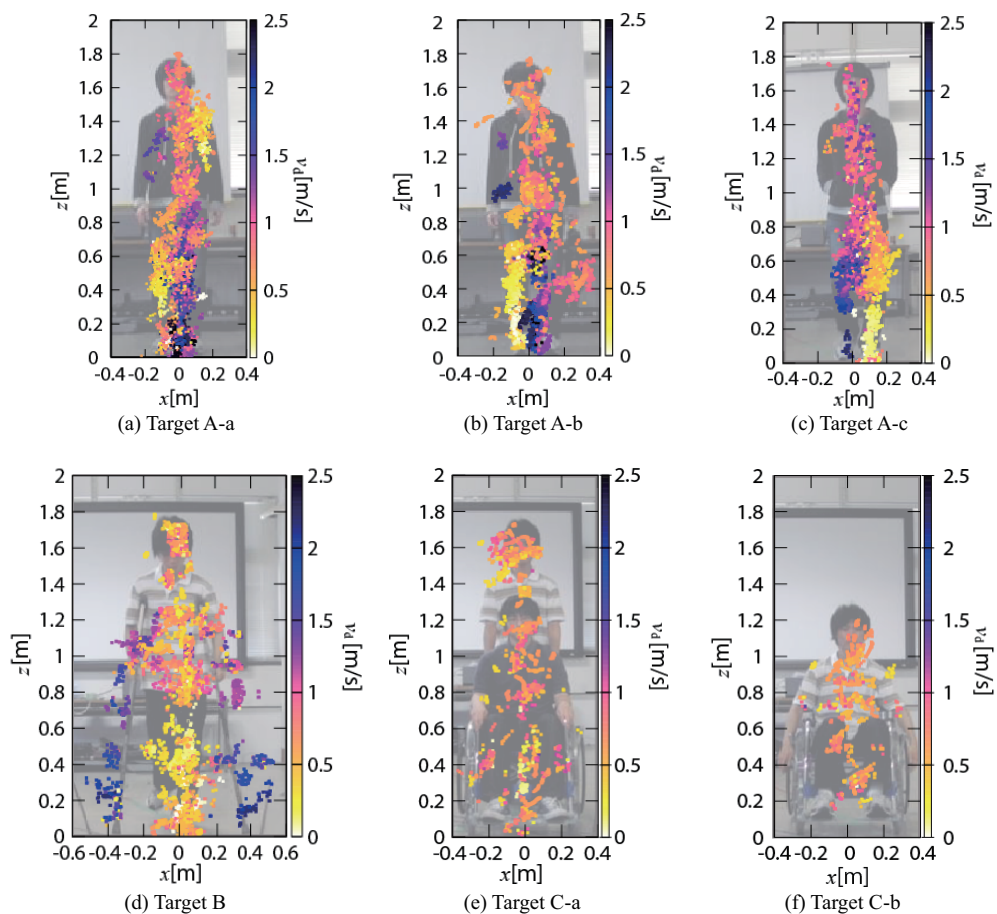
Figure 4.2: Frontal views of the images for all pedestrian types.

85

4.3　Feature Parameter Extraction

4.3.1　Silhouette Extraction from Frontal Image

We propose feature parameters for pedestrian classification in this section. Our proposed feature parameters are extracted from silhouettes and radial velocity distributions of the estimated UWB Doppler radar images. First, we extract the shape of an image silhouette. For example, the important difference between target C-b and others is the height of the image, and this is estimated as the silhouette's height. Fig. 4.3 shows an outline of our proposed silhouette extraction method, which is explained below:

1. Scan an ellipse whose minor axis is parallel to the x-axis and major axis is parallel to the z-axis in the xz plane. The length of the major and minor axes are defined as R_z and R_x.

2. Count the number of estimated scattering centers $N_s(x_{ec}, z_{ec})$ within each ellipse whose central position is (x_{ec}, z_{ec}).

3. If $N_s(x_{ec}, z_{ec}) > \gamma N_A$, points on the ellipse (x_e, z_e) are candidates for the silhouette, where γ is the threshold ratio of N_s to number of the whole estimated points N_A.

4. Extract the maximum and minimum x_e from the candidate points for each z_e, and these silhouette points are defined as $x_{max}(z)$ and $x_{min}(z)$ ($z_{maxe} < z < z_{mine}$), where z_{maxe} and z_{mine} are the maximum and minimum of z_e.

Fig. 4.4 shows the estimated image silhouette of Fig. 4.2(b). We empirically set R_x=2 cm, R_z=10 cm, and γ=0.004. The silhouette of the image is extracted as can be seen from this figure.

We then extract the parameters for the silhouette shapes. First, the height of the silhouette is extracted as:

$$H_S = z_{maxe} - z_{mine}. \tag{4.1}$$

Next, we extract the width and center of the silhouette in the high and low z regions. These are used to extract parameters of the radial velocity features, which is described in the next section. We extract the mean width of the silhouette in the high z region as:

$$W_H = \mathrm{E}[x_{max}(z) - x_{min}(z) \mid z > \alpha_H H_S], \tag{4.2}$$

where $\mathrm{E}[X \mid C_1, C_2, \cdots]$ means the average of X which satisfy conditions $C_1, C_2, \cdots$, and $\alpha_H < 1$ is a threshold ratio of z to the height H_S. A mean center in terms of x in high z region is estimated as:

$$x_{cH} = \mathrm{E}[\{x_{max}(z) + x_{min}(z)\}/2 \mid \alpha_H H_S]. \tag{4.3}$$

Moreover, we extract W_L and x_{cL}, which is determined by using the silhouette that satisfies $z < \alpha_L H_S$ in the same way.
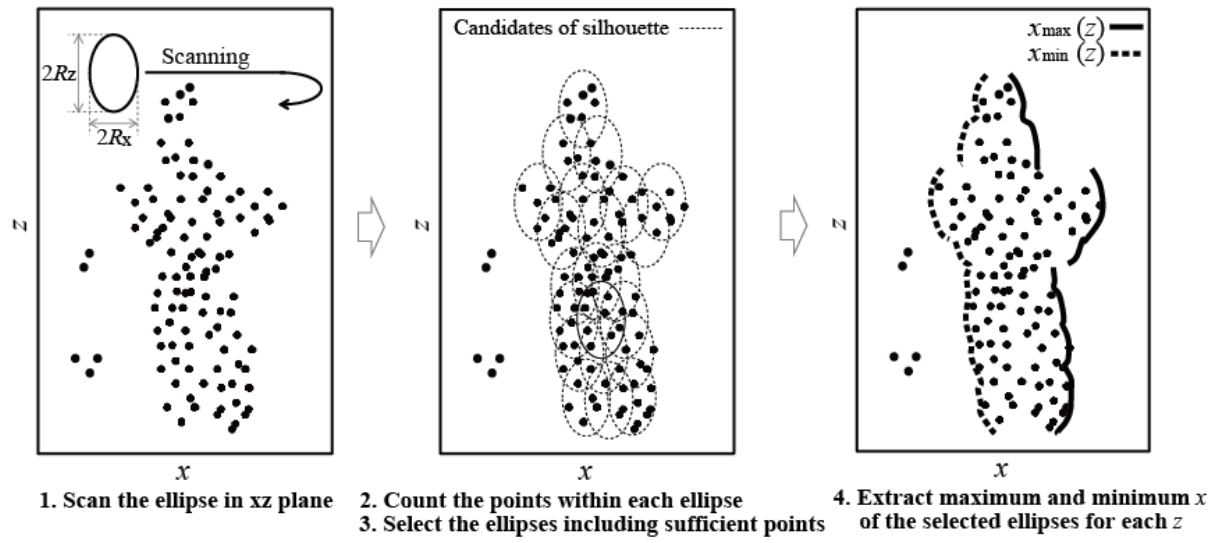
Figure 4.3: Outline of the proposed silhouette extraction method.
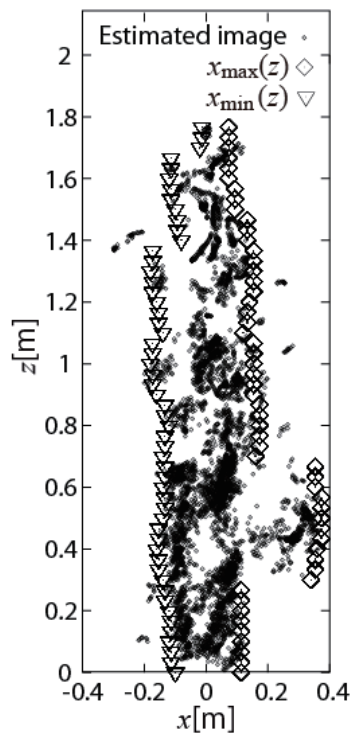
Figure 4.4: Extracted silhouette of the image in Fig.4.2(b).

87

4.3.2 Parameters of Radial Velocity Distribution in Each Region of the Image

We propose feature parameters based on the radial velocity features of the estimated images in this subsection. First, we examine radial velocity distributions in the relatively low z region to classify target groups A, B and C. Fig. 4.5(a) shows the radial velocity distributions of the estimated images of Figs. 4.2 (a),(d),and (e) in $z < 0.4H_\mathrm{S}$. Targets A-a and B have a radial velocity spread that corresponds to the forward motion of legs or crutches. In contrast, the radial velocity spread of target C-a is small because of the constant speed of the wheelchair. Thus, the standard deviation of the radial velocity distribution can effectively be used to classify target groups C and A or B. The standard deviation of the radial velocity distribution in the low z region is determined by:

$$\sigma_\mathrm{L} = \mathrm{Std}[v_\mathrm{d} \mid z_\mathrm{s} < \alpha_\mathrm{L} H_\mathrm{S}], \qquad (4.4)$$

where $\mathrm{Std}[X \mid C_1, C_2, \cdots]$ is the standard deviation determined by $\{\mathrm{E}[X^2 \mid C_1, C_2, \cdots] - (\mathrm{E}[X \mid C_1, C_2, \cdots])^2\}^{1/2}$. Next, let us consider the classification of target groups A and B. As seen in Fig. 4.2(d), target group B has an approximately symmetrical distribution with respect to the z-axis near the floor. In contrast, the targets in group A have asymmetric distributions to the z-axis corresponding to the asymmetrical motion of legs in half a walking cycle. Figs. 4.5(b) and (c) show the radial velocity distributions in Figs. 4.2(a) and (d) for $z < 0.4H_\mathrm{S}$ and $x < x_\mathrm{cL} - 0.1W_\mathrm{L}$ or $x > x_\mathrm{cL} + 0.1W_\mathrm{L}$. The region near the x_cH is excluded because the properties of the left and right sides of the estimated image are mixed. As we can see from these figures, there is a difference between the averages of both distributions for target A-a, while target group B does not have any difference between the distributions of both regions. Thus, we use the average difference for both regions, which is expressed as:

$$\Delta\mu_\mathrm{L} =\mid \mathrm{E}[v_\mathrm{d} \mid x_\mathrm{s} > x_\mathrm{cL} + \beta W_\mathrm{L}, z_\mathrm{s} < \alpha_\mathrm{L} H_\mathrm{S}]$$
$$- \mathrm{E}[v_\mathrm{d} \mid x_\mathrm{s} < x_\mathrm{cL} - \beta W_\mathrm{L}, z_\mathrm{s} < \alpha_\mathrm{L} H_\mathrm{S})] \mid, \qquad (4.5)$$

where $\beta < 1$ is the threshold ratio of x to the mean width of the silhouette.

Next, we discuss the classification of gait types in target group A. The difference in arm movements in Figs. 4.2(a), (b), and (c) is detected from estimated images that correspond to the upper parts of the body. Fig. 4.5(d) shows the radial velocity distributions in Figs. 4.2(a), (b), and (c) for $z > 0.6H_\mathrm{S}$. As we can see from this figure, the standard deviation of the radial velocity in the high z region is an effective parameter, which is estimated as:

$$\sigma_\mathrm{H} = \mathrm{Std}[v_\mathrm{d} \mid z_\mathrm{s} > \alpha_\mathrm{H} H_\mathrm{S}]. \qquad (4.6)$$

The asymmetry between motion in the left and right arms is an important feature of target A-b. Figs. 4.5(e) and (f) show the radial velocity distributions for $z > 0.6H_\mathrm{S}$ and

$x < x_{\mathrm{cH}} - 0.1W_{\mathrm{H}}$ or $x > x_{\mathrm{cH}} + 0.1W_{\mathrm{H}}$. Similar to Eq. (4.5), the difference in the average in the high z region is expressed as:

$$
\begin{aligned}
\Delta\mu_{\mathrm{H}} =& \mid \mathrm{E}[v_{\mathrm{d}} \mid x_{\mathrm{s}} > x_{\mathrm{cH}} + \beta W_{\mathrm{H}}, z_{\mathrm{s}} > \alpha_{\mathrm{H}} H_{\mathrm{S}}] \\
& - \mathrm{E}[v_{\mathrm{d}} \mid x_{\mathrm{s}} < x_{\mathrm{cH}} - \beta W_{\mathrm{H}}, z_{\mathrm{s}} > \alpha_{\mathrm{H}} H_{\mathrm{S}}] \mid .
\end{aligned}
\tag{4.7}
$$

In addition, there is a difference in the standard deviation of both regions in target A-b, which is extracted by:

$$
\begin{aligned}
\Delta\sigma_{\mathrm{H}} =& \mid \mathrm{Std}[v_{\mathrm{d}} \mid x_{\mathrm{s}} > x_{\mathrm{cH}} + \beta W_{\mathrm{H}}, z_{\mathrm{s}} > \alpha_{\mathrm{H}} H_{\mathrm{S}}] \\
& - \mathrm{Std}[v_{\mathrm{d}} \mid x_{\mathrm{s}} < x_{\mathrm{cH}} - \beta W_{\mathrm{H}}, z_{\mathrm{s}} > \alpha_{\mathrm{H}} H_{\mathrm{S}}] \mid .
\end{aligned}
\tag{4.8}
$$

Targets A-a, -b, and -c are classified with these parameters. Moreover, the target C-b and others are classified with height H_{S}. Based on the above, we propose a feature vector that is expressed as:

$$
\psi = (\sigma_{\mathrm{L}}, \Delta\mu_{\mathrm{L}}, \sigma_{\mathrm{H}}, \Delta\mu_{\mathrm{H}}, \Delta\sigma_{\mathrm{H}}, H_{\mathrm{S}}).
\tag{4.9}
$$

4.4 Classification Using the k-Nearest Neighbor Algorithm

We classified targets using the proposed feature vector extracted from the experimental results, which is explained in this section. We also explain the classification procedure. We evaluated the rate of accuracy in classification from the viewpoint of the three groups and the six types of classifications. The experimental setup and parameters were the same as those in Section 4.2. The parameters for the process to extract the silhouettes were the same as those in Section 4.3.1. The threshold parameters for radial velocity distributions α_{L}, α_{H}, and β were empirically determined as 0.4, 0.6, and 0.1. We assumed four subjects, and their parameters are listed in Table 4.1. Fig. 4.6 and Table 4.2 show examples of relationships between the proposed feature parameters extracted from the data for these subjects and the mean values of these parameters, respectively. We can see clear diversity between the types of pedestrians. Fig. 4.6(a) shows there are clear boundary between Target group A or B and C, and (b) shows the clear difference of Targets in group A. (c) and (d) of this figure also indicate that Targets B, C-a and -b can be separated with the proposed feature parameters.

The types of pedestrians with the extracted feature parameters were classified with the k-NN algorithm. As explained in Section 1.3.3, the k-NN algorithm is suitable for classifying multi-classes with simple boundary [127, 128]. Thus, this algorithm may be suitable for the proposed feature parameters because of their clear boundary. The procedure for classification involves three steps:

1. Prepare the training data set, ψ_{tr}.
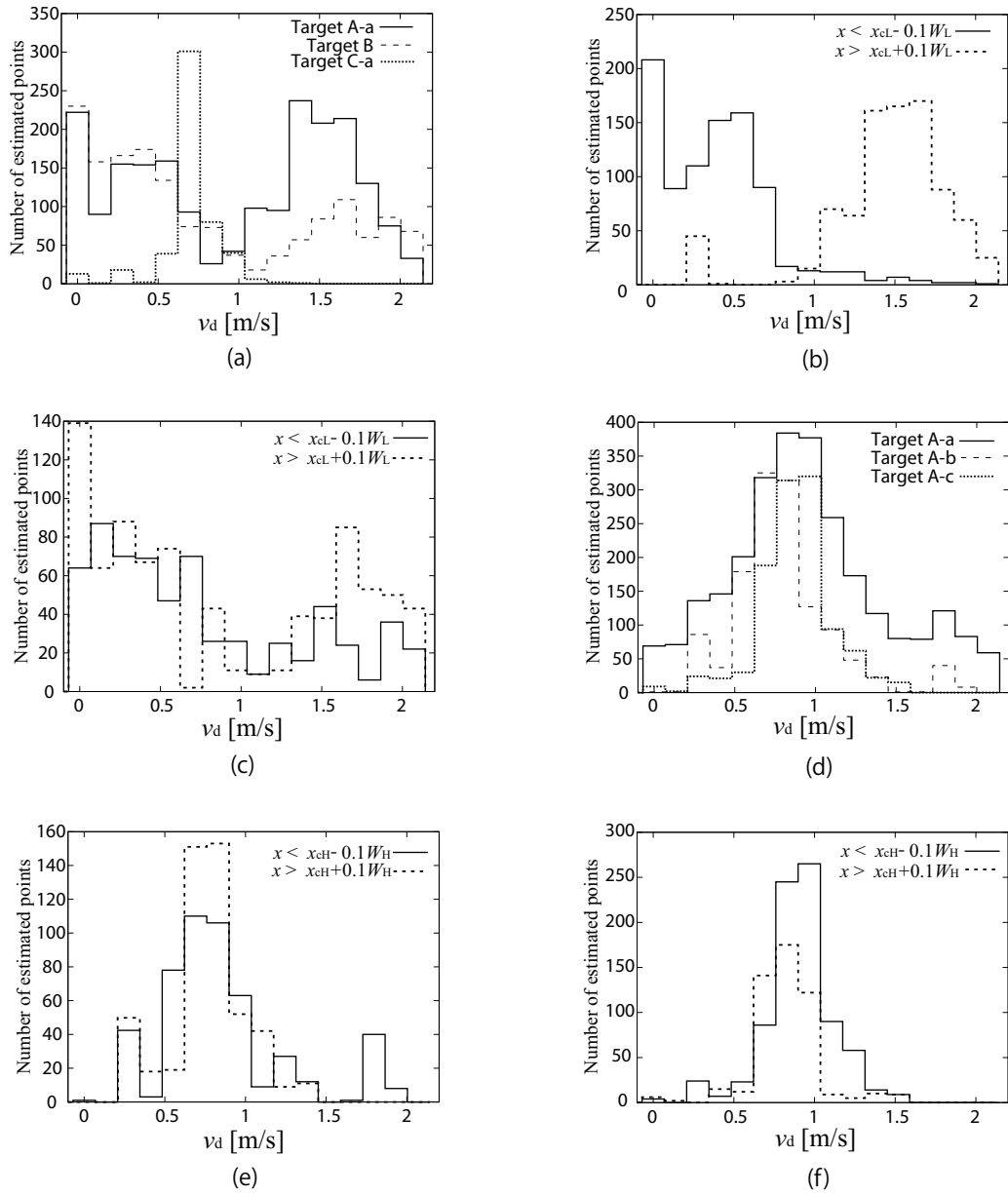
Figure 4.5: Radial velocity distributions of the estimated images shown as Fig. 4.2 in various regions. (a) Target A-a, B and C-a in $z < 0.4H_\mathrm{S}$, (b) Target A-a in $z < 0.4H_\mathrm{S}$, and $x < x_\mathrm{cL} - 0.1W_\mathrm{L}$ or $x > x_\mathrm{cL} + 0.1W_\mathrm{L}$, (c) Target B in $z < 0.4H_\mathrm{S}$, and $x < x_\mathrm{cL} - 0.1W_\mathrm{L}$ or $x > x_\mathrm{cL} + 0.1W_\mathrm{L}$, (d) Target A-a, -b and -c in $z > 0.6H_\mathrm{S}$, (e) Target A-b in $z > 0.6H_\mathrm{S}$, and $x < x_\mathrm{cH} - 0.1W_\mathrm{H}$ or $x > x_\mathrm{cH} + 0.1W_\mathrm{H}$, and (f) Target A-c in $z > 0.6H_\mathrm{S}$, and $x < x_\mathrm{cH} - 0.1W_\mathrm{H}$ or $x > x_\mathrm{cH} + 0.1W_\mathrm{H}$.

Table 4.1: Parameters of subjects.

Subject number	Height [m]	Mean speed [m/s]	Number of data for each pedestrian type
(i)	1.75	0.83	20
(ii)	1.72	0.78	15
(iii)	1.70	0.86	15
(iv)	1.63	0.74	20

Black: A–a (Normal) Red: A–b (Bag) Green: A–c (Pocket)
Blue: B (Crutch) Aqua: C–a (Pushing wheelchair) Purple: C–b (Driving wheelchair)
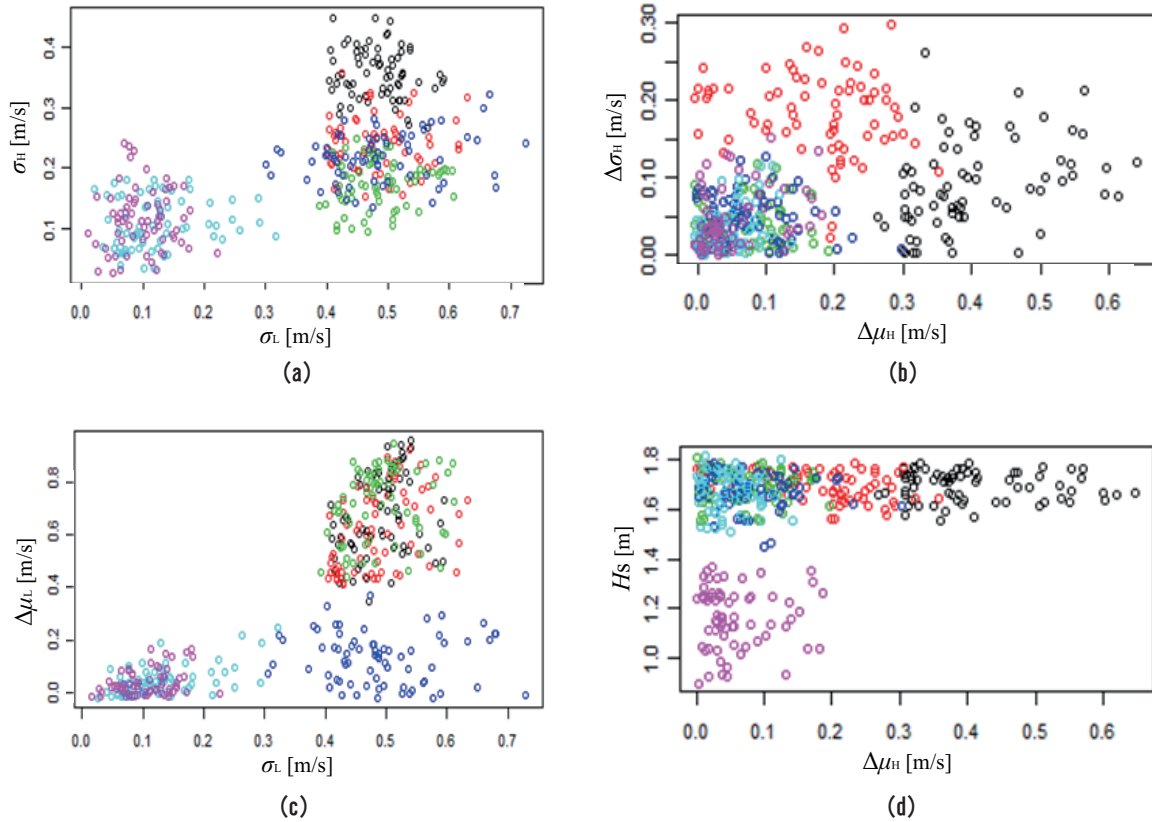
Figure 4.6: Estimation results of proposed feature paramters with experimental data for all subjects in Table 4.1.

Table 4.2: Mean values of proposed feature parameters.

	σ_{L}	$\Delta\mu_{\mathrm{L}}$	σ_{H}	$\Delta\mu_{\mathrm{H}}$	$\Delta\sigma_{\mathrm{H}}$	H_{S}
A-a	0.489	0.643	0.357	0.407	0.0912	1.69
A-b	0.486	0.530	0.238	0.179	0.184	1.70
A-c	0.491	0.677	0.175	0.0736	0.0408	1.69
B	0.489	0.138	0.218	0.0820	0.0507	1.67
C-a	0.127	0.0590	0.108	0.0508	0.0334	1.67
C-b	0.104	0.0518	0.116	0.0557	0.0449	1.16

2. Calculate the Euclidean distance between an unlabeled feature vector, ψ, and all ψ_{tr}.

3. Classify ψ to the label which most frequently appear in k training vectors nearest to ψ.

We set the data of subject (i) to ψ_{tr}, and k=3. How k was set and the number of training data were determined are discussed in the next section. Table 4.3 shows the confusion matrix for the classification results for subjects (ii)–(iv). Although there is slight mis-classification of targets A-a, -b, and -c, accurate classification is generally achieved. The rate of classification accuracy for the six types is 96.0 %. Moreover, the rate of classification accuracy is 99.3 % with respect to classification of the three groups. The input time duration of each set of data is less than 0.8 s, and the average of the total calculation time for the imaging and classification processes is 0.55 s using an Intel Core 2 Duo 3.33-GHz processor. These results mean that our proposed feature parameters and classification procedures could accurately classify pedestrians in real-time.

4.5 Discussion

4.5.1 Evaluation of Performance for Quantity of Training Data and Comparison with Other Classifiers

This subsection discusses our investigations into the performance of our proposed method of classification with respect to the quantity of training data. Moreover, we compared the k-NN algorithm with other representative classifiers explained in Section 1.3.3: a support vector machine (SVM) and a naive Baysian classifer (NBC). This section uses a soft-margin multi-class SVM with a Gaussian kernel function and a one-versus-one approach [124]. We investigated the rate of classification accuracy with 1- and 3-NN algorithms and SVM for the ratio of the quantity of training data to all data. The

Table 4.3: Confusion matrix. AT represents the actual type, and ET represents the type estimated by the 3-NN algorithm.

AT \ ET	A-a	A-b	A-c	B	C-a	C-b
A-a	46	4	0	0	0	0
A-b	3	44	3	0	0	0
A-c	0	0	49	1	0	0
B	0	0	0	50	0	0
C-a	0	0	0	1	49	0
C-b	0	0	0	0	0	50

experimental setting, parameters, and the data used were the same as those presented in the previous section, and the training data set was randomly selected.

Figs. 4.7 and 4.8 plot the relationships between the rate of classification accuracy and the quantity of training data to classify the six types and three groups, where N_{train} and N_{all} correspond to the quantity of training and all data. As seen in this figure, the k-NN and NBC algorithms classify more accurately than SVM, and 3-NN is better than 1-NN when the quantity of training data is relatively large. The 3-NN algorithm achieves 99 % accuracy in classifying the three groups when $N_{\text{train}}/N_{\text{all}}$ is larger than 15 %, and 95 % accuracy in classifying the six types when $N_{\text{train}}/N_{\text{all}}$ is greater than 20 %. The NBC also realizes accurate classification with almost same accuracy of the 3-NN. However, the calculation time is relatively large. When $N_{\text{train}}/N_{\text{all}}$ is 20 %, the mean calculation time of NBC and 3-NN are 0.77 s and 0.08 s, respectively. These results mean that the 3-NN algorithm can classify the pedestrian targets accurately and rapidly with a relatively small quantity of training data.

Additionally, an important property of the proposed classification algorithm is that almost same accuracy rate is realized with different training data. For the classification of Table 4.3, the training data set is the data of subject (i) and $N_{\text{train}}/N_{\text{all}}$ is 28.6 %. As shown in Figs. 4.7 and 4.8, almost same classification rate is realized with approximately $N_{\text{train}}/N_{\text{all}} = 30$ %, although these examples randomly selected the training data. This discussion indicates that the the proposed algorithm can realize accurate classification with training data set extracted from data of arbitrary one subject. This is an important characteristics in practice.

4.5.2   Assessment of Suitable Parameters

This subsection discusses the parameters we used with our proposed method. First, let us explain how we set spatial threshold parameters α_{L}, α_{H}, and β. Here, we present $\Delta\mu_{\text{L}}$ of targets A-a and B for each α_{L} as an example. Fig. 4.9 plots the relationship between α_{L} and the mean value of $\Delta\mu_{\text{L}}$. The difference between the target types is relatively large for
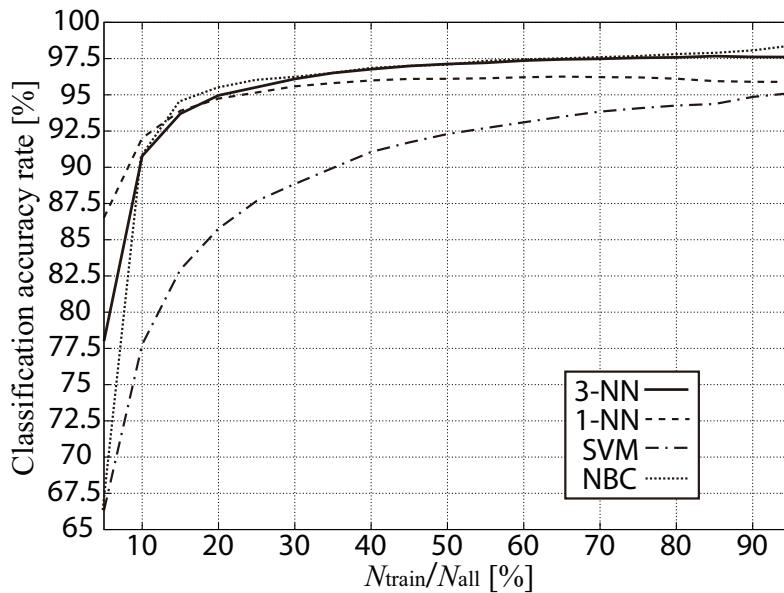
Figure 4.7: Classification accuracy rate of the six types versus the quantity of training data.

$0.25 < \alpha_{\mathrm{L}} < 0.5$. Other parameters can be set similarly. Therefore, we can easily choose appropriate parameters based on a few examples.

We will next discuss k of the k-NN algorithm. Fig. 4.10 plots the relationship between k and the rate of classification accuracy for the six types. The value of $k = 1$ or 3 was better. In addition, $k = 3$ was better when the quantity of training data was relatively large. Accuracy deteriorated when k was an even number. This is because the k-NN algorithm randomly selected a label when the number of classes was the same.

4.5.3 Discussion on Variety of Motions

This subsection will discuss the possibility of classifying other types of targets such as a person carrying a box on a hand cart, a short person, a person making other movements, and a person moving in oblique directions. The main characteristic of a target pushing a hand cart is almost the same as that of target C-a, and the classification of normal pedestrians and those on crutches is possible using σ_{L} and σ_{H}. Although target C-b and others can be classified with H_{S}, it is difficult to classify a short person such as a child with only this parameter. However, if the short person makes leg or arm movements, classification using σ_{L} and σ_{H} is possible. Furthermore, it is plausible to classify a variety of motion types (e.g. running, sitting, rotating, and jumping [87]). We can easily predict that the differences in these motion types will clearly be extracted as velocity and silhouette parameters. For a person walking in oblique direction, human outline and walking features can be estimated as shown in Sections. 2.4 and 3.4.4. In addition, feature detection of

94
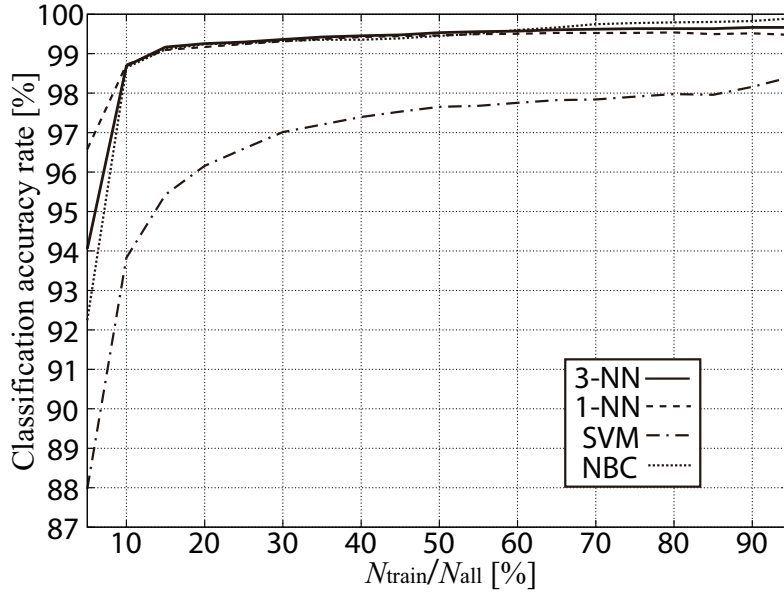
Figure 4.8: Classification accuracy rate of three groups versus the quantity of training data.

Target B becomes easy because the velocity difference between crutches also becomes large. Consequently, the proposed classification algorithm may be able to apply to the targets moving in oblique directions.

4.6 Conclusions

This chapter presented an accurate and real-time algorithm of classifying pedestrians. We first demonstrated that accurate imaging could be accomplished with the UWB Doppler radar interferometric imaging algorithm for a variety of pedestrian targets, and discussed the features of each target. Then, effective feature parameters based on UWB Doppler radar images and their radial velocity features were proposed. The experiments took into consideration six types of pedestrians (those with both arm-swing, having a bag and swinging one arm, and no-arm motion, those on crutches and in wheelchairs, and a person propelling himself in a wheelchair) and we found that they were classified with an accuracy of 96 % by using the 3-NN algorithm. The total calculation time for the imaging and classification processes was 0.55 s. Moreover, we revealed that the proposed algorithm can realize accurate classification with the training data set which is extracted from data of arbitrary one subject. In addition, an accuracy of 99 % was accomplished in classifying the three groups (normal pedestrians, those on crutches and both wheelchair groups). The performance comparison with other classifiers indicated that 3-NN algorithm is an appropriate algorithm for the classification using the proposed feature parameters with
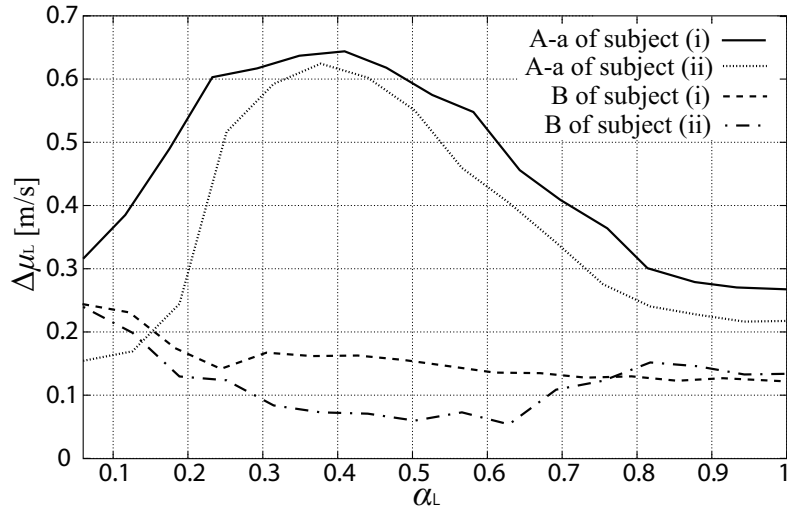
Figure 4.9: Relationship between α_L and $\Delta\mu_\mathrm{L}$ for targets A-a and B.
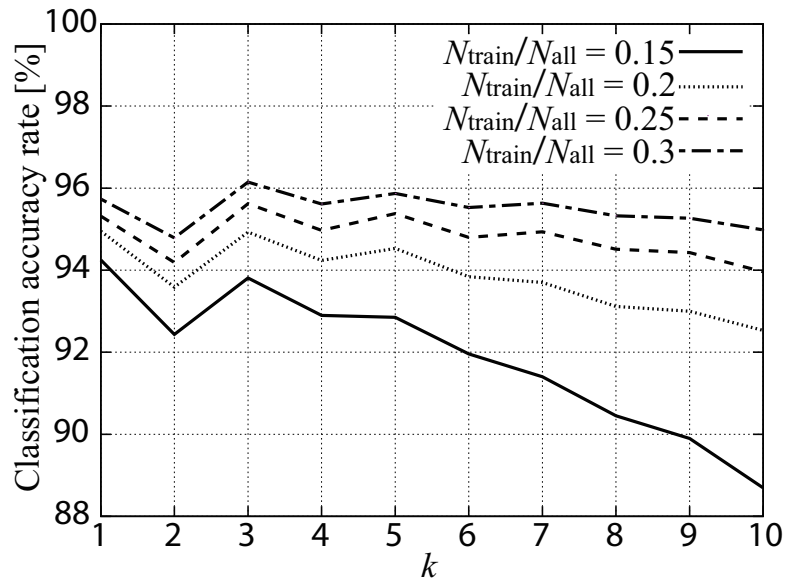
Figure 4.10: Relationship between k and the classification accuracy rate of the six types.

respect to both accuracy and calculation time. Furthermore, we clarified how well the method performed, found suitable parameter settings for the proposed algorithm, and discussed capabilities in classifying other types of targets.

Chapter 5

Image Separation Algorithm for Two Closely Spaced Pedestrians

5.1   Introduction

Although a large number of studies have focused on developing human identification techniques for monitoring systems using micro-Doppler radars, as described in Chapter 1, most of these conventional methods were designed for a solitary target or targets sufficiently well spaced. Several researchers proposed methods to classify whether one or two people are detected [91]. However, their classification accuracy is inadequate and identification of each person is impossible.

   This chapter proposes a solution to these problems with a separation algorithm for two closely spaced pedestrian targets using high-resolution images acquired using UWB Doppler radar interferometry. First, an imaging example of pedestrians and a simple image separation method using range profiles are introduced. This method is applied experimentally to a group image estimated by the proposed UWB Doppler radar imaging algorithm and shows that the separation accuracy of closely spaced pedestrians is unsatisfactory. To solve this problem, an accurate separation algorithm for the targets in the image using a support vector machine (SVM) is proposed. As explained in Section 1.3.3, the SVM is one of effective discriminant analyses capable of determining non-linear separating hyperplane [123]. The proposed algorithm uses a training data set extracted from range profiles. Finally, false points caused by target interference are rejected based on the separation results. An experiment, which assumes two closely spaced pedestrian targets, shows that the proposed algorithm achieves accurate separation and identification of their images. Moreover, applications with various target positions are described, their performance established, comparison with other classifiers carried out, and optimal settings of the proposed separation algorithm derived.

Figure 5.1: Experimental setup with two pedestrian targets.

5.2 Imaging of Two Closely Spaced Pedestrians

This section describes an experimental setup and imaging result of two pedestrian targets. Fig. 5.1 shows a photograph of the setup. The setup and parameters of the radar and proposed UWB Doppler radar imaging algorithm are the same as in the previous chapters. Two pedestrians walk in phase simultaneously with a gait cycle of 1.25 s and an average speed of 0.96 m/s. Target 1, 1.63 m tall, walks from (x, y)=(0.25 m, 3.9 m) to (0.25 m, 1.5 m), while Target 2, 1.75 m tall, walks from (x, y)=(-0.2 m, 4.35 m) to (-0.2 m, 1.95 m). The separation of their torsos is approximately 0.44 m. This is a relatively difficult task for conventional UWB Doppler radar imaging techniques because the separation of the targets has an insufficient value with a nominal range resolution of 0.3 m. In this setup, the echoes from many parts of the body of both targets are mixed in the same range bin (e.g. the right arm of Target 1 and the left arm of Target 2). In addition, they walk in phase and in the same direction, which is a relatively tough situation to analyze because the Doppler radar separates targets based on the difference in their motions.

Fig. 5.2 shows the time-variation of the range profile for Rx_1 at z_c= 0.36 m. Strong echoes are obtained for $t > 1.7$ s. From these echoes it is verified that both targets are walking at an approximately constant speed towards the antennas. Fig. 5.3 shows the summation of the spectrograms for ranges corresponding to Fig. 5.2. The radial velocity offset corresponding to the walking speed and the micro-Doppler signatures of the leg motion are observed. Fig. 5.4 shows a top view of the imaging result. Here, the data for $t > 1.7$ s are used because of high signal-to-noise ratio. The scattering centers corresponding to both targets are confirmed. Next, the problem of determining which target each scattering center belongs to is considered.

98
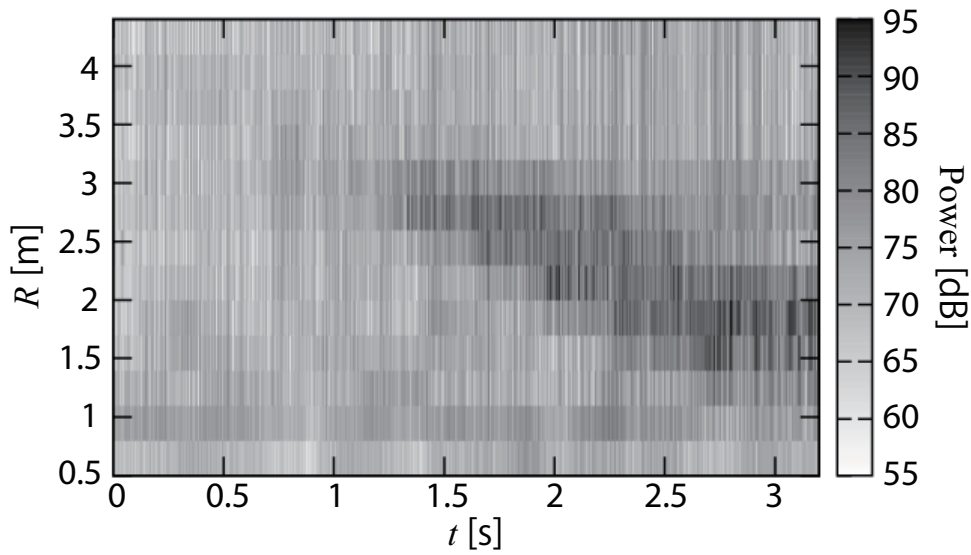
Figure 5.2: Time-variation of range profile for Rx_1 at $z_c = 0.36$ m.
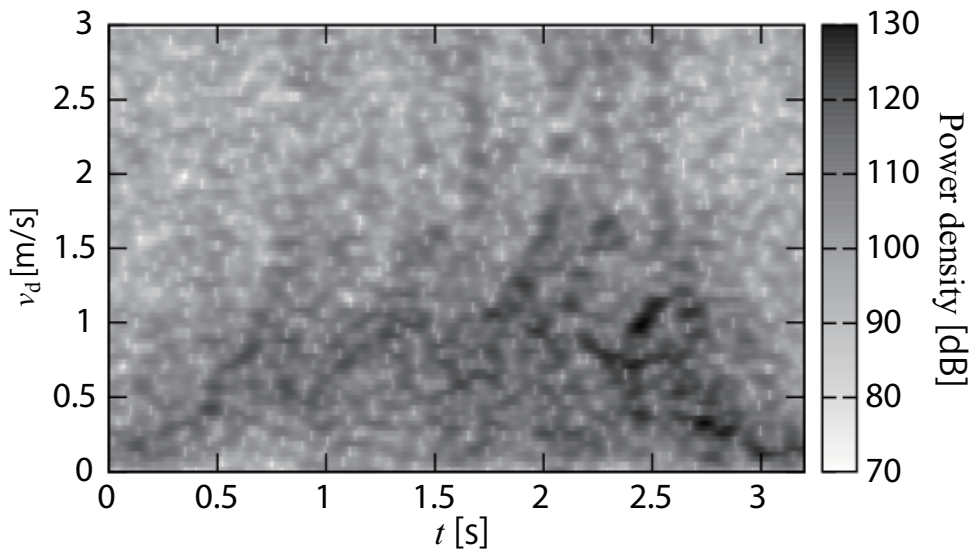
Figure 5.3: Summation of spectrograms for range from Rx_1 at $z_c = 0.36$ m.

5.3   Simple Image Separation Method

This section introduces a simple image separation method for two targets, and confirms its performance in an experiment. In this method, the estimated scattering centers are

99
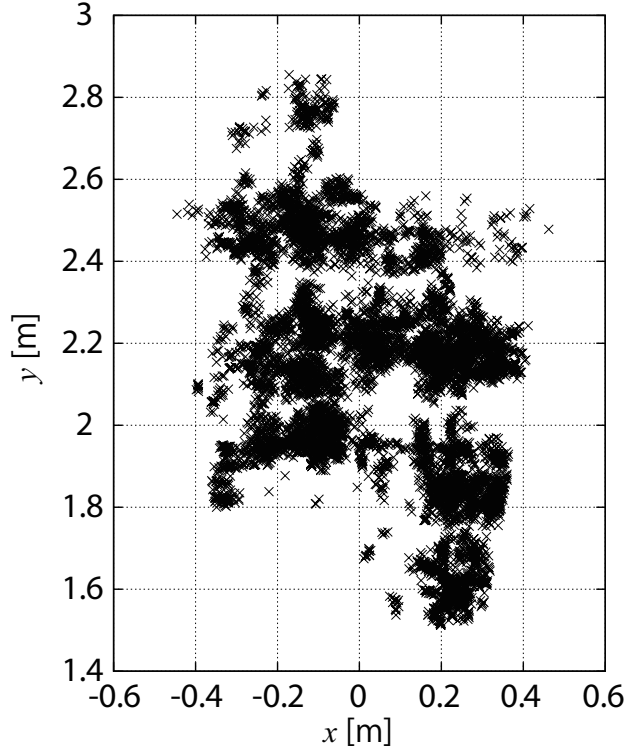
Figure 5.4: Top view of the estimated image of two closely spaced pedestrians.

separated by identifying a delimiting boundary between the two targets. The delimiting boundary is extracted as the power-weighted mean of the range profile for each time bin, which is expressed as:

$$B(t) = \sum_{j}^{N_{\mathrm{R}}} j\Delta R |s_{1j}(t)|^2 (j\Delta R)^4 \Big/ \sum_{j}^{N_{\mathrm{R}}} |s_{1j}(t)|^2 (j\Delta R)^4, \qquad (5.1)$$

where N_{R} is the number of range bins. A target label (Target 1 or 2) for each estimated scattering center $\mathbf{x}_{\mathrm{s}}(t, v_{\mathrm{d}n})$ is determined by comparison with $B(t)$ and the range $R(t, v_{\mathrm{d}n})$ as:

$$\mathrm{label}\{\mathbf{x}_{\mathrm{s}}(t, v_{\mathrm{d}n})\} = \begin{cases} 1 & (R(t, v_{\mathrm{d}n}) \leq B(t)) \\ 2 & (R(t, v_{\mathrm{d}n}) > B(t)). \end{cases} \qquad (5.2)$$

Fig. 5.5 shows the top view of the separation result of Fig. 5.4 using Eq. (5.1). Many separation errors are obtained because the range difference between the targets is too small compared with ΔR. Fig. 5.6 shows the front views of images separated by the simple separation method for 1.76 s $< t <$ 2.39 s, corresponding to a single stride, or half a walking cycle. Although human features are to a certain degree discernible, the extraction of a human target is difficult because of many separation errors. Thus, a better separation method for closely spaced pedestrians is needed to achieve greater accuracy.

100
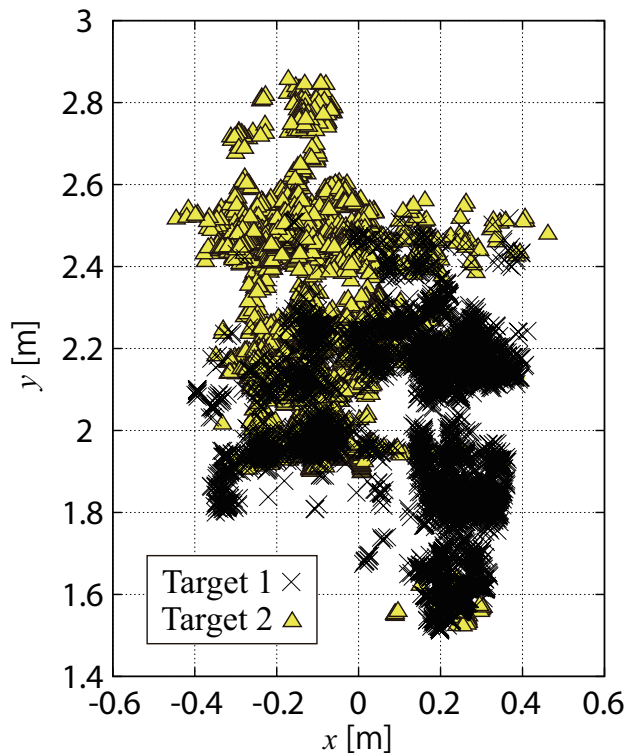
Figure 5.5: Top view of the image separation result using the simple method.

5.4   Proposed Image Separation Algorithm

5.4.1   Training Data Acquisition

To accomplish accurate separation of two adjacent pedestrians, an image separation method using the SVM is then proposed. The SVM is a accurate classifier developed to create non-linear separation boundary by applying the kernel technique (described in Section 1.3.3) [123, 124]. The proposed algorithm determines the separation boundary of the estimated scattering centers using a training data set acquired from the estimated scattering centers based on range profiles. Fig. 5.7 sshows an example of a range profile when two peaks are confirmed; these peaks mainly correspond to the echoes from the torso of each target. The data between these peaks correspond to the interference between the targets. Nevertheless, data on either side of these peaks can be regarded as echoes from one or other target.

Based on the above consideration, training data are extracted at scattering centers that exist around the peaks in the range profile. First, the two peaks of the range profile are extracted for each time bin t. Here, if two peaks cannot be acquired, training data are not extracted in this time t. Next, it is assumed that the reflected signal from each target

(a) Target 1   (b) Target 2
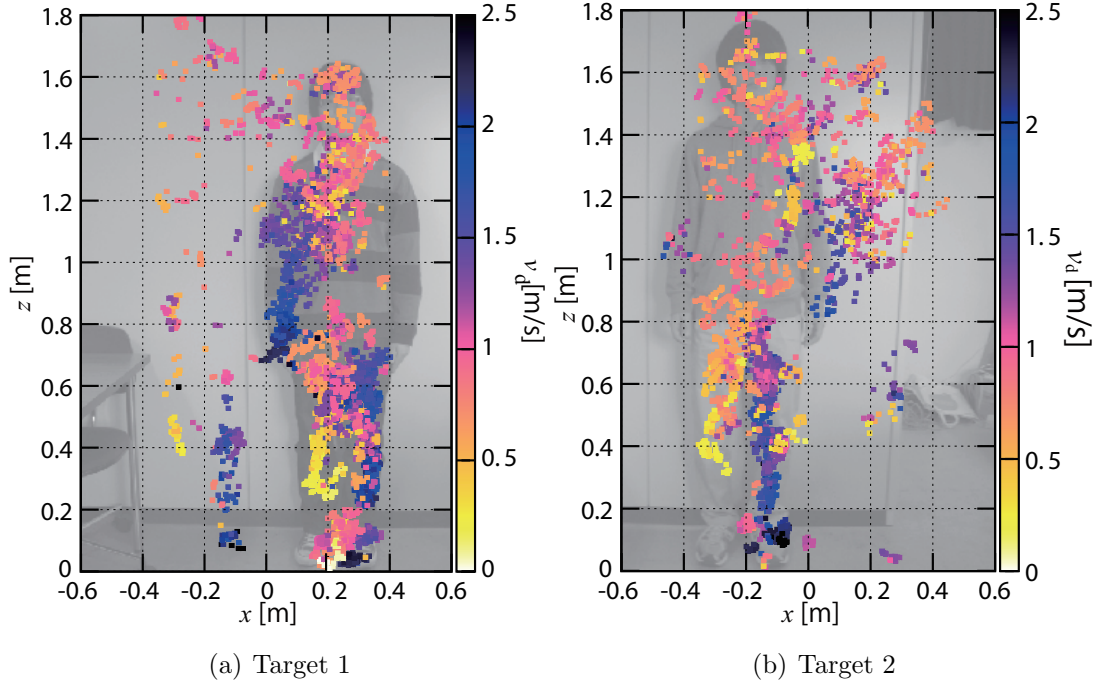
Figure 5.6: Frontal view of the image separated by the simple method.

is a Gaussian function, and signals shown in Fig. 5.7 are estimated using each peak and two adjacent range gates around the peak. The estimated signal at t corresponding to Targets 1 and 2 are denoted as $G_{1t}(R)$ and $G_{2t}(R)$, and the maximum powers of $G_{1t}(R)$ and $G_{2t}(R)$ are denoted as P_{1t} and P_{2t}. A threshold is set for the acquisition of training data for Target 1 as the range for which $G_{1t}(R) = \alpha P_{1t}$ hold, where $0 < \alpha < 1$ is a constant. Consequently, the range threshold for Target 1 is determined from:

$$B_1(t) = \min\left(G_{1t}^{-1}(\alpha P_{1t})\right), \tag{5.3}$$

where G_{1t}^{-1} is the inverse function of G_{1t} and $\min(\cdot)$ is a function returning the minimum value. With $B_1(t)$, scattering center information is extracted for the training data of Target 1 that satisfy the condition:

$$R(t, v_{\mathrm{d}n}) < B_1(t). \tag{5.4}$$

Similarly, the threshold for Target 2 is determined by:

$$B_2(t) = \max\left(G_{2t}^{-1}(\alpha P_{2t})\right), \tag{5.5}$$

and the condition for training data extraction for Target 2 is:

$$R(t, v_{\mathrm{d}n}) > B_2(t). \tag{5.6}$$
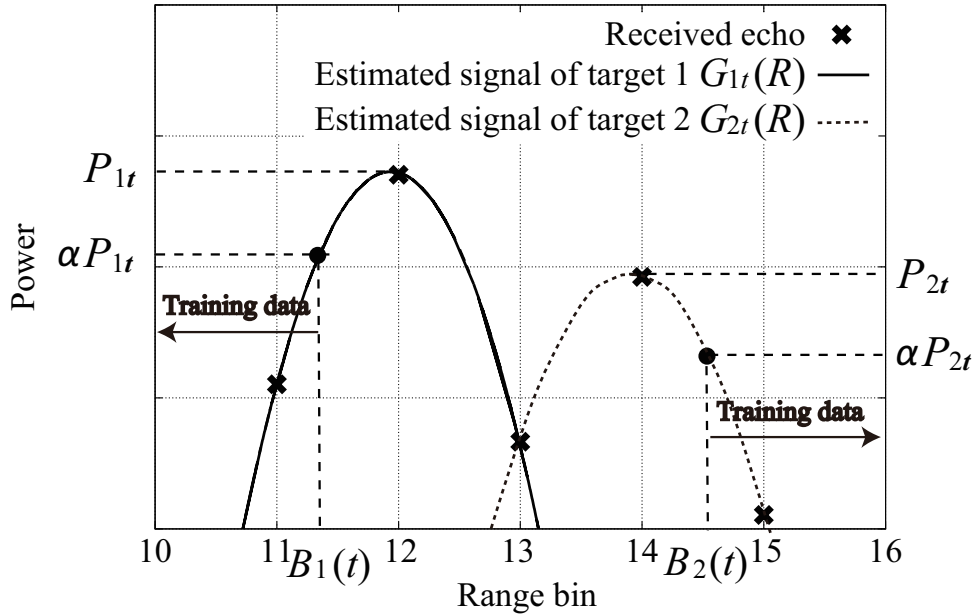
Figure 5.7: An example of a range profile and threshold for training data acquisition.

Fig. 5.8 shows the acquired training data from the data of Fig. 5.5. Since the number of time bins which can extract two peaks is limited, the amount of training data is small compared with the amount of estimated data. In this case, the ratio of the quantity of the training data to other data is 1.0 %.

5.4.2 Image Separation and False Point Rejection

Next, details of the SVM process are explained. A separation boundary is determined by the SVM from the estimated scattering centers selected as the training data at each time interval. The method in this study uses the Gauss kernel function, which is known as a general-purpose function for the SVM [123]. The SVM parameters are set by a grid search using the two-fold cross-validation approach [124]. Using the determined separation boundary, the target label is identified for each estimated scattering center except for the training data. The separation is conducted in the xyt space. This is because pedestrian targets are assumed where the height differences (z-axis direction) between the targets are not clear. These separation processes, including training data acquisition, are conducted for a certain time interval T_{in}. In this study, T_{in} is set based on the gate cycle of the targets.

Image separation is achieved from the above process. However, because of interference between targets, many false points that do not belong to either target remain near the separation boundary. Based on the separation result of the SVM, the proposed method finally removes these false points. First, a sphere centered at $\mathbf{x}_s(t, v_{dn})$ with a radius of r_b
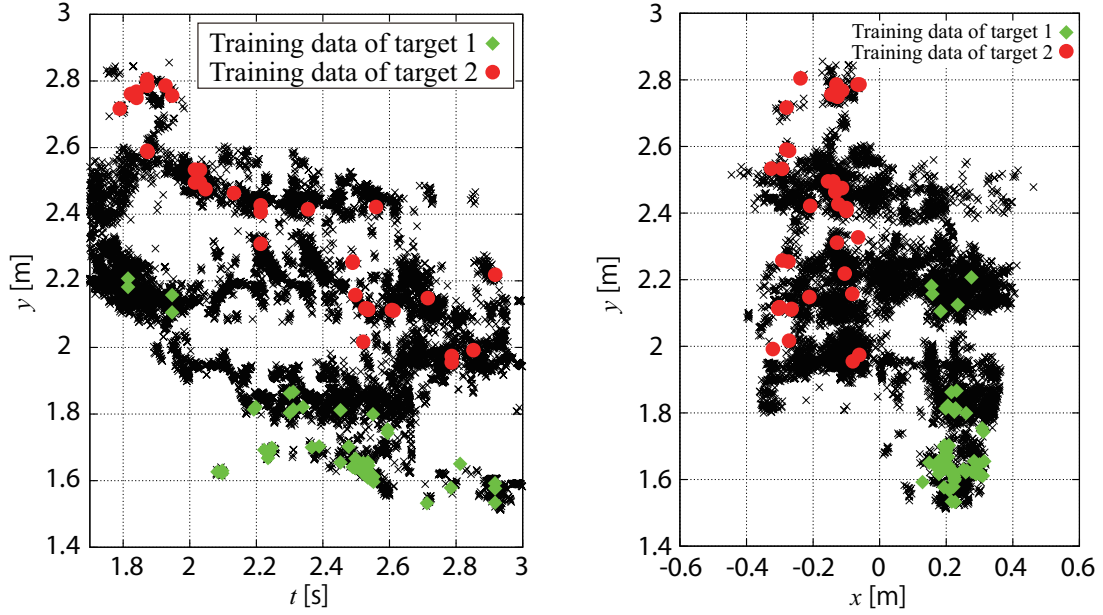
Figure 5.8: Top view and ty plane of the estimated image and acquired training data.

in the $xyt_{\mathrm{w}l}$ space is assumed, where $t_{\mathrm{w}l} = tv_{\mathrm{w}l}$ and $v_{\mathrm{w}l}$ is the mean radial velocity for the estimated scattering center corresponding to Target l ($l = 1, 2$). Next, the number N_l of scattering centers which belong to each target within the assumed sphere is counted. If it is assumed $\mathbf{x}_{\mathrm{s}}(t, v_{\mathrm{d}n})$ belongs to Target 1, the scattering centers that satisfy the condition $N_1/N_2 < \beta$ as false points are rejected, where $0 < \beta < 1$ is empirically determined. If it is assumed $\mathbf{x}_{\mathrm{s}}(t, v_{\mathrm{d}n})$ belongs to Target 2, the scattering centers that satisfy the condition $N_2/N_1 < \beta$ are rejected in the same way.

The procedure for the proposed image separation algorithm is summarized as:

1. Estimate the scattering centers using data whose length of T_{in}.

2. Obtain a training data set from these scattering centers using only data that can extract two peaks of the range profiles.

3. Determine the separation boundary with SVM using these training data.

4. Conduct separation using the determined boundary and false point rejection.

5. Iterate these steps until the end of the observation data is reached.

Here, the assumed input time duration T_{in} is smaller than 1 s.

5.5 Results and Discussion

5.5.1 Image Separation Example with the Proposed Method

This subsection presents a separation example with the same situation as in Sections 5.2 and 5.3 but using the above-proposed method, and assesses its separation accuracy. The experimental setup and parameters are same as in Section 5.2. Fig. 5.9 shows the top view of the separation result using this new method. The data for $t > 1.5$ s are used, and $\alpha = 0.3$, $r_{\mathrm{b}} = \Delta R/10 = 3$ cm, and $\beta = 0.3$ are set empirically. As shown in this figure, the proposed method achieves accurate separation. Fig. 5.10 shows that for 1.76 s $< t < 2.39$ s, the frontal views of each image are well separated by this method. Although separation errors between targets still remain, outlines of human shapes are observable. We can recognize from the v_{d} information that the left leg and the right arm of both targets are striding forward in this half of the walking cycle. This is a key feature in walking.

Next, the separation accuracy is quantitatively evaluated. A separation error rate is defined using a true separation plane in $xyt_{\mathrm{w}l}$ space. The true separation plane is defined as the central plane between the assumed true orbits of the targets. The true orbit of target l is expressed as $y = -t_{\mathrm{w}l} + y_l$ and $x = x_l$. The true separation plane is defined as:

$$y_{\mathrm{T}}(t_{\mathrm{w}l}, x) = -t_{\mathrm{w}l} - \frac{x_2 - x_1}{y_2 - y_1}x + \frac{y_1 + y_2}{2} \tag{5.7}$$

The number of misclassification points N_{E} using $y_{\mathrm{T}}(t_{\mathrm{w}l}, x)$ are then counted and the separation error rate is defined as

$$\delta = N_{\mathrm{E}}/N_{\mathrm{All}}, \tag{5.8}$$

where N_{All} is the total number of estimated scattering centers. δ of Figs. 5.5 and 5.9 are 18.5 % and 4.87 %. Moreover, when calculated, T_{in} was 0.8 s which is slightly larger than half the walking cycle, and the total calculation time for the training data acquisition and classification processes was 0.33 s using an Intel Core i5-2520M CPU 2.50 GHz processor. These results confirm that the proposed method improves the separation accuracy more than three-fold over the simple method and accomplishes accurate and real-time image separation of two closely spaced pedestrians.

5.5.2 Performance Evaluation for Various Target Positions

In this subsection, the performance of the proposed separation method for various target positions is evaluated. Fig. 5.11 shows the top view of the initial position of the targets. Here, the distance between the targets is $L =67$ cm, and the relative positions are varied by angle θ. The same pedestrian targets as in the previous section are assumed. In all scenarios, the targets walk 2.4 m in a straight line parallel with the y-axis towards the
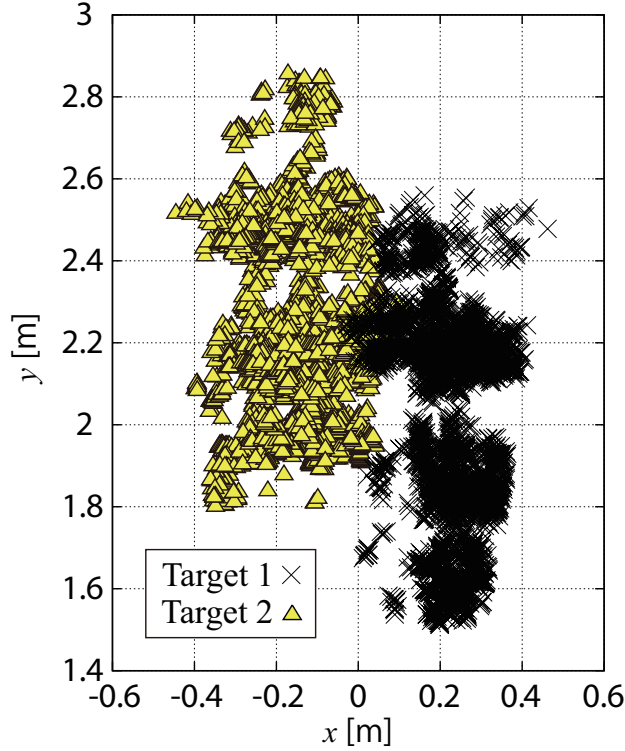
Figure 5.9: Top view of the image separation result with the proposed method.

origin. The parameter α is empirically set for each θ, details of which are discussed in the next section. Other parameters and the experimental setup are the same as described in the previous section.

The relationship between θ and δ obtained from the simple and proposed separation methods, (see Fig. 5.12) shows that the separation accuracy of the proposed method is better for all θ. However, δ becomes comparatively large for $\theta = 0$ and $90°$. When θ is small, the range difference between the targets is also small; therefore the extraction of training data is difficult in this case. When θ is nearly $90°$, Target 2 is obscured by Target 1, and the number of estimated scattering centers for Target 2 decreases greatly. However, with the exception of these cases, the proposed method achieves accurate separation over the interval $10° < \theta < 80°$. These results verify that the proposed separation method works well for various positions of the pedestrians.

5.5.3 Examination of Suitable Parameters α and β

This section investigates suitable settings for the parameters α and β. First, α is discussed. Eqs. (5.3) and (5.5) mean that α determines the threshold of training data acquisition. The separation accuracy depends on the amount of training data. On the one hand, if

(a) Target 1   (b) Target 2
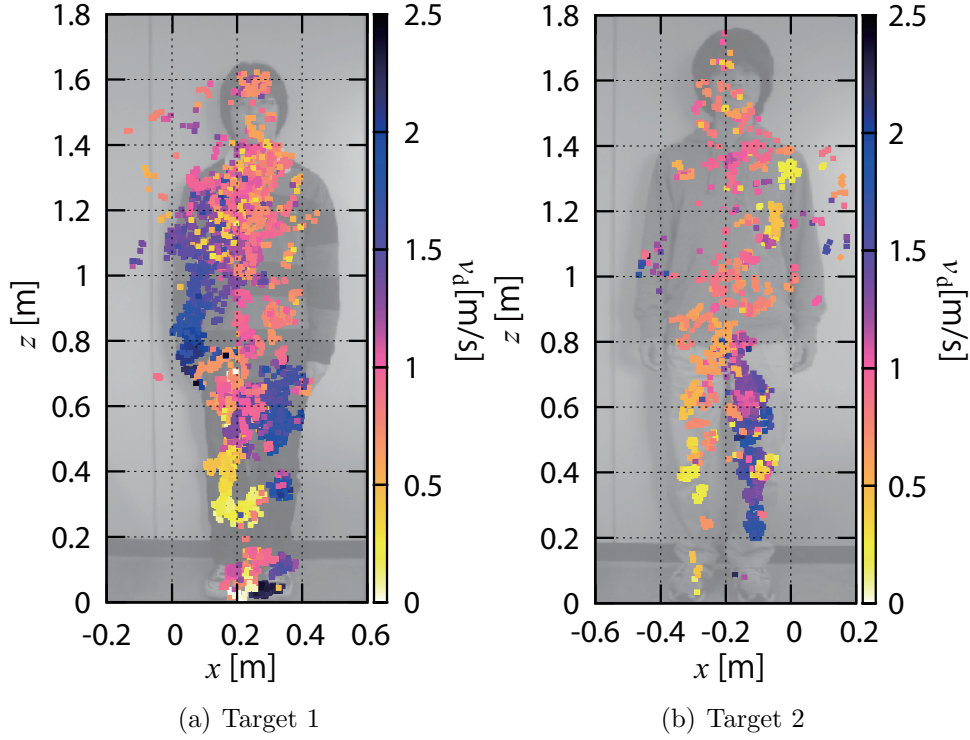
Figure 5.10: Frontal view of the image separated by the proposed method.

a value for α that is too small is set, the amount of training data becomes insufficient. On the other hand, if α is too large, an improper training data set is extracted through interferences from the targets. For these reasons, setting an α value is important for the proposed method. To investigate suitable α, the relationship between α and the separation accuracy for the various target positions assumed in the previous section, is estimated.

The separation error rate δ for each α and θ (see Fig. 5.13), shows that optimum values for α depend on the relative positions of the targets. When θ is small, the appropriate α also needs to be small because there is an increase in the mis-extraction of the training data for larger α. In contrast, the optimum α value can be relatively large for large θ. Sufficiently accurate separation is achieved at $\alpha = 0.3$ for all θ, hence this becomes a suitable setting for a wide range of situations. However, if it is recognized that the range separation between the targets is sufficiently large, the separation accuracy can be improved by setting larger α values. Thus, a suitable α can be chosen to perform a few examples for each situation.

Next, the parameter β, which is the threshold in the false point rejection method, is discussed. If β is too large, too many points are rejected. Conversely, if β is set small,
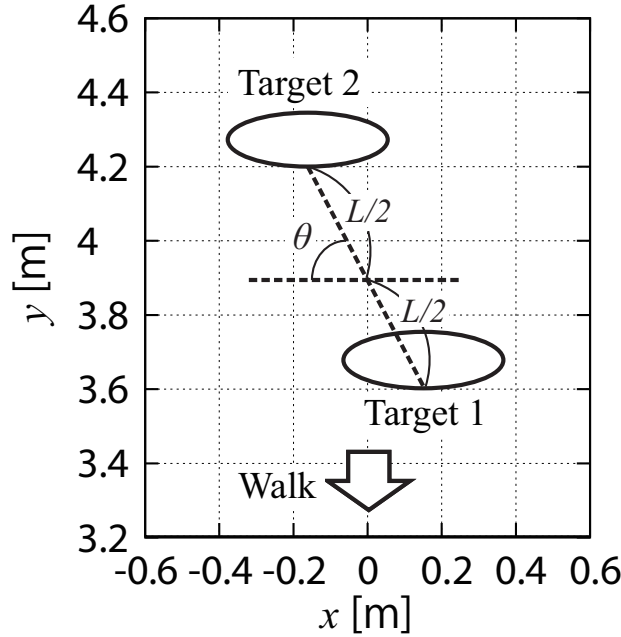
Figure 5.11: Top view of the initial positions of the targets.

many false points near the separation boundary remain. For these reasons, the relationships $\beta - \delta$, and β and the number of rejected points are important for the appropriate setting of β. Fig. 5.14 shows these relationships for $\theta = 47.8°$ and $\alpha = 0.3$. The improvement in the classification accuracy is confirmed when setting a large β. However, the number of rejected points become excessive when $\beta > 0.4$. Moreover, the improvement in δ is relatively small when $\beta > 0.25$. Based on these observations, the interval $0.25 < \beta < 0.35$ is determined as a suitable setting. In addition, the same tendency for the other θ is confirmed.

5.5.4 Performance Comparison with Other Classifiers

Finally, the separation performance is compared with other representative classifiers explained in Section 1.3.3: a k-nearest neighbor (k-NN) and a naive Baysian classifer (NBC). Figs. 5.15 and 5.16 are classification results of 3-NN and NBC algorithms with the same data as in Fig. 5.9. Here, $k = 3$ is a better setting for k-NN in this case. As can be seen from these figures, a large number of separation errors compared with SVM are confirmed for both algorithms. The classification accuracy rate using the 3-NN and NBC are 9.02 and 11.9 %, and these are worse than for the SVM (4.87 %), because the amount of training data is insufficient for these algorithms. k-NN requires a relatively large number of training data near the class boundary, but such data are not acquired as shown in Fig. 5.8. NBC generates many separation errors especially near $(x, y) = (0.2$ m , 2.5 m)
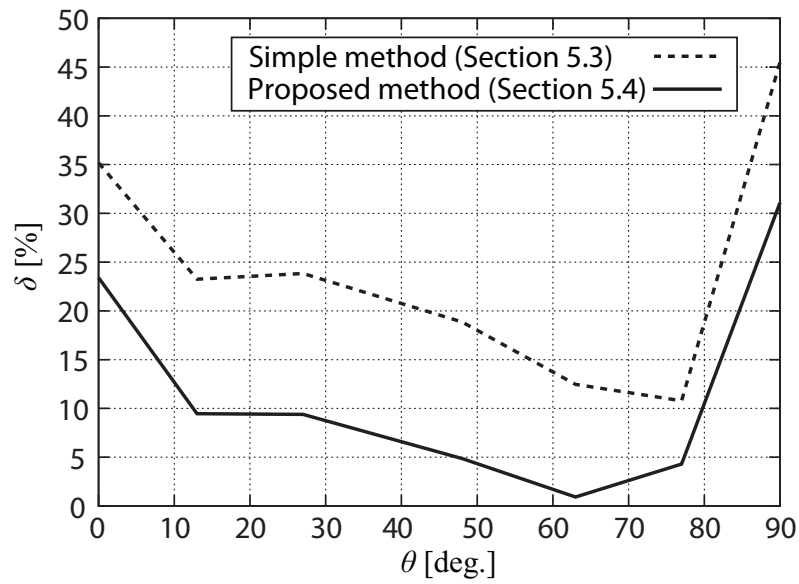
Figure 5.12: Separation error rate for various positions of targets.
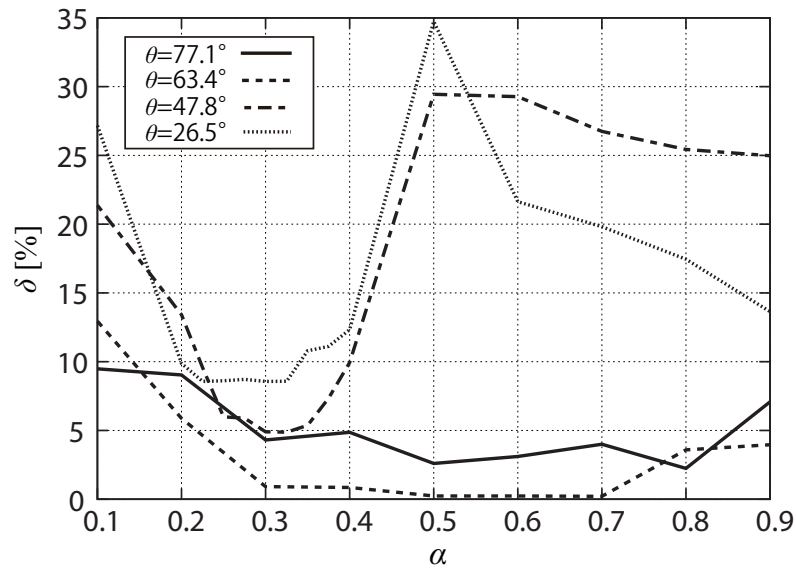
Figure 5.13: Relationship between α and δ.

because it requires training data evenly distributed in the region where the data exist. In contrast, SVM can classify with a small amount of training data near the class boundary because of the perceptron principle. Thus, SVM is the most effective algorithm for the applications assumed in this chapter.
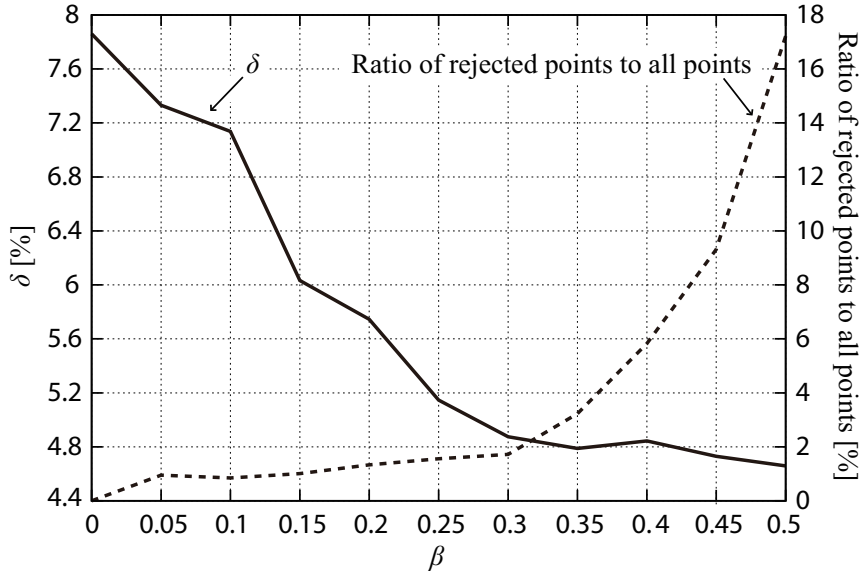
Figure 5.14: Relationship between β, δ, and the ratio of rejected points to all estimated points.

5.6 Conclusions

Based on UWB Doppler radar images, an image separation method for two closely spaced pedestrians has been proposed in this chapter. Its accuracy is demonstrated by its application in realistic environments. First, the simple image separation method is introduced, and the experiment showed that the separation accuracy of adjacent pedestrians was inadequate. To achieve better accuracy, the image separation method using the SVM is proposed. The experiment, involving two pedestrians separated by 0.44 m walking towards the radar, showed that the method achieved image separation. With a down-range resolution of 0.3 m, features of the pedestrians were evident from images separated by the method. The separation error rates for the simple and proposed separation methods were 18.5 % and 4.87 %, respectively. In addition, the input time duration for each separation process was 0.8 s, and the total calculation time for training data acquisition and classification processes was 0.33 s using an Intel Core i5-2520M CPU 2.50 GHz processor. These results verified that the proposed algorithm achieves accurate and real-time separation of pedestrians in close proximity. The performance and parameter of the proposed method for various relative positions of the pedestrians are also examined. The experiments verified that the proposed method worked well compared with the simple separation method. Finally, a suitable parameter setting was established for the proposed method that optimizes the training process for the SVM, and clarified the effectiveness of the SVM compared with other classification algorithms. However, investigation on more than two targets will be an important future task.
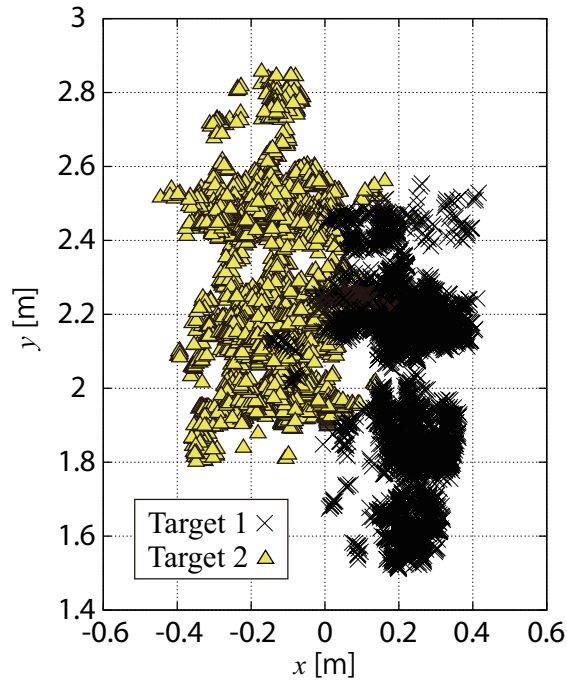
Figure 5.15: Image separation result using 3-NN.
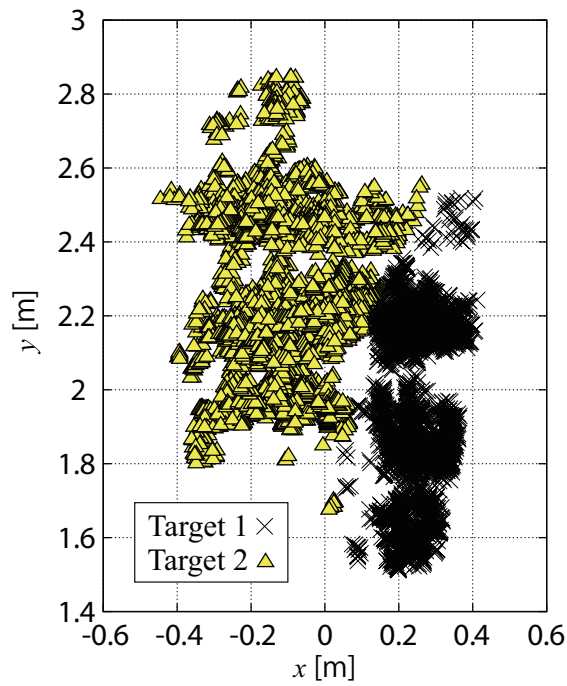
Figure 5.16: Image separation result using NBC.

111

Chapter 6

Concluding Remarks

This thesis proposes a human imaging algorithm with UWB Doppler radar interferometry, and presents two types of human identification algorithms based on estimated images, namely, the pedestrian type classification and the separation of two closely spaced pedestrians. The proposed human imaging algorithm achieved high-resolution and real-time human imaging in a realistic environment. The imaging system was composed of a small number of antennas. Moreover, the proposed classification and separation algorithms for pedestrians also work well in real-time. Various investigations of this thesis verified that the proposed human imaging and identification algorithms can satisfy requirements of the surveillance and monitoring systems described in Section 1.1.

Chapters 2 and 3 presented the imaging algorithm with UWB Doppler radar interferometry composed of a small number of antennas. Chapter 2 described the high-resolution imaging algorithm for multiple moving targets and its application to a few revolving targets and the numerical human model. The UWB Doppler radar realizes detection of multiple targets using the differences in their Doppler frequencies and ranges. The proposed imaging algorithm separates multiple scattering centers based on time-frequency analysis, and estimates the positions of each separated target using interferometry and a range interpolation technique. The experiment verified that accurate shape estimation of two revolving targets with the SPWD is achieved. The mean error of the estimated image is 5.2 mm, which corresponds to 1/58 of the nominal downrange resolution. Next, a performance evaluation for three revolving targets clarified that SDFT is better than SPWD when applied to human sensing. Thus, the performance with SDFT was investigated by means of numerical simulation assuming a walking human model composed of multiple scattering centers, and showed that the proposed algorithm extracted the outline of a human shape and its walking trajectory. These investigations meant that the UWB Doppler radar interferometry using the SDFT can accurately realize human sensing. However, many false images were confirmed.

Chapter 3 proposed a human imaging algorithm by solving the problem in terms of false images for a realistic situation. The human imaging result with UWB Doppler radar

interferometry and the many false images generated by the interference from multiple targets were also presented with the experimental data. Thus, the mechanism for this type of false image was clarified, and two detection and rejection methods for these images were proposed using velocity information. The proposed imaging algorithm is composed of these methods and UWB Doppler radar interferometry. The experiments, which assumed a pedestrian target, verified that the proposed imaging algorithm achieves high-resolution and reliable human imaging in a realistic environment. It is also confirmed that the identification of pedestrian features is realized with the time-variation of the estimated image acquired using short-time data of 0.1 s, and this means that the proposed imaging algorithm has a real-time capability. Moreover, the applications to pedestrian targets walking in arbitrary directions are presented, and high-resolution and reliable imaging was realized in all the experimental scenarios.

Chapters 4 and 5 presented the human identification applications based on the UWB Doppler radar images. Chapter 4 proposed an accurate and real-time classification algorithm for various types of pedestrians. The effective feature parameters extracted from UWB Doppler radar images and their radial velocity features were proposed. The experiments assumed six types of pedestrians (those with both arms swinging, carrying a bag and swinging one arm, and no arm motion, those on crutches and pushing wheelchairs, and a person propelling himself in a wheelchair) and verified their classification with an accuracy of 96 % is accomplished using the k-NN algorithm. Moreover, the total calculation time for the imaging and classification processes was 0.55 s with an Intel Core 2 Duo 3.33-GHz processor and the input time duration for each set of data was less than 0.8 s. These mean that the proposed classification algorithm has real-time capability. In addition, an accuracy of 99 % was achieved for the classification of three groups assuming hospital security systems (normal pedestrians, those on crutches and both wheelchair groups). The proposed algorithm is based on accurate shape/motion information obtained from UWB Doppler radar interferometry, and thus has great potential for the classification of other various motion/target types. Furthermore, we revealed that the proposed algorithm only needs training data set which is extracted from arbitrary one subject.

Chapter 5 demonstrated the image separation and identification of two closely spaced pedestrians. The proposed algorithm applies the SVM to the scattering centers estimated by UWB Doppler radar interferometry. The training data set for the SVM is extracted from the range profiles. The experiment, which assumes two pedestrians with a body separation of 0.44 m, showed that the proposed method accurately separated their images using UWB Doppler radar with a nominal down-range resolution of 0.3 m. The features of each target were confirmed in the separated images. The separation error rate for the proposed separation algorithm was 4.87 %. This was better than the simple separation method using the range profiles, whose separation error rate was 18.5 %. The input time duration for each data set for the separation process was 0.8 s, and the total calculation time for the training and separation processes was 0.33 s with an Intel Core i5-2520M CPU 2.50 GHz processor. Moreover, the effectiveness of the proposed method for var-

ious relative positions of the two pedestrians is confirmed. These results verified that the proposed algorithm achieves accurate and real-time separation of two closely spaced pedestrians and their identifications based on UWB Doppler radar images in real-time.

The targets of the present study described in Section 1.5 are practically accomplished with the proposed UWB Doppler radar interferometric imaging and identification algorithms. The proposed algorithms can realize real-time human remote sensing in input and calculation time of less than 1 s, and can produce high-resolution images whose accuracy is order of 1 cm and accurate identification results with these images for targets with various movements. However, applications to more than two targets are not considered in Chapter 5. For this purpose, an advanced algorithm based on the proposed image separation algorithm should be developed.

Moreover, one of the important future directions of study is the realization of a simpler system using adaptive antenna techniques [186]. In the present study, measurements were conducted with several antenna positions to acquire data on the whole body and a sufficient scanning area was thus required. One of the solutions to this problem is to use wide-directivity antennas. However, the amount of interference increases because the number of targets is also increased in the beam illumination area. To resolve these problems, adaptive antenna techniques should be an effective approach. This technique can scan beams electrically without mechanical scanning, which leads to smaller physical packaging. Thus, development of a combined system of UWB Doppler radar interferometry and these techniques is an important future task.

The important goal of the present study is implementation of UWB Doppler radars to intelligent robots. For robot monitoring systems, both sensing targets and radars have arbitrary motion. Thus, another possible topic for future work is to investigate the performance when the radar system is moving. The rejection of clutter will be an important and difficult problem in this case, and finding a solution to this problem is also an important future work. The use of both high-resolution UWB Doppler radar imaging and adaptive antenna techniques can be considered as an effective approach.

Furthermore, this thesis presented sensing techniques using only the UWB Doppler radar, but fusion systems with various sensors described in Section 1.2 may realize monitoring systems with higher performance. Additionally, the proposed algorithms can apply not only surveillance systems and moving robots but also other applications such as automotive radar, space observations, and medical imaging. Consequently, long-range goals are developments of advanced sensing systems including consideration of sensor fusion techniques for various applications.

Bibliography

[1] Y. H. Wu, C. Fassert, and A. S. Rigaud, "Designing Robots for the Elderly: Appearance Issue and Beyond," *Arch. Gerontol. and Geriat.*, vol. 54, no. 1, pp. 121–126, 2012.

[2] A. R. Krishna, G. S. Bala, A. S. N. Chakravarthy, B. B. P. Sarma, and G. S. Alla, "Design of a Rescue Robot Assist at Fire Disaster," *Int. J. Comput. Appl.*, vol. 47, no. 10, pp. 25–30, 2012.

[3] T. Wang, H. Zhang, X. Ma, Y. Zhu, Z. Zhou, and B. Qian, "A Home Nursing Robot System," *Lect. Notes in Electr. Eng.*, vol. 86, pp. 317–324, 2011.

[4] F. M. Moghaddam, "The New Global Insecurity: How Terrorism, Environmental Collapse, Economic Inequalities, and Resource Shortages are Changing Our World," *Praeger Pub Text*, 199pp., 2010.

[5] J. B. Yang, M. Shi, and Q. M. Yi, "A New Method for Motion Target Detection by Background Subtraction and Update," *Phys. Proc. (Elsevier)*, vol. 33, pp. 1768–1775, 2012.

[6] Y. Kawanishi, I. Mitsugami, M. Mukunoki, and M. Minoh, "Background Image Generation by Preserving Lighting Condition of Outdoor Scenes," *Proc. Soc. Behav. Sci.*, vol. 2, no. 1, pp. 137–142, 2010.

[7] L. Shidaro, C. Micheloni, and C. Chiavedale, "Video Security for Ambient Intelligence," *IEEE Trans. Sys. Man Cyb.*, vol. 35, pp. 133-144, 2005.

[8] O. Barnich and V. Droogenbroeck, "A Powerful Random Technique to Estimate the Background in Video Sequences," *Proc. of Int. Conf. Acoust. Speech Sig. Proc. (ICASSP2009)*, pp. 945–948, 2009.

[9] D. Tsai, M. Flagg, A. Nakazawa, and J. M. Rehg, "Motion Coherent Tracking Using Multi-Label MRF Optimization," *Int. J. Comput. vis.*, vol. 100, no. 2, pp. 190–202, 2012.

[10] X. Lu and R. Manduchi, "Fast Image Motion Segmentation for Surveillance Applications," *Image Vis. Comput. (Elsevier)*, vol. 29, no. 2, pp. 104–116, 2011.

[11] P. Arbelaez, "Contour Detection and Hierarchical Image Segmentation," *IEEE Trans. Patt. Anal. Mach. Intelli.*, vol. 33, no 5, pp. 898–916, 2011.

[12] S. C. Hsia, C. H. Hsiao, and C. Y. Huang, "Single-Object-Based Segmentation and Coding Technique for Video Surveillance System," *J. Elec. Imag.*, vol. 18, no. 3, Article No. 033007, 2009.

[13] P. Buehler, M. Everingham, D. P. Huttenlocher, and A. Zisserman, "Upper Body Detection and Tracking in Extended Signing Sequences," *Int. J. Comput. Vis.*, vol. 95, no. 2, pp. 180–197, 2011.

[14] T. Brox and J. Malik, "Large Displacement Optical Flow: Descriptor Matching in Variational Motion Estimation," *IEEE Trans. Patt. Anal. Mach. Intelli.*, vol. 33, no 3, pp. 500–513, 2011.

[15] N. Dalal, B. Triggs, and C. Schmid, "Human Detection Using Oriented Histograms of Flow and Appearance," *Lect. Notes in Comput. Sci.*, vol. 3952, pp. 428–441, 2006.

[16] D. G. Lowe, "Distinctive Image Features from Scale-Invariant Keypoints," *Int. J. Comput. Vis.*, vol. 60, no. 2, pp. 91–110, 2004.

[17] N. Dalal and B. Triggs, "Histograms of Oriented Fradients for Human Detection," *Proc. IEEE Computer Society Conf. on Comput. Vis. and Patt. Recogn. (CVPR2005)*, vol. 1, pp. 886–893, 2005.

[18] A. Wagner, J. Wright, A. Ganesh, Z. Zihan, H. Mobahi, and Y. Ma, "Toward a Practical Face Recognition System: Robust Alignment and Illumination by Sparse Representation," *IEEE Trans. Patt. Analy. Mach. Intell.*, vol. 34, no. 2, pp. 372–386, 2012.

[19] M. Guillaumin, T. Mensink, J. Verbeek, and C. Schmid, "Face Recognition from Caption-Based Supervision," *Int. J. Comput. Vis.*, vol. 96, no. 1, pp. 64–82, 2012.

[20] O. Déniz, G. Bueno J. Salido, and F. De la Torre, "Face Recognition Using Histograms of Oriented Gradients" *Patt. Recog. Lett.*, vol. 32, no. 12, pp. 1598–1603, 2011.

[21] X. Tan and B. Triggs, "Enhanced Local Texture Feature Sets for Face Recognition under Difficult Lighting Conditions," *IEEE Trans. Image Proc.*, vol. 19, no. 6, pp. 1635–1650, 2010.

116

[22] Y. S. Heo, K. M. Lee, and S. U. Lee, "Robust Stereo Matching Using Adaptive Normalized Cross-Correlation," *IEEE Trans. Patt. Anal. Mach. Intelli.*, vol. 33, no. 4, pp. 807–822, 2011.

[23] Y. Hohikawa, Y. Hashimoto, A. Moro, K. Terabayashi, and K. Umeda, "Tracking of Human Groups Using Subtraction Stereo," *SICE J. Contr. Meas. Sys. Integr.*, vol. 4, no. 3, pp. 214–220, 2011.

[24] K. Schindler, A. Ess, B. Leibe, and L. V. Gool, "Automatic Detection and Tracking of Pedestrians from a Moving Stereo Rig," *ISPRS J. of Photogramm. Remote Sens.*, vol. 65, pp. 523–537, 2010.

[25] G.L. Mariottini, G. Oriolo, and D. Prattichizzo, "Image-based Visual Servoing for Nonholonomic Mobile Robots Using Epipolar Geometry," *IEEE Trans. Robot.*, vol. 23, no. 1, pp. 87–100, 2007.

[26] A. W. Senior, Y. Tian and M. Lu, "Interactive Motion Analysis for Video Surveillance and Long Term Scene Monitoring," *Lect. Notes in Comput. Sci.*, vol. 6468, pp. 164–174, 2011.

[27] T. Teixeira and A. Savvides, "Lightweight People Counting and Localizing for Easily Deployable Indoors WSNs," *IEEE J. of Selected Topics in Sig. Proc.*, vol. 2, no. 4, pp.493–502, 2008.

[28] L. Xu, J. Jia, and Y. Matsushita, "Motion Detail Preserving Optical Flow Estimation," *IEEE Trans. Patt. Anal. Mach. Intelli.*, vol. 34, no. 9, pp. 1744–1757, 2012.

[29] S. Nobuhara, Y. Tsuda, I. Ohama, and T. Matsuyama, "Multi-viewpoint Silhouette Extraction with 3D Context-aware Error Detection, Correction, and Shadow Suppression," *IPSJ Trans. Comp. Vis.*, vol. 1, pp. 242–259, 2009.

[30] A. Mittal and L. S. Davis, "A General Method for Sensor Planning in Multi-Sensor Systems: Extension to Random Occlusion," *Int. J. Comp. Vis.*, vol. 76, no. 1, pp. 31–52, 2008.

[31] G. Vogiatzis, C. Hernandez, P. H. S. Torr, and R. Cipolla, "Multiview Stereo via Volumetric Graph-Cuts and Occlusion Robust Photo-Consistency," *IEEE Trans. Patt. Anal. Mac. Int.*, vol. 29, no. 12, pp. 2241–2255, 2007.

[32] M. Rioux, "Laser Range Finder Based on Synchronized Scanners," *Applied Optics*, vol. 23, no. 21, pp. 3837-3844, 1984.

[33] C. Mertz, L. E. Navarro-Serment, R. Maclachlan, P. Rybski, A. Steinfeld, A. Suppé, C. Urmson, N. Vandapel, M. Hebert, and C. Thorpe, "Moving Object Detection with Laser Scanners," *J. Feild Robotics*, vol. 1, pp. 1–27, 2012.

[34] O. M. Mozos, R. Kurazume, and T. Hasegawa, "Multi-Part People Detection Using 2D Range Data," *Int. J. Soc. Robot*, vol. 2, no. 1, pp. 31–40, 2010.

[35] D. F. Glas, T. Miyashita, H. Ishiguro, and N. Hagita, "Laser-Based Tracking of Human Position and Orientation Using Parametric Shape Modeling," *Adv. Robotics*, vol. 23, no. 4, pp. 405–428, 2009.

[36] A. Panangadan, M. Matarić, and G. S. Sukhatme, "Tracking and Modeling of Human Activity Using Laser Rangefinders," *Int. J. Soc. Robot.*, vol. 2, no. 1, pp. 95–107, 2010.

[37] B. Lau, K. O. Arras, and W. Burgard, "Multi-model Hypothesis Group Tracking and Group Size Estimation," *Int. J. Soc. Robot.*, vol. 2, no. 1, pp. 19–30, 2010.

[38] T. Bardouille, S. V. Krishnamurthy, S. G. Hajra, and R. C. N. D'Arcy, "Improved Localization Accuracy in Magnetic Source Imaging Using a 3-D Laser Scanner," *IEEE Trans. Bio-Med. Eeg.*, vol. 59, no. 12, pp. 3491–3497, 2012.

[39] T. Jing, Z. Jin, L. Ligang, P. Zhigeng, and Y. Hao, "Scanning 3D Full Human Bodies Using Kinects," *IEEE Trans. Vis. Comput. Graph..* vol. 18, no. 4, pp. 643–650. 2012.

[40] (in Japanese) M. Ariizumi, T. Kawano, Y. Abe, and K. Harada, "Development of Non-Contact 3D Measurement Technology," *KONIKA MINOLTA Tech. Rep.*, vol. 2, pp. 187–192, 2005.

[41] A. Fernández-Caballero, J. C. Castillo, J. Serrano-Cuerda, and S. Maldonado-Bascón, "Real-time Human Segmentation in Infrared Videos," *Exp. Systems with Applications (Elsevier)*, vol. 38, no. 3, pp.2577–2584, 2011.

[42] D. W. Abraham, T. J. Chainer, K. F. Etzol, and H. K. Wickramasinghe, "Thermal Image Analysis for Polygraph Testing," *IEEE Trans. Eng. Med. Bio. Mag.*, vol. 21, no. 6, pp. 56–64, 2002.

[43] H. M. Chen, S. Lee, R. M. Rao, M. A. Slamani, and P. K. Varshney, "Imaging for Concealed Weapon Detection; a Tutorial Overview of Development in Imaging Sensors and Processing," *IEEE Sig. Proc. Mag.*, vol. 22, no. 2, pp. 52–61, 2005.

[44] G. Feng, X. Guo, and G. Wang, "Infrared Motion Sensing system for Human-Following Robots," *Sens. and Actuat. A: Physical (Elseiver)*, vol. 185, pp. 1–7, 2012.

[45] Y. Yang, G. Feng, X. Guo, and G. Wang, "Compressed Infrared Bearing Sensor for Human Localization: Design and Implementation," *Proc. Int. Conf. Inform. Autm. (ICIA)*, pp. 936–940, 2012.

[46] S. D. Feller, Y. Zheng, E. Cull, and D. Brady, "Tracking and Imaging Humans on Heterogeneous Infrared Sensor Arrays for Law Enforcement Applications," *Proc. SPIE Int. Soc. Opt.* , vol. 4708, 2002.

[47] F. W. Mauldin, L. Dan, and J. A. Hossack, "The Singular Value Filter: A General Filter Design Strategy for PCA-Based Signal Separation in Medical Ultrasound Imaging," *IEEE Trans. Med. Imaging*, vol. 30, no. 11, pp. 1951–1964, 2011.

[48] L. K. Wee, H. Y. Chai, and E. Supriyanto, "Surface Rendering of Three Dimensional Ultrasound Images Using VTK," *J. Sci. Ind. Res.*, vol. 70, pp. 421–426, 2011.

[49] S.D. Santos, M. Domenjoud, and Z. Prevorovsky, "Ultrasonic Imaging of Human Tooth Using Chirp-Coded Nonlinear Time Reversal Acoustics," *Physics Proc. (Elseiver)*, vol. 3, no. 1, pp. 913–918, 2010.

[50] H. Taki, T. Sakamoto, M. Yamakawa, T. Shiina, and T. Sato, "Small Calcification Indicator in Ultrasonography Using Correlation of Echoes with a Modified Wiener filter," *J. Med. Ultasonics*, vol. 39, pp. 127–135, 2012.

[51] H. Taki, K. Taki, T. Sakamoto, M. Yamakawa, T. Shiina, M. Kudo, and T. Sato, "High Range Resolution Ultrasonographic Vascular Imaging Using Frequency Domain Interferometry with the Capon Method," *IEEE Trans. Med. Imaging*, vol. 31, No. 2, pp. 417–429, 2012.

[52] K. Saho, T. Kimura, S. Kidera, H. Taki, T. Sakamoto, and T. Sato, "Robust and Accurate Ultrasound 3-D Imaging Algorithm Incorporating Adaptive Smoothing Techniques," *IEICE Trans. Commun.*, vol. E95-B, no. 2, pp. 572-580, 2012.

[53] J. Zhang, B. W. Drinkwater, P. D. Wilcox, and A. J. Hunter, "Defect Detection Using Ultrasonic Arrays: The Multi-mode Total Focusing Method," *NDT & E International*, vol. 43, no. 2, pp. 123–133, 2010.

[54] S. Wagle and H. Kato, "Ultrasonic Wave Intensity Reflected from Fretting Fatigue Cracks at Bolt Joints of Aluminum Alloy Plates," *NDT & E International*, vol. 42, no. 8, pp. 690–695, 2009.

[55] J. Westlund, "2D SH Modelling of Ultrasonic Testing for Cracks Near a Non-Planar Surface," *Eng. Anal. Bound. Elem.*, vol. 33, no. 8–9, pp. 1103–1112, 2009.

[56] M. Bradley and J. M. Sabatier, "Aerial Ultrasonic Micro Doppler Sonar Detection Range in Outdoor Environments," *J. Acoust. Soc. Am.*, vol. 131, no. 3, pp. EL203–EL209,2012.

[57] P. Atrey, N. Maddage, and M. Kankanhalli, "Audio Based Event Detection for Multimedia Surveillance", *Proc. IEEE Int. Conf. Acoust. Speech Sig. Proc.*, vol. 5, pp. 813-816, 2006.

[58] D. Caicedo and A. Pandharipande, "Ultrasonic Array Sensor for Indoor Presence Detection," *Proc. 20th European Sig. Proc. Conf.*, pp. 175–179, 2012.

[59] G. Valenzise, L. Gerosa, and M. Tagliasacchi, "Scream and Gunshot Detection and Localization for Audio-Surveillance Systems", *Proc. IEEE Conf. on Adv. Video and Sig. Based Surveillance*, pp.21-26, 2007.

[60] Y. Zhi-jun, Y. Guang-xin, and W. Jian-ming, "Multi-model Rao-blackwellised Particle Filter for Maneuvering Target Tracking in Distributed Acoustic Sensor Network". *Proc. IEEE Int. Conf. Acous. Speech Sig. Proc.*, vol. 3, pp. 15–20, 2007.

[61] Z. Yu, S. Dong, and J. Wei, "Neural Network Aided Unscented Kalman Filter for Maneuvering Target Tracking in Distributed Acoustic Sensor Network". *Proc. Int. Conf. Comput. Theory and Applications (ICCTA)*, pp. 245-249, 2007.

[62] A. Mehmood, J. M. Sabatier, M. Bradley, and A. Ekimov, "Extraction of the Velocity of Walking Human's Body Segments Using Ultrasonic Doppler," *J. Acoust. Soc. Am.* vol. 128, pp. EL316–EL322, 2010.

[63] A. Balleri, K. Chetty, and K. Woodbridge, "Classification of Personnel Targets by Acoustic Micro-Doppler Signatures," *IET Radar Sonar Navig.*, vol. 5, no. 9, pp. 943–951, 2011.

[64] S. Bernal, G. Garreau, C. Andreu, A. Andreou, J. Georgiou, T. Wennekers, and S. Denham, "Human Action Categorization Using Ultrasound Micro-Doppler Signatures," *Lect. Notes Comput. Sci.*, vol. 7065, no. 1, pp. 18–28, 2011.

[65] S. Hirata and H. Hachiya, "Study About Accuracy and Resolution of Ultrasonic Distance and Velocity Measurement for Moving Objects Using M-sequence Modulated Signals," *Proc. Symp. Ultrasonic Electron.*, vol. 33, pp. 297–298, 2012.

[66] T. Hayashi, S. Hirata, and H. Hachiya, "Coded Signal Pair for Simultaneous Ultrasound Transmission in High-Speed Acoustic Imaging," *Proc. Symp. Ultrasonic Electron.*, vol. 33, pp. 335–336, 2012.

[67] R. C. Luo, O. Chen, and P. H. Lin, "Indoor Robot/Human Localization Using Dynamic Triangulation and Wireless Pyroelectric Infrared Sensory Fusion Approaches," *Proc. IEEE Int. Conf. Robot. and Automat.*, pp. 1359–1364, 2012.

[68] F. Colone, K. Woodbridge, H. Guo, D. Mason, and C. J. Baker, "Ambiguity Function Analysis of Wireless LAN Transmissions for Passive Radar," *IEEE Trans. Aero. Elec. Sys.*, vol. 47, no. 1, pp. 240–264, 2011.

[69] K. Chetty, G. E. Smith, and K. Woodbridge, "Through-the-Wall Sensing of Personnel Using assive Bistatic WiFi Radar at Standoff Distances," *IEEE Trans. Geosci. Remote Sens.*, vol. 50, No. 4, pp. 1218–1226, 2012.

[70] K. Chetty, G. E. Smith, H. Guo, and K. Woodbridge, "Target Detection in High Clutter using Passive Bistatic WiFi Radar," *Proc. IEEE Radar Conf.*, pp. 1–5, 2009.

[71] J. Yim, C. Park, J. Joo, and S. Jeong, "Extended Kalman Filter for Wireless LAN based Indoor Positioning," *Decis. Support Syst. (Elsevier)*, vol. 45, no. 4, pp. 960–971, 2008.

[72] J. M. Christiansen and K. E. Olsen, "Range and Doppler walk in DVB-T based Passive Bistatic Radar," *Proc. IEEE Radar Conf.*, pp. 620–626, 2010.

[73] D. Tan, H. Sun, Y. Lui, M. Lesturgie, and H. Chan, "Passive Radar Using Global System for Mobile Communication Signal: Theory, Implementation and Measurements," *IEE Proc. Radar, Sonar and Navig.*, vol. 152, no. 3, pp. 116–123, 2005.

[74] C. Ozdemir, "Inverse Synthetic Aperture Radar Imaging with MATLAB Algorithm," *John Wiley and Sons Inc.*, 383pp., 2012.

[75] D. L. Mensa, "High Resolution Radar Cross-Section Imaging," *Artech House Inc.*, 270pp., 1991.

[76] X. Bai, F. Zhou, M. Xing, and Z. Bao, "High Resolution ISAR Imaging of Targets with Rotating Parts," *IEEE Trans. Aero. Elec. Sys.*, vol. 47, no. 4, pp. 2530–2543, 2011.

[77] Y. Wang and J. Yicheng, "Fourth Order Complex-Lag PWVD for Multicomponent Signals with Application in ISAR Imaging of Maneuvering Targets," *Circuits Syst. Sig. Process.*, vol. 29, no. 1, pp. 449–457, 2010.

[78] J. Li, C.-W. Qiu, L. Zhang, M. Xing, Z. Bao, and T.-S. Yeo, "Time-Frequency Imaging Algorithm for Highspeed Spinning Targets in Two Dimensions," *IET Radar Sonar Navig.*, vol. 4, no. 6, pp. 806–817, 2010.

[79] T. Sato, "Shape Estimation of Space Debris Using Single-Range Doppler Interferometry," *IEEE Trans. Geosci. Remote Sens.*, vol. 37, no. 2, pp. 1000–1005, 1999.

[80] F. Foroozan and A. Asif, "Time-Reversal Ground-Penetrating Radar: Range Estimation With Cramér-Rao Lower Bounds," *IEEE Trans. Geosci. Remote Sens.*, vol. 48, no. 10, pp. 3698–3708, 2010.

[81] D. Liu, G. Kang, L. Li, Y. Chen, S. Vasudevan, W. Joines, Q.H. Liu, J. Krolik, and L. Carin, "Electromagnetic Time-Reversal Imaging of a Target in a Cluttered Environment," *IEEE Trans. Antenna Propagat.*, vol. 53, no. 9, pp. 3058–3066, 2005.

[82] V. C. Chen, F. Li, S. S. Ho, and H. Wechsler, "Micro-Doppler Effect in Radar: Phenomenon, Model, and Simulation Study," *IEEE Trans. Aero. Elec. Sys.*, vol. 42, no. 1, pp. 2–21, 2006.

[83] V. C. Chen, F. Li, S. S. Ho, and H. Wechsler, "Analysis of Micro-Doppler Signatures," *IET Radar Sonar Navig.*, vol. 150, no. 4, Accession no. 7781469, 2003.

[84] F.H.C. Tivive, A. Bouzerdoum, M. Herberthson, and M.G. Amin, "A Human Gait Classification Method Based on Radar Doppler Spectrogram," *EURASIP J. Adv. Sig. Proc.*, vol. 2010, Article ID 389716, 2010.

[85] J. Li, S. L. Phung, F. H. C. Trivive, and A. Bouzerdoum, "Automatic Classification of Human Motions using Doppler Radar," *Proc. IEEE World Cong. Comput.Intell.*, pp. 1–6, 2012.

[86] A. Sume, M. Gustafsson, M. Herberthson, A. Jänis, S. Nilsson, J. Rham, and A. Örbom "Radar Detection of Moving Targets Behind Corners," *IEEE Trans. Geosci. Remote Sens.*, vol. 49, no. 6, pp. 2259–2267, 2011.

[87] Y. Kim and H. Ling, "Human Activity Classification Based on Micro-Doppler Signatures Using a Support Vector Machine," *IEEE Trans. Geoscie. Remote Sens.*, vol. 47, no. 5, pp. 1328–1337, 2009.

[88] S. Bjorklund, T. Johansson, and H. Petersson, "Evaluation of a Micro-Doppler Classification Method on mm-Wave Data," *Proc. IEEE Radar Conference 2012*, pp. 0934–0939, 2012.

[89] L. Liu, M. Popescu, M. Skubic, T. Yardibi, and P. cuddihy, "Automatic Fall Detection Based on Doppler Radar Motion Signature," *Proc. 5th Int. Conf. pervasive-Health and Workshops*, pp. 222–225, 2011.

[90] G. E. Smith, W. Karl, and C. J. Baker, "Radar Micro-Doppler Signature Classification using Dynamic Time Warping," *IEEE Trans. Aero. Elec. Sys.*, vol 46, no. 3, pp. 1078–1096, 2010.

[91] B. Igal and T. Joseph, "Radar Target Classification using Doppler Signatures of Human Locomotion Models," *IEEE Trans. Aero. Elec. Sys.*, vol. 43, no. 4, pp. 1510–1522, 2007.

[92] L. Liu, M. Popescu, and M. Skubic, "Fall Detection Using Doppler Radar and Classifier Fusion," *Proc. IEEE-EMBS Int. Conf. Biomed. and Health Informat.*, pp. 180–183, 2012.

[93] Y. Kim and H. Ling, "Through-Wall Human Tracking with Multiple Doppler Sensors Using an Artificial Neural Network," *IEEE Trans. Ant. Prop.*, vol. 57, no. 7, pp. 2116–2122, 2009.

[94] S. H. Darwish, M. A. Ellatif, and M. Morsy, "Micro-Doppler Detection and Target Identification Using Artificial Neural Network," *Proc. IEEE Aero. Conf.*, pp. 1–5, 2012.

[95] J. Astola, K. Egiazarian, and A. Totsky, "Ground Moving Target classification by using DCT Coefficients Extracted from Micro-Doppler Radar Signatures and Artificial Neuron Network, " *Proc. Microwaves, Radar and Remote Sensing Symp.*, pp. 173–176, 2011.

[96] G. Garreau, C. M. Andreou, A. G. Andreou, J. Georgiou, S. Bernal, T. Wennekers, and S. Denham, "Gait-Based Person And Gender Recognition Using Micro-Doppler Signatures," *Proc. IEEE Biomedical Circ. and Syst. Conf.*, pp. 444–447, 2011.

[97] P. Setlur, F. Ahmad, and M. Amin, "Maximum Likelihood and Suboptimal Schemes for Micro-Doppler Estimation Using Carrier Diverse Doppler Radars," *IET Sig. Process.*, vol. 5, no. 2, pp. 194–208, 2011

[98] G. Smith, K. Woodbridge, and C. Baker, "Template Based Micro-doppler Signature Classification," *3rd European Radar Conf.*, pp. 127–144, 2006.

[99] M. B. Guldogan, F. Gustafsson, U. Orguner, S. Bjorklund, H. Petersson and A. Nezirovic, "Human Gait Parameter Estimation Based on Micro-Doppler Signatures Using Particle Filters," *Proc. IEEE Int. Conf. Acoust. Speech Sig. Proc. *, pp. 5940–5943, 2011.

[100] S. Bjorklund, T. Johansson, and H. Petersson, "Evaluation of a Micro-Doppler Classification Method on mm-Wave Data," *Proc. IEEE Radar Conf.*, pp. 0934–0939, 2012.

[101] J. Zhang, "Analysis of Human Gait Radar Signal Using Reassigned WVD," *Physics Proc. (Elsevier)*, vol. 24, pp. 1607–1614, 2012.

[102] T. Thayaparan, S. Abrol, E. Riseborough, L. Stankovic, D. Lamothe, and G. Duff, "Analysis of Radar Micro-Doppler Signatures from Experimental Helicopter and Human Data," *IET Radar Sonar Navig.*, vol. 1, no. 4, pp. 289–299, 2007.

[103] I. Orović, S. Stanković, and M. Amin, "A New Approach for Classification of Human Gait Based on Time-Frequency Feature Representations," *Sig. Process. (Elsevier)*, vol. 91, no. 6, pp. 1448–1456, 2011.

[104] D. P. Fairchild and R. M. Narayanan, "Human Activity Classification Using Hilbert-Huang Transform Analysis of Radar Doppler Data", *Proc. Soc. of Photo-Opt. Instrum. Eng. 8021*, Paper no. 80210F, 2011.

[105] E. G. Smith, K. Woodbridge and J. C. Baker, "Template Based Micro-Doppler Signature Classification," *Proc. 2006 European Radar Conf.*, pp. 127–144, 2006.

[106] G. E. Smith, K. Woodbridge, and C. Baker, "Naíve Bayesian Radar Micro-Doppler Recognition," *Proc. Int. Conf. Radar 2008*, pp. 111–116, 2008.

[107] A. Lin and H. Ling, "Doppler and Direction-of-Arrival (DDOA) Radar for Multiple-Mover Sensing," *IEEE Trans. Aero. Elec. Sys.*, vol. 43, no. 4, pp. 1496–1509, 2007.

[108] A. Lin and H. Ling, "Frontal Imaging of Human Using Three Element Doppler and Direction-of-Arrival Radar," *Electron. Lett.*, vol. 42, no. 11, pp. 660–661, 2006.

[109] A. Lin and H. Ling, "Three-Dimensional Tracking of Humans Using Very Low Complexity Radar," *Electron. Lett.*, vol. 42, no. 18, pp. 1062–1063, 2006.

[110] I. Shafi, J. Ahmad, S. I. Shah, and F. M. Kashif, "Techniques to Obtain Good Resolution and Concentrated Time-Frequency Distributions: A Review," *EURASIP J. Adv. Sig. Proc.*, vol. 2009, Article ID 673539, 2009.

[111] F. Hlawatsch and G. F. Boudreaux-Bartels, "Linier and Quadratic Time-Frequency Signal Representations," *IEEE Sig. Proc. Mag.*, vol. 9, pp. 21–67, 1992

[112] E. Jacobsen and R. Lyons, "The Sliding DFT," *IEEE Trans. Sig. Proc. Mag.*, vol. 20, no. 2, pp. 74–80, 2003.

[113] Y. Wang and Y. Jiang, "Fourth-Order Complex-Lag PWVD for Multicomponent Signals with Application in ISAR Imaging of Maneuvering Targets," *Circ. Syst. Sig. Process.*, vol. 29, pp. 449–456, 2010.

[114] Y. Wu and D. C. Munson "Wide-Angle ISAR Passive Imaging Using Smoothed Pseudo Wigner-Ville Distribution," *Proc. IEEE Radar Conf.*, pp. 363–368, 2001.

[115] S. Mallat, "A Theory for Multiresolution Signal Decomposition: The Wavelet Representation," *IEEE Trans. Pattern Anal. Machine Intell.*, vol. 11, pp. 674–693, 1989.

[116] F. Cakrak and P. J. Loughin, "Multiwindow Time-Varying Spectrum with Instantaneous Bandwidth and Frequency Constraints," *IEEE Trans. Sig. Proc.*, vol. 49, no. 8, pp. 1656–1666, 2001.

[117] N. Huang, Z. Shen, S. Long, M. Wu, H. Shih, Q. Zheng, N. Yen, C. Tung, and H. Liu, "The Empirical Mode Decomposition and the Hilbert Spectrum for Nonlinear and Non-Steady Time Series Analysis," *Proc. R. Soc. London Ser. A,*, vol. 454, pp. 903–995, 1998.

[118] F. Rosenblatt, "The Perceptron: a Probabilistic Model for Information Storage and Organization in the Brain," *Psychology. Rev.*, vol. 65, pp. 386–408, 1959.

[119] V. Vapnik and A. Lerner, "Pattern Recognition Using Generalized Portrait Method," *Automn. Remote Contr.*, vol. 24, pp. 774–780, 1963.

[120] A. G. Stove and S. R. Sykes, "A Doppler-based target classifier using linear discriminants and principal components," *Proc. Int. Radar Conf.*, pp. 171–176, 2003.

[121] A. G. Stove and S. R. Sykes, "A Doppler-based Automatic Target Classifier for a Battlefield Surveillance Radar," *Proc. Int. Conf. IEE RADAR*, pp. 419–423, 2002.

[122] C. Cortes and V. Vapnik, "Support-Vector Networks," *J. Mac. Learn.*, vol. 20, pp.273–297, 1995.

[123] C. J. C. Burges, "A Tutorial on Support Vector Machines for Pattern Recognition," *Data Min. Knowl. Discov.*, vol. 2, no. 2, pp. 121–167, 1998.

[124] C. L. Huanga, M. C. Chenb, and C. J. Wangc, "Credit Scoring with a Data Mining Approach Based on Support Vector Machines," *Exp. Syst. with Applications (Elsevier)*, vol. 33, no. 4, pp. 847–856, 2007.

[125] R. Kalaivani and P. Thangaraj, "River Water Level Prediction in Satellite Images Using Support Vector Machine," *Int. J. Comp. Appl.*, vol. 43, no. 23, pp. 27–33, 2012.

[126] C. W. Hsu and C. J. Lin, "A Comparison of Methods for Multiclass Support Vector Machines," *IEEE Trans. Neural Netw.*, vol. 13, no. 2, pp. 415–425, 2002.

[127] T. M. Cover and P .E. Hart, "Nearest Neighbor Pattern Classification," *IEEE Trans. Info. Theo.*, vol. 13, no. 1, pp. 21–27, 1968.

[128] Y. Liao and V. R. Vemuri, "Use of K-NearestNeighbor Classifier for Intrusion Detection," *Comput. Secur. (Elseiver)*, vol. 21, no. 5, pp. 439–448, 2002.

[129] Y. Li, C. Luo and S. M. Chung, "Weighted Naive Bayes for Text Classification Using Positive Term-Class Dependency," *Int. J. Artif. Intell. Tools*, vol. 21, no. 1, Article no. 1250008, 2012.

[130] M. Westa, J. Szymański, and H. Krawczyk, "Text Classifiers for Automatic Articles Categorization," *Artif. Intell. and Soft Comput.*, vol. 7268, pp. 196–204, 2012.

[131] N. K. Ibrahim, R. S.A.R. Abdullah, and M. I. Saripan, "Artificial Neural Network Approach in Radar Target Classification," *J. Comuput. Sci.*, vol. 5, no. 1, pp. 23–32, 2009.

[132] G. Breed, "A Summary of FCC Rules for Ultra Wideband Communications," *High Freq. Electron.*, pp. 42–44, 2005.

[133] A. Dhital, P. Closas and C. Fernández-Prades, "Bayesian Filtering for Indoor Localization and Tracking in Wireless Sensor Networks," *EURASIP J. Wirel. Commun. Netw.*, vol. 2012, Article no. 21, 2012.

[134] S. Jovanoska and R. Thoma, "Multiple Target Tracking by a Distributed UWB Sensor Network Based on the PHD Filter," *Proc. Int. Conf. Information Fusion*, pp. 1095–1102, 2012.

[135] S. Hantscher, B. Schlenther, M. Hagelen, S.A. Lang, H. Essen, A. Tessmann, A. Hulsmann, A. Leuther, and M. Schlechtweg, "Security Pre-Screening of Moving Persons Using a Rotating Multichannel W-Band Radar," *IEEE Trans. Micro. Theo. Tech.*, vol. 60, no. 3, pp. 870–880, 2012.

[136] H. Hatano, K. Sugiyama, T. Mizutani, and Y. Kuwahara, "Error Reduction Algorithm for Target Position Estimation Using Reflected Signals," *IEICE Trans. Commun.*, vol. E94-B, no. 10, pp. 2886–2890, 2011.

[137] E. Paolini, A. Giorgetti, M. Chiani, R. Minutolo, and M.Montanari, "Localization Capability of Cooperative Anti-Intruder Radar Systems," *EURASIP J. Adv. Sig. Proc.*, Article no. 726854, 2008.

[138] A. Stephan, J. Y. Baudais, and J. F. Hélard, "Range Improvement of UWB Systems Using Adaptive Multicarrier Spread-Spectrum and MIMO Techniques," *Euro. Trans. Telecomms.*, vol. 19, no. 5, pp. 589–599, 2008.

[139] X. Zhuge and A. G. Yarovoy, "A Sparse Aperture MIMO-SAR-based UWB Imaging System for Concealed Weapon Detection," *IEEE Trans. Geosci. Remote Sens.*, vol. 49, no. 1, pp. 509–517, 2011.

[140] Y. Wang and A. E. Fathy, "Advanced System Level Simulation Platform for Three-Dimensional UWB Through-Wall Imaging SAR Using Time-Domain Approach," *IEEE Trans. Geosci. Remote Sens.*, vol. 50, no. 5, pp. 1986–2000, 2012.

[141] F. Gumbmann and L. Schmidt, "Millimeter-Wave Imaging With Optimized Sparse Periodic Array for Short-Range Applications," *IEEE Trans. Geosci. Remote Sens.*, vol. 49, no. 10, pp. 3629–3638, 2011.

[142] J. P. Fitch, "Synthetic Aperture Radar," New York, Springer-Verlag, 170pp., 1988.

[143] T. Suzuki and I. Arai, "Advance on Underground Radars," *IEICE Trans. Commun.*, vol. E74-B, no. 2, pp. 289–294, 1991.

[144] L. Zhang, Z.-J. Qiao, M.-D. Xing, K.-L. Sheng, R. Guo, and Z. Bao "High-Resolution ISAR Imaging by Exploiting Sparse Apertures," *IEEE Trans. Ant. Prop.*, vol. 60, no. 2, pp. 997–1008, 2012.

[145] S. Stoa, N. Andersen, K. Granhaug, T. S. Lande, and H. A. Hjortland, "CMOS Nanoscale Impulse Radar Utilized in 2-dimensional ISAR Imaging System," *Proc. IEEE Radar Conf.*, pp. 714–719, 2012.

[146] S. Bertl, A. Dallinger, and J. Detlefsen, "Interferometric Focusing for the Imaging of Humans," *IET Radar Sonar Navig.*, vol. 4, no. 3, pp. 457–463, 2010.

[147] S. Bertl, A. Dallinger, and J. Detlefsen, "Broadband Circular Interferometric Millimetre-Wave ISAR for Threat Detection," *Adv. Radio Sci.*, vol. 5, pp. 147–151, 2007.

[148] S. Dhar, A. Poddar, P. Karmakar, T. Paul, D. Kandar, and R. Bera, "Radar Target Modeling and 2D ISAR Imaging at 76GHz for ITS Application," *Proc. Annual IEEE India conf.*, Paper ID 6139459, 2011.

[149] M. E. Yavuz and F. L. Teixeira, "Space-Frequency Ultrawideband Time-Reversal Imaging," *IEEE Trans. Geosci. Remote Sens.*, vol. 46, no. 4, pp. 1115–1124, 2008.

[150] L. Borcea, G. Papanicolaou, and C. Tsogka, "Theory and Applications of Time Reversal and Interferometric Imaging," *Inv. Problems*, vol. 19, pp. S139–S164, 2003.

[151] H. Choi, Y. Ogawa, T. Nishimura, and T. Ohgane, "Time-Reversal MUSIC Imaging with Time-Domain Gating Technique," *IEICE Trans. Commun.*, vol. E95-B, no. 7, pp. 2377–2385, 2012.

[152] Y. Jin and J. M. F. Moura, "Time-Reversal Detection Using Antenna Arrays," *IEEE Trans. Sig. Proc.*, vol. 57, pp.1396–1414, 2009.

[153] C. Yifan, E. Gunawan, K. S. Low, S. Wang, C. B. Soh, and T. C. Putti, "Time-Reversal Ultrawideband Breast Imaging: Pulse Design Criteria Considering Multiple Tumors With Unknown Tissue Properties," *IEEE Trans. Ant. Prop.*, vol. 56, no. 9, pp. 3073–3077, 2008.

[154] R. C. Conceicão, M. O'Halloran, E. Jones, and M. Glavin, "Investigation of Classifiers for Early-Stage Breast Cancer Based on Radar Target Signatures," *Prog. Electromagn. Res.*, vol. 105, pp. 295–311, 2010.

[155] N. Maaref, P. Millot, X. Ferrieres, C. Pichot, and O. Picon, "Electromagnetic Imaging Method Based on Time Reversal Processing Applied to Through-the-Wall Target Localization," *Prog. Electromagn. Res. M*, vol. 1, pp. 59–67, 2008.

[156] M. Davy, T. Lepetit, J. de Rosny, C. Prada, and M. Fink, "Detection and Imaging of Human Beings Behind a Wall Using the DORT Method," *Prog. Electromagn. Res.*, vol. 110, pp. 353–369, 2010.

[157] R. Dubroca, N. Fortino, J.-Y. Dauvignac, L. Bellomo, S. Pioch, M. Saillard, T. Lepetit, J. de Rosny, C. Prada, P. Millot, N. Maafer, and B. Boudamouz, "Time Reversal-Based Processing for Human Targets Detection in Realistic Through-the-Wall Scenarios," *Proc. 2011 Eropean Radar Conf. (EuRAD)*, pp. 1–4, 2011.

[158] S. Fujita, T. Sakamoto, and T. Sato, "2-dimensional Accurate Imaging with UWB Radar Using Indoor Multipath Echoes for a Target in Shadow Regions," *IEICE Trans. Commun.*, vol. E94-B, no. 8, pp. 2366–2374, 2011.

[159] Y. Jin, J. M. F. Moura, N. O'Donoughue, and J. Harley, "Single Antenna Time Reversal Detection of Moving Target," *Proc. IEEE Int. Conf. Acoust. Speech and Sig. Proc.*, pp. 3558–3561, 2010.

[160] T. Sakamoto and T. Sato, "A Target Tracking Method with a Single Antenna Using Time-Reversal UWB Radar Imaging in a Multi-Path Environment," *Proc. 2010 IEEE Int. Geosci. Remote Sens. Symp.*, pp. 3319-3322, 2010.

[161] (in Japanese) T. Sato and T. Sakamoto, "Image Reconstruction Algorithms for UWB Pulse Radar Systems," *IEICE Trans. Commun.*, vol. J88-B, no. 12, pp. 2311–2325 , 2005.

[162] T. Sakamoto and T. Sato, "A Target Shape Estimation Algorithm for Pulse Radar Systems Based on Boundary Scattering Transform," *IEICE Trans. Commun.*, vol. E87-B, no. 5, pp. 1357–1365, 2004.

[163] T. Sakamoto, "A Fast Algorithm for 3-Dimensional Imaging with UWB Pulse Radar Systems," *IEICE Trans. Commun.*, vol. E90-B, no. 3, pp. 636–644, 2007.

[164] T. Sakamoto and T. Sato, "An Estimation Algorithm of Target Location and Scattered Waveforms for UWB Pulse Radar Systems," *IEICE Trans. Commun.* vol. E87-B, no. 6, pp. 1631–1638, 2004.

[165] S. Kidera, T. Sakamoto, and T. Sato, "High-Resolution and Real-Time 3-D Imaging Algorithm with Envelope of Spheres for UWB radars," *IEEE Trans. Geosci. and Remote Sens.*, vol. 46, no. 11, pp. 3503-3513, 2008.

[166] T. C. Williams, J. M. Sill, and E. C. Fear, "Breast Surface Estimation for Radar-Based Breast Imaging System," *IEEE Trans. Biomed. Eng.*, vol. 44, no. 6, pp. 1678–1686, 2008.

[167] T. Sakamoto, H. Taki, and T. Sato, "An Experimental Study of Ultrasonic Imaging with a Reduced Number of Array Elements using the Envelope Method," *Acoust. Sci. and Tech.*, vol. 32, no. 4, pp. 143-150, 2011.

[168] T. Sakamoto and T. Sato, "2-Dimensional Imaging of Human Bodies with UWB Radar Using Approximately Uniform Walking Motion along a Straight Line with the SEABED Algorithm," *IEICE Trans. Commun.*, vol. E91-B, no. 11, pp. 3695–3703, 2008.

[169] Y. Matsuki, T. Sakamoto, and T.Sato, "An Imaging Algorithm of a Target with Arbitrary Motion for Ultra Wide-Band Radar with a Small Number of Antennas," *IEICE Trans. Commun.*, vol. E94-B, no. 3, pp. 742–749, 2011.

[170] T. Sakamoto and T. Sato, "Two-Dimensional Ultra-Wide-Band Radar Imaging of a Target with Arbitrary Translation and Rotation," *IEEE Trans. Geosci. Remote Sens.*, vol. 49, no. 11, pp. 4493–4502, 2011.

[171] T. Sakamoto, Y. Matsuki, and T. Sato, "Method for the Three-Dimensional Imaging of a Moving Target Using an Ultra-Wideband Radar with a Small Number of Antennas," *IEICE Trans. Commun.*, vol. E95-B, no. 3, pp. 972–979, 2012.

[172] W. Shiyou, X. Yanyun, C. Jie, M. Shengwei, F. Guangyou, and Y. Hejun, "A New Method of Through Wall Moving Target Detection and Imaging Using UWB-SP Radar," *Proc. 2011 IEEE Int. Geosci. and Remote Sens. Symp. (IGARSS)*, pp. 182–185, 2011.

[173] S. Kidera, T. Sakamoto, and T. Sato, "Accurate UWB Radar 3-D Imaging Algorithm for Complex Boundary without Range Points Connections," *IEEE Trans. Geosci. Remote Sens.*, vol. 48, no. 4, pp. 1993-2004, 2010.

[174] S. Hantscher and C. G. Diskus, "Pulse-Based Radar Imaging Using a Genetic Optimization Approach for Echo Separation," *IEEE Sensors J.*, vol. 9, no. 3, pp. 271–276, 2009.

[175] T. Sakamoto, H. Matsumoto, and T. Sato, "A High-resolution Imaging Algorithm for Complex-Shaped Target Shapes by Optimizing Quasi-Wavefronts," *Proc. IEEE Int. Symp. Ant. and Prop. Soc. (AP-S) 2008*, Paper no. IF516.5, 2008.

[176] Y. Xu, S. Dai, S. Wu, J. Chen, and G. Fang, "Vital Sign Detection Method Based on Multiple Higher Order Cumulant for Ultrawideband Radar," *IEEE Trans. Geosci. Remote Sens.*, vol. 50, no. 4, pp.1254–1265, 2012.

[177] D. Girbau, A. Lazaro, A. Ramos, and R. Villarino, "Remote Sensing of Vital Signs Using a Doppler Radar and Diversity to Overcome Null Detection," *IEEE Sensors J.*, vol. 12, no. 3, pp.512–518, 2012.

[178] D. Nagae and A. Mase, "Measurement of Heart Rate Variability and Stress Evaluation by Using Microwave Reflectometric Vital Signal Sensing," *Rev. Sci. Instrum.*, vol. 81, no. 9, Article ID 094301, 2010.

[179] Z. Zeng, J. Sun, and F. Liu, "Through-Wall Detection of Human Being's Movement by UWB Radar," *IEEE Geosci. Remote Sens. Lett.*, vol. 9, no. 6, pp.1079–1083, 2012.

[180] O. R. Fogle and B. D. Rigling, "Micro-Range/Micro-Doppler Decomposition of Human Radar Signatures," *IEEE Trans. Aero. Elec. Sys.*, vol. 48, no. 4, pp. 3058–3072, 2012.

[181] S. Singh, Q. Liang, D. Chen, and L. Shen, "Sense Through Wall Human Detection Using UWB radar," *EURASIP J. Wireless Commun. Netw.*, vol. 1, pp. 20–31, 2011.

[182] A. G. Yarovoy, L. P. Ligthart, J. Matuzas, and B. Levitas, "UWB Radar for Human Being Detection," *IEEE Aero. Elec. Sys. Mag.*, vol. 21, no. 3, pp. 10–14, 2006.

[183] G. E. Smith, F. Ahmad, and M. G. Amin, "Micro-Doppler Processing for Ultra-Wideband Radar Data," *Proc. Radar Sensor Tech. XVI (SPIE)*, paper no. 10, 2012.

[184] R. Pickholts, D. Schilling, and L. B. Milstein, "Theory of Spread-Spectrum Communications-A Tutorial," *IEEE Trans. Commun.*, vol. 30, no. 5, pp. 855–882, 1982.

[185] T. Fukuda, N. Nagoro, S. Ujita, S. Nagai, M. Nishijima, H. Sakai, T. Tanaka, and D. Ueda, "A 26GHz Short-Range UWB Vehicular Radar Using 2.5 Gcps Spread Spectrum Modulation," *Proc. IEEE/MTT-S Int. Microwave Symp.*, pp. 1311–1314, 2007.

[186] K. Kamio, K. Nishimura, and T. Sato, "Adaptive Sidelobe Control for Clutter Rejection of Atmospheric Radars," *Ann. Geophys.*, vol. 22, no. 11, pp. 4005–4012. 2004.

Major Publications

Refereed Papers

1   <u>Kenshi Saho</u>, Tomoki Kimura, Shouhei Kidera, Hirofumi Taki, Takuya Sakamoto, and Toru Sato, "Robust and Accurate Ultrasound 3-D Imaging Algorithm Incorporating Adaptive Smoothing Techniques," *IEICE Transactions on Communications*, vol. E95-B, no. 2, pp. 572–580, February 2012.

2   <u>Kenshi Saho</u>, Takuya Sakamoto, Toru Sato, Kenichi Inoue, and Takeshi Fukuda, "Pedestrian Imaging Using UWB Doppler Radar Interferometry," *IEICE Transactions on Communications*, vol. E96-B, no. 2, pp. 613–623, February 2013.

Refereed Conference Proceedings

1   <u>Kenshi Saho</u>, Tomoki Kimura, Shouhei Kidera, Hirofumi Taki, Takuya Sakamoto, and Toru Sato, "Experimental study of robust and high-resolution ultrasound imaging algorithm with adaptive smoothing techniques," *Workshop for Space, Aeronautical and Navigational Electronics 2008 (WSANE2008)*, Paper no. SANE2008–84, pp. 119–124, Qingdao, China, November 2008.

2   <u>Kenshi Saho</u>, Takuya Sakamoto, Toru Sato, Kenichi Inoue, and Takeshi Fukuda, "High-resolution UWB Doppler radar interferometric imaging algorithm for multiple moving targets with smoothed pseudo Wigner distribution," *International Conference on Space, Aeronautical and Navigational Electronics 2010 (ICSANE2010)*, Paper no. SANE2010–114, pp. 261–266, Jejudo, Korea, October 2010.

3   <u>Kenshi Saho</u>, Takuya Sakamoto, Toru Sato, Kenichi Inoue, and Takeshi Fukuda, "Experimental Study of Real-Time Human Imaging Using UWB Doppler Radar Interferometry," *6th European Conference on Antennas and Propagation (EuCAP2012)*, Presentation ID M16–3, pp. 3495–3499, Prague, Czech Republic, March 2012.

4   <u>Kenshi Saho</u>, Takuya Sakamoto, Toru Sato, Kenichi Inoue, and Takeshi Fukuda, "Pedestrian Classification Based on Radial Velocity Features of UWB Doppler Radar Images," *International Symposium on Antennas and Propagation 2012 (ISAP2012)*, Paper ID P0039, pp. 90–93, Nagoya, Japan, October 2012.

5   <u>Kenshi Saho</u>, Takuya Sakamoto, and Toru Sato, "Imaging of pedestrians with UWB Doppler radar interferometry," *International Union of Radio Science, 2013 International Symposium on Electromagnetic Theory (URSI-EMTS 2013)*, Accepted for presentation, Hiroshima, Japan, May 2013.

Patents

1   Takeshi Fukuda, Kenichi Inoue, Toru Sato, Takuya Sakamoto, and <u>Kenshi Saho</u>, "Radar Imaging Device, Imaging Method and Program Therefor," International Application Number: PCT/JP2011/003657, International Filing Date: 27.06.2011, Publication Number: WO/2012/020530, Publication Date: 16.02.2012.

2   Takeshi Fukuda, Kenichi Inoue, Toru Sato, Takuya Sakamoto, and <u>Kenshi Saho</u>, "Radar Imaging Apparatus, Imaging Method, and Program Thereof," Application Number: 13/478323, Filing Date: 23.05.2012, Publication Number: US2012/0293359, Publication Date: 22.11.2012.

Awards

1   Best Paper Award, International Symposium on Antennas and Propagation (ISAP) 2012, November 1st 2012.

2   Best Research Award, Kyoto University ICT Innovation 2013, February 19th 2013.